Author:
Sun, Xin

Title:
Complex ferrite thin films for photoelectrochemical water splitting

Complex ferrite thin films for photoelectrochemical water splitting

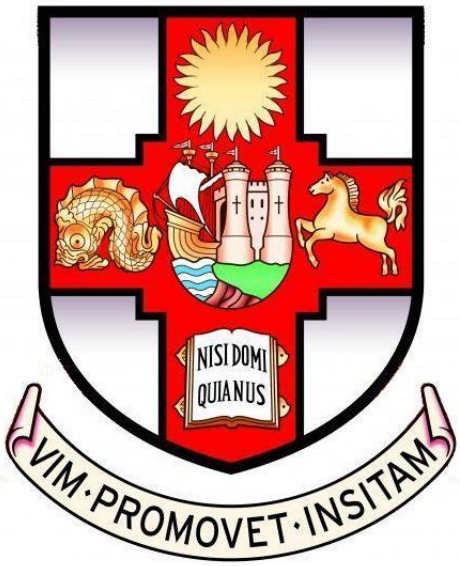

Xin Sun

A dissertation submitted to the University of Bristol in accordance with the requirements for award of the degree of Doctor of Philosophy in the School of Chemistry, Faculty of Science

September 2020

Word Count: 41000

Abstract

The traditional energy consumption that relies on fossil fuels has triggered a number of issues, such as excessive carbon dioxide emission and poor sustainability. Solar energy as a promising renewable source permits a free, universal, and secure energy access. Photoelectrochemical water splitting technology can convert it into solar fuel, achieving the effective usage of solar energy, which opens new avenues for the transformation of the global energy system.

Transition metal oxide absorbers have made rapid progress in the field of photoelectrochemical (PEC) water splitting over the past few decades, primarily due to their chemical stability, low cost and tunability of electronic properties. However, numerous formidable challenges obstruct their development in viable and scalable PEC water splitting technology. The investigation of ferrite-based ternary oxides, $LaFeO_3$ and $GaFeO_3$ for PEC water splitting is targeted in this thesis. A series of strategies for the innovation of $LaFeO_3$ photocathode are presented from the modification of surface and the tuning of bulk electronic structure. The deposition of TiO_2 film as a hole blocking layer and heterojunction on $LaFeO_3$ leads to the photocurrent onset potential for the hydrogen evolution reaction of +1.47 V vs RHE, which is one of the most positive values reported for a single absorber. The surface co-catalyst loading also generates a 10-fold increase in the photocurrent responses, compared with pristine $LaFeO_3$. With regards to bulk tuning, the substitution of divalent alkaline-earth metal cations into $LaFeO_3$ thin films results in changes in the electronic structure with a strong impact in PEC performance, achieving more than 3 times increase in the external quantum efficiency for solar oxygen reduction. Finally, a novel ferrite-based photoanode, $GaFeO_3$ is discovered for the first time. The structural, optical, and PEC properties of $GaFeO_3$ are systemically reported under the combination of theoretical and experimental studies. These findings have important implications on materials design in the field of solar energy conversion.

Acknowledgements

I believe the journey to a PhD will be one of the most significant and precious memories in my life. Over the past three years, I not only learned numerous knowledge, but also met many great people. I would like to express my deep thanks to them.

First and foremost, I am so grateful to my supervisor Professor David J. Fermin from the depth of my heart. His rigorous scholarship and profound knowledge had grand influences in my mind, which will be an asset in my future research. I am also extremely appreciative for the opportunities, guidance, novel ideas and encouragement I was given while working with David.

I would like to thank Dr. Devendra Tiwari who is a talented scientist. Congratulate Devendra on being a Senior Fellow now. He is an important collaborator in my PhD study. Thank Devendra for sharing loads of chemistry knowledge and research experience with me. Our friendship will be engraved on my mind.

I would like to thank Gael Gobaille-Shaw. He always helped me to deal with many troubles I faced in both study and life. I am very fortunate to meet so nice people.

I would like to thank Yvette Li who was an undergraduate while working with me. Although we just worked 3 months together, I am grateful for her valuable contributions to my project.

I would like to thank Mohammed Alkhalifah for cheering me up and sharing experimental supply with me.

Thank my other lab members (Benjamin Howchen and Muhunthan Nadarajah) and project students (Georgina Plant and Hilary McCarthy) for your kind help.

Thank Mattia Cattelan for supporting me to do the XPS characterisations.

Finally, I would like to specially thank my parents. They played crucial roles in these three years. I fail to make it to the end of the road without their endless love and support.

Author's Declaration

I declare that the work in this dissertation was carried out in accordance with the requirements of the University's Regulations and Code of Practice for Research Degree Programmes and that it has not been submitted for any other academic award. Except where indicated by specific reference in the text, the work is the candidate's own work. Work done in collaboration with, or with the assistance of, others, is indicated at the start of each chapter. Any views expressed in the dissertation are those of the author.

SIGNED: ..... DATE:.....

Contents

Abstract ……I

Acknowledgements ……II

Author's Declaration ……IV

List of Figures ……X

List of Tables ……XVIII

List of Publications ……XIX

List of Abbreviations ……XX

CHAPTER 1.

Introduction 1

1.1 Motivation 2

1.2 Principles and Definitions 5

1.2.1 Semiconductor 5

1.2.2 Photoelectrochemical water splitting cell 8

1.2.3 Tandem photoelectrochemical water splitting cell 11

1.2.4 Band gap and band offset 13

1.2.5 Solar energy conversion efficiency 17

1.3 Recent progress, challenges, and strategies of PEC water splitting 19

1.3.1 Overview of current progress and challenges 19

1.3.2 The selectivity challenges in photoelectrodes 20

1.3.3 PV-grade materials 22

1.3.4 Non-PV-grade materials 24

1.3.5 Strategies for improving efficiency 27

1.3.6 Strategies for improving stability 28

1.3.7 Strategies for optimizing photovoltage 29

1.4 Thesis Outline 31

1.5 References 32

CHAPTER 2.

Experimental set-up and methods 42

2.1 Abstract 43

2.2 Experimental set-up and methods 43

2.2.1 XRD 43

2.2.2 SEM, EDX and TEM 43

2.2.3 XPS 44

2.2.4 Diffuse reflectance and transmittance spectra 44

2.2.5 Photoelectrochemical characterisations 44

2.2.6 Electrochemical characterisations 48

2.2.7 Thin films preparation 49

2.3 References 50

CHAPTER 3.

Heterojunction and cocatalyst for improving the EQE and onset potential of nanostructured $LaFeO_3$ photocathode 51

3.1 Abstract 52

3.2 Introduction 52

3.2.1 Overview of current photocathodes 52

3.2.2 The selection of absorber ($LaFeO_3$) 53

3.2.3 The strategies for improving PEC performance of nanostructured $LaFeO_3$ photocathode 54

3.3 Experimental Section 55

3.3.1 Materials 55

3.3.2 The purifying of FTO substrates 56

3.3.3 The synthesis of $LaFeO_3$ nanoparticles 56

3.3.4 The synthesis of Pt nanoparticles precursor 56

3.3.5 The synthesis of TiO_2 precursor 57

3.3.6 The preparation of various thin film-based photoelectrodes 57

3.4 Results and discussion 57

3.4.1 XRD characterisation of $LaFeO_3$, TiO_2 and Pt nanoparticles 57

3.4.2 Morphology characterisation of $LaFeO_3/TiO_2$ construct 59

3.4.3 Band offsets upon the modification of TiO_2 films and Pt NPs 61

3.4.4 PEC characterisation of various constructs 64

3.4.5 Optimization of TiO_2 film and Pt NPs thickness 67

3.4.6 Quantum efficiency and optical responses of various constructs 70

3.5 Summary 73

3.6 References 73

CHAPTER 4.

Alkaline-earth metal substitution for the enhancement of photoelectrochemical properties in $LaFeO_3$ thin films via promoting active electronic states 77

4.1 Abstract 78

4.2 Introduction 79

4.2.1 The selection of absorber 79

4.2.2 The comparison of different synthesis methods for $LaFeO_3$ photoelectrode 79

4.2.3 Current progress of substituted (doped) $LaFeO_3$ photoelectrode 80

4.3 Experimental Section 82

4.3.1 Materials 82

4.3.2 The preparation of various thin films 82

4.4 Results and discussion 83

4.4.1 XRD characterisation of various $LaFeO_3$ based thin films 83

4.4.2 Morphology characterisation of various $LaFeO_3$ based thin films 86

4.4.3 XPS analysis of various photocathode constructs 87

4.4.4 Optical properties of pristine and 7% AMC substituted LFO thin films . 91

4.4.5 Electrochemical characterisation of various constructs 92

4.4.6 Mott-Schottky plots and valence band edges of various thin films 95

4.4.7 PEC characterisation of pristine and AMC substituted $LaFeO_3$ thin films 98

4.4.8 The role of sub-bandgap states in photoelectrochemical responses .. 103

4.4.9 The stability test of AMC substituted LFO photocathodes 108

4.5 Summary 109

4.6 References 110

CHAPTER 5.

High interfacial hole-transfer efficiency at $GaFeO_3$ thin film photoanodes 114

5.1 Abstract 115

5.2 Introduction 115

5.2.1 Overview of current photoanodes 115

5.2.2 The selection of absorber ($GaFeO_3$) 117

5.3 Experimental Section 119

5.3.1 Materials 119

5.3.2 The preparation of $GaFeO_3$ thin film 119

5.3.3 Computational methods 120

5.4 Results and Discussion 120

5.4.1 The complexity of $GaFeO_3$ structure 120

5.4.2 XPS characterisation of $GaFeO_3$ thin films 123

5.4.3 Optical analysis of $GaFeO_3$ thin films 124

5.4.4 Band composition and energy of $GaFeO_3$ thin films 126

5.5 PEC characterisation of $GaFeO_3$ thin films 130

5.6 Summary 136

5.7 References 137

CHAPTER 6.

Conclusion and future outlook 142

6.1 Conclusion 143

6.2 Future outlook 146

List of Figures

Figure 1-1 Three typical water splitting devices powered by solar energy: photocatalytic particle-based cell (a), decoupled solar water splitting cell (b) and PV devices connected to electrolyzer cell (c). 3

Figure 1-2 Schematic of chemical bond in silicon: (a) intrinsic Si, (b) n-type P-doped Si and (c) p-type B-doped Si. Image reproduced from ref 19, Copyright (2017), Royal Society of Chemistry. Band structure diagram: (d) intrinsic semiconductor, (e) n-type semiconductor and (f) p-type semiconductor. 7

Figure 1-3 Schematic of the process of PEC water splitting: n-type semiconductor (a) and p-type semiconductor (b). 9

Figure 1-4 Band energy of n-type semiconductor-liquid junction (SLJ): in the dark equilibrium (a) and under illumination (b). E^o (H_2O/O_2) is the Nernst potential of H_2O/O_2 redox pair (+1.23 V vs RHE). 11

Figure 1-5 Schematic of the working mechanism of tandem PEC water splitting configuration (a) and an example for the selection of photoelectrodes in tandem PEC cells (b): photocurrent vs. potential plot of photocathode (green line), and two different photoanodes: photoanode 1 (blue line) and photoanode 2 (red line). In order to easily compare the photocurrent density, the photocathodic current (green line) is inverted to positive values, as shown by green dashed line. 12

Figure 1-6 The bandgap energy as a function of theoretical maximum photocurrent magnitude and solar to hydrogen (STH) conversion efficiency under the irradiation of AM 1.5 G solar spectrum (data obtained from The American Society for Testing and Materials G-173 spectrum). 14

Figure 1-7 Schematic of three types of heterojunctions (a) and band diagram of p-n heterojunction before and after equilibrium (b). 15

Figure 1-8 Schematic diagram of recent challenges and strategies for PEC water splitting. 22

Figure 2-1 Photoelectrochemical set-up I. 46
Figure 2-2 Photoelectrochemical set-up II. 47
Figure 2-3 The process of thin films preparation. 49
Figure 2-4 Various precursor solutions (a); and FTO-coated glass substrates before and after the deposition of thin films (b). 50
Figure 3-1 (a) XRD patterns of the LFO, TiO_2 and Pt nanoparticles (NPs) and (b) calculation of coherent diffraction domain size of LFO NPs, using Scherrer equation. 58
Figure 3-2 Morphology of the LFO/TiO_2 photoelectrodes: top view scanning electron micrographs (SEM) image of the LFO film prior (a) and after (b) TiO_2 deposition; cross-sectional SEM image (c) and EDX maps (d) of LFO/TiO_2 films, revealing domains associated with FTO, LFO and TiO_2. 60
Figure 3-3 The schematic diagram of the cross-sectional EDX analysis: the electron beam moves from glass to FTO (a) and to samples (b). 61
Figure 3-4 Cyclic voltammograms of the various constructs recorded at 50 mV s^{-1} in Ar-purged aqueous 0.1 M Na_2SO_4 solution at pH 12 in the dark (a); Mott-Schottky plot of LFO in Ar-saturated 0.1 M Na_2SO_4 aqueous solution at pH 12 (b); and estimation of the band alignment of LFO and TiO_2 before and after the formation of the heterojunction, based on the Mott-Schottky plot of LFO and the majority carrier density of the order of 10^{17} cm^{-3} in the TiO_2 film (c). 63
Figure 3-5 Photoelectrochemical responses of various nanostructured photocathodes in Ar-saturated 0.1 M Na_2SO_4 aqueous solutions (pH 12) under the illumination at 464 nm: (a) cycling voltammogram of LFO and LFO/TiO_2 under photon flux of 2.17×10^{15} cm^{-2} s^{-1}; (b) transit photocurrent responses under photon flux of 3.44×10^{15} cm^{-2} s^{-1}; and (c) photocurrent ratio of three LFO-based constructs to pristine as a function of potential. 65
Figure 3-6 Cyclic voltammograms of TiO_2 with different thickness coated onto FTO substrate in a solution containing 1 mM $K_4Fe(CN)_6$ and 0.1 M KNO_3 measured at a

scan rate of 50 mV s^{-1}(a); and photocurrent potential curves of as-deposited LFO films and after modified by TiO_2 with different thickness, measured in Ar-saturated 0.1 M Na_2SO_4 aqueous solution (pH 12) and a photon flux of 3.44×10^{15} cm^{-2} s^{-1}(b). 68
Figure 3-7 Photocurrent transient measurements of the LFO/TiO_2 with different Pt nanoparticles loading amount at different potentials in Ar-saturated 0.1 M Na_2SO_4 aqueous solution (pH 12) under illumination of 464 nm and photon flux of 3.44×10^{15} cm^{-2} s^{-1}. 70
Figure 3-8 Quantum efficiency spectra of LFO based photocathodes at +0.5 V vs RHE in Ar-saturated 0.1 M Na_2SO_4 aqueous solution at pH 12: (a) external quantum efficiency spectra of various constructs and (b) internal and external quantum efficiency spectra of the LFO photoelectrode; Optical properties of the LFO film: (c) diffuse reflectance and transmittance spectrum, (d) absorption spectra, (e) Tauc plot analysis; and (f) equivalent plots estimated from the EQE spectra of the various photoelectrode constructs. Red arrows show the linear fitting of the Tauc plot, indicating two distinctive transitions in LFO. 71
Figure 4-1 XRD of alkaline-earth metal cation (AMC) substituted $LaFeO_3$ (LFO) thin films: XRD patterns of pristine and 3% Ba^{2+} substituted LFO thin films (a), showing the key features associated with the pm-3m cubic phase. Evolution of the (110) peak upon 7% substitution of the various AMC (b) and as a function of the extent of Ba^{2+} (c), Mg^{2+} (d), Ca^{2+}(e), and Sr^{2+}(f) substitution. 83
Figure 4-2 XRD patterns of the pristine and 7% AMC substituted LFO refined to the pm-3m cubic phase JCPDS-ICDD database file 01-075-0541 (a). The bule line represents the difference between observed (black) and calculated (red) XRD patterns. Lattice constant of substitution of the various AMC (b) and as a function of the extent of Mg^{2+}, Ca^{2+}, Sr^{2+} and Ba^{2+} substitution (c) extracted from full-profile structural Pawley refinement. The ionic radius ratio of AMC to La^{3+} (b). 85

Figure 4-3 Top view scanning electron micrographs (SEM) of bare FTO-coated glass substrate and LFO-based thin films (a). Energy dispersive analysis of X-rays (EDX) spectra of pristine and AMC substituted LFO thin films (b). 86
Figure 4-4 X-ray photoelectron spectroscopy for the survey of pristine and AMC substituted LFO thin films: 7% substitution of the various AMC (left) and as a function of the extent of Ba^{2+} (right)..... 88
Figure 4-5 Deconvolution of La 3d, Fe 2p, O 1s XPS bands of 7% Sr substituted LFO thin film. All constructs show a similar deconvolution pattern. 89
Figure 4-6 Evolution of the XPS spectra in the regions of Fe 2p (a,c) and O 1s (b,d) upon 7% AMC substitution and extent of Ba^{2+} substitution. The dashed lines show the shift of binding energies upon substitution. 90
Figure 4-7 Correlation between binding energies (BEs) of Fe $2p_{3/2}$ and O 1s (perovskite lattice) in pristine and AMC substituted LFO films. This trend strongly suggests that Fe oxidation state and covalency of the Fe-O bond are strongly correlated..... 91
Figure 4-8 Optical properties of 95 nm pristine and 7% AMC substituted LFO thin films: (a) transmittance and reflectance spectra in the visible range and (b) Tauc plots showing the main absorption edge at 2.72 eV. Dashed arrows show the linear fit of pristine film, indicating two clear distinctive transitions. 92
Figure 4-9 Electrochemical responses in 0.1 M Na_2SO_4 pH 12: (a) cyclic voltammograms of pristine and 7% AMC substituted LFO films at 0.1 V s^{-1}; (b) cyclic voltammograms as a function of the Ba^{2+} substitution extent at 0.1 V s^{-1}; and (c) Capacitance voltage curves extracted from electrochemical impedance spectra of pristine and 7% AMC substituted films, highlighting the pseudo-capacitive elements associated with A and B sub-bandgap states. 93
Figure 4-10 Mott-Schottky plots of LFO based thin films in 0.1 M Na_2SO_4 aqueous solutions at pH 12: (a) pristine, (b) 7% AMC substitution and (c) 17% Mg^{2+}

substitution. Dashed arrows show the fit of the Mott-Schottky plots. The linear fitting in (b) employs the data of the 7% Sr^{2+} substituted LFO thin film. 96
Figure 4-11 Valence band edge calculated from XPS analysis of the pristine and 7% AMC substituted films. The valence band edge of pristine and 7% Sr^{2+} substituted LFO is 0.53 eV and 0.85 eV with reference to Fermi level, respectively. 98
Figure 4-12 Photoelectrochemical responses in O_2-saturated 0.1M Na_2SO_4 aqueous solution pH 12: (a-f) 5 mV s^{-1} linear sweep voltammetry of pristine and AMC substituted LFO thin films under a square wave 405 nm light perturbation and photon flux of 3.25×10^{15} cm^{-2} s^{-1}; and (g) photocurrent response at +0.45 V vs RHE as a function of the type and extent of AMC substitution. 99
Figure 4-13 External quantum efficiency spectra for the pristine and 7% AMC substituted thin films (a); and Tauc plot representation of the EQE (b). Dashed arrows show the linear fit of pristine (black), Mg^{2+} substituted (yellow) and Sr^{2+} substituted (green) LFO, demonstrating that charge carriers are generated only above the 2.72 (±0.02) eV edge. 101
Figure 4-14 Linear sweep voltammetry (LSV) of pristine and AMC substituted LFO thin films in Ar-saturated 0.1M Na_2SO_4 aqueous solution pH 12: (a) 7% AMC substitution; and (b-f) different extents of AMC substitution. LSV were recorded at 5 mV s^{-1} and under square wave light perturbation (405 nm and 3.25×10^{15} cm^{-2} s^{-1} photon flux)..... 102
Figure 4-15 Schematic representation of the position of valence band edge as well as of the hydrated A- and B-states for pristine and AMC substituted LFO thin films. A-states are linked to intrinsic defects linked to cation disorder, while B-states are a combination of O 1s and Fe 3d states associated with high Fe-oxidation states..... 104
Figure 4-16 Dynamic photocurrent transient responses of pristine and 7% Ba^{2+} substituted LFO thin films at +0.45 V vs RHE in a 0.1M Na_2SO_4 aqueous solution (pH 12): under Ar-saturated solutions (a) and O_2-saturated solutions (c); Photocurrent transients normalised by the maximum photocurrent: Ar-saturated solutions (b) and

O_2-saturated solutions (d). The thin films are illuminated with a 405 nm LED (3.25×10^{15} cm^{-2} s^{-1} photon flux). 105
Figure 4-17 Electrochemical responses of pristine and Ba^{2+} substituted LFO thin films recorded at 5 mV s^{-1} in O_2-saturated Na_2SO_4 aqueous solutions (pH 12) in the dark. 106
Figure 4-18 Stability test of 7% AMC substituted LFO thin films in O_2-saturated Na_2SO_4 aqueous solutions (pH 12) under illumination of a 405 nm LED (3.25×10^{15} cm^{-2} s^{-1} photon flux): LSV plots after preparation (a), after 1 hour of continuous illumination (b), after 45 days exposed to air (c) and photocurrent density extracted from Figure a, b and c vs. time plots at +0.4 V vs RHE (d). 108
Figure 5-1 $GaFeO_3$ (GFO) structural complexity: (a) powder XRD with quantitative Rietveld analysis; (b) schematic of the GFO unit cell, featuring Ga (purple) and Fe (green) sites with tetrahedral and octahedral coordination geometries; (c) HR-TEM of GFO powder with lattice fringes associated with {221} planes; (d) cross-sectional SEM image of a GFO film obtained after 10 coating steps onto FTO glass; (e) EDX spectrum recorded at the top of the film after dc-sputter coating a 20 nm Ag layer; and (f) Raman spectrum of GFO films under 514 nm excitation, featuring 27 modes deconvoluted using Voigt functions. 121
Figure 5-2 Surface composition analysis of GFO thin films using XPS: (a) survey spectrum showing the different photoemissions features; (b) Ga 2p core-level; (c) O 1s core-level; and (d) Fe 2p core-level. Spectral deconvolution is performed using Gaussian-Lorentzian mix functions. 124
Figure 5-3 Optical properties of GFO thin films: (a) transmittance and reflectance spectra for a 350 nm GFO film; (b) absorption spectrum constructed from (a); (c) Tauc plot for bandgap determination assuming direct band-band transitions; (d) energy-differential absorption spectrum along with symmetry assignment for ligand-field (LFT) and charge-transfer transitions (C-T); and (e) modified TS diagram

for Fe^{3+} in tetrahedral and octahedral field depicting the electronic configuration of states associated with the optical transitions. 125
Figure 5-4 Bands composition and structure: (a) valence-band spectrum of a GFO thin film measured under Al-Kα X-ray excitation; (b) density of states (DOS) and (c) band structure of GFO calculated employing hybrid density functional theory (DFT) with HSE06 functional. 127
Figure 5-5 Flat band energy: (a) capacitance voltage curves extracted from electrochemical impedance spectroscopy of 350 nm GFO film in Ar-saturated 0.1M Na_2SO_4 aqueous solutions (pH 12) and (b) Mott-Schottky plot. 128
Figure 5-6 Band-alignment of GFO band-edges with respect to common electron-transport (ETL)[37] and hole-transport layers (HTL).[37] Band offset with other Fe based photoelectrodes including $LaFeO_3$ (LFO),[38] $YFeO_3$ (YFO),[31] $BiFeO_3$ (BFO),[39] $CaFe_2O_4$ (CaFO),[40] $CuFeO_2$ (CuFO),[41] $ZnFe_2O_4$ (ZFO),[42] and Fe_2O_3,[43] illustrates how deep is the VBM in GFO. The construction of the GFO band diagram is identical to Figure 4-15, as shown in section 4.4.8. 129
Figure 5-7 Photoelectrochemical responses of 350 nm GFO thin films: (a) linear sweep voltammetry (LSV) recorded at 5 mV s^{-1} under square wave 405 nm light perturbation and 4.25 × 10^{15} cm^{-2} s^{-1} photon flux in Ar-saturated 0.1M Na_2SO_3 and Na_2SO_4 electrolytes (pH 12); (b) the yield of surface and bulk charge transfer estimated from (a); (c) IQE at +1.4 V vs RHE as a function of wavelength; (d) Tauc plot analysis of IQE data; and (e) potential-dependence of IQE in Ar-saturated 0.1M Na_2SO_3 electrolytes (pH 12), along with fits to the Gärtner model (Eqn. 5-1). 130
Figure 5-8 Thickness dependence of photocurrent responses and PEC stability test: (a) LSV responses of films with a thickness between 110 and 350 nm in Ar-saturated 0.1M Na_2SO_3 aqueous solutions at pH 12; photocurrent responses under the back and front illumination at 350 nm (b) and 110 nm (c) films; (d) photocurrent transient responses at 350 and 110 nm GFO films at +1.2 V vs. RHE; and (e) stability test of 350 nm film under a 405 nm continuous irradiation. 133

Figure 5-9 The effect of Ga:Fe ratio: (a) $Ga_xFe_{2-x}O_3$ photocurrent responses as a function of Ga:Fe ratio (x values) in the sol-gel precursor; Scan rate, wavelength, and photon flux values are as indicated in Figure 5-8a; (b) representative XRD patterns of $Ga_xFe_{2-x}O_3$ (x=1 and 0.7); and (c) cyclic voltammograms of $Ga_xFe_{2-x}O_3$ thin films, recorded at 100 mV s^{-1} in the dark in Ar-saturated 0.1M Na_2SO_3 aqueous solutions (pH 12). 135

List of Tables

Table 1-1 PEC performance of some attractive ternary oxides……..26

Table 3-1 The coherent diffraction domain sizes of LFO NPs estimated from each peak.……59

Table 3-2 Phenomenological first-order electron transfer rate for the oxidation of $Fe(CN)6^{4-}$ at TiO_2 modified electrodes…..……69

List of Publications

(1) Sun, X.; Tiwari, D.; Fermin, D. J. Nanostructured $LaFeO_3$ Photocathodes with Onset Potentials for the Hydrogen Evolution Reaction Over 1.4 V vs. RHE. *J. Electrochem. Soc.* **2019**, *166*, H764–H768.

(2) Sun, X.; Tiwari, D.; Fermin, D. J. Promoting Active Electronic States in $LaFeO_3$ Thin-Films Photocathodes via Alkaline-Earth Metal Substitution. *ACS Appl. Mater. Interfaces* **2020**, *12*, 31486−31495.

(3) Sun, X.; Tiwari, D.; Fermin, D. J. High Interfacial Hole-transfer Efficiency at $GaFeO_3$ Thin Film Photoanodes, *Adv. Energy Mater.* **2020**, *10*, 2002784.

List of Abbreviations

Abbreviation	Definition
PEC	photoelectrochemical
PV	photovoltaics
PC	photocatalytic
PV+E	photovoltaic devices connected to electrolyzer
LCHG	levelized costs for hydrogen generation
ALD	atomic laser deposited
HER	hydrogen evolution reaction
OER	oxygen evolution reaction
SLJ	semiconductor/liquid junction
SCR	space charge region
E_F	Fermi level
FLP	Fermi-level pinning
VB	valence band
CB	conduction band
VBM	valence band maximum
CBM	conduction band minimum
STH	solar-to-hydrogen
ABPE	applied bias photon-to-current conversion efficiency
IPCE	incident photon-to-electron conversion efficiency
EQE	external quantum efficiency
APCE	absorbed photon-to-current conversion efficiency
IQE	internal quantum efficiency

AM 1.5 G	Air Mass 1.5 Global
CV	cyclic voltammetry
LSV	linear sweep voltammetry
TP	transit photocurrent
QE	quantum efficiency
EIS	electrochemical impedance spectra
XRD	X-ray diffraction
SEM	scanning electron microscopy
EDX	energy-dispersive X-rays
HR-TEM	high-resolution transmission electron microscopy
XPS	X-ray photoelectron spectroscopy
RHE	reversible hydrogen electrode
NHE	normal Hydrogen Electrode
FTO	$F:SnO_2$
LFO	$LaFeO_3$, lanthanum iron oxide
NPs	nanoparticles
AMC	alkaline-earth metal cation
GFO	$GaFeO_3$, gallium iron oxide
BE	binding energies
U_{fb}	flat band potential
CIF	crystallographic information file
$\eta_{surface}$	surface charge transfer efficiency
η_{bulk}	bulk charge transfer efficiency

CHAPTER 1.

Introduction

1.1 Motivation

The World Energy Council has reported that our planet has been seeing an unprecedented growth of energy consumption, mainly dominated by the combustion of fossil fuels, such as coal, oil, and natural gas. This behaviour poses a major threat to our future due to the limited quantities of non-renewable sources, for example, the oil will eventually be consumed without further action.[1] On the other hand, the burning of fossil fuels emits large quantities of carbon dioxide, leading to global climate change.[2] There are many formidable challenges in the current global energy system. As elaborated by the Journal of the Economist[3], it is necessary to completely transform our current energy consumption system from traditional fossil fuel combustion to the usage of sustainable resources. Developing sustainable energies (e.g., solar, hydroelectricity and wind) has the potential to be the replacement for those fossil fuels, achieving zero-carbon energy consumption and sustainable development.[4] Solar energy shows promising properties to be applied among them, as it contains decentralized and inexhaustible power. Specifically, there is approximately 430 quintillion joules (430×10^{18} J) of solar energy reaching our land every hour; by contrast, the global energy demand is 410 quintillion joules in a year.[5] This means only converting and storing the solar energy that hits the Earth within an hour can satisfy the whole year human energy consumption. However, the major issues for the usage of solar energy are its conversion and storage. Currently, both photovoltaics (PV) and artificial photosynthesis including related process are two active research areas for sunlight transformation and storage.

The past decade witnessed the flourishing development of PV devices for electricity production from a theoretical idea to a practical and reliable technology.[6] For example, there has been a dramatic increase in global production of the various solar cells from 21 GW in 2010 to 129 GW in 2019.[7] Meanwhile, the cost of

production in the range of $50–$100 per W since 1976 has dropped to $0.5 per W in 2018.[8] However, it should be noted that the storage of electricity generating from PV devices requires batteries, which is the significant factor to increase the overall production cost.[9] Alternatively, it is possible to convert sunlight to fuels which could be an efficient and long-term strategy to employ and store solar energy.[10]

Hydrogen as an attractive solar fuel can be applied in many fields, such as heating, driving vehicle and material refining.[11] Water photoelectrolysis is a well-known technology for the production of solar hydrogen.[4] The semiconductor in the process of solar water splitting acts as light absorber and energy converter, collecting and storing solar power in chemical bonds, H_2 and/or O_2.

Nowadays, the prototypes of solar water splitting can be classified into three configurations.[9,12] As shown in Figure 1-1, they are photocatalytic (PC) water splitting (a) based on particle suspensions, film-based photoelectrochemical (PEC) water splitting (b) and PV-based electrolysis water splitting (c). The decoupled configurations have in principle more disadvantages than integrated systems, though the maximum theoretical solar-to-hydrogen (STH) convention efficiency of the former is larger than the later. The integrated PEC absorbers could possess a cooler

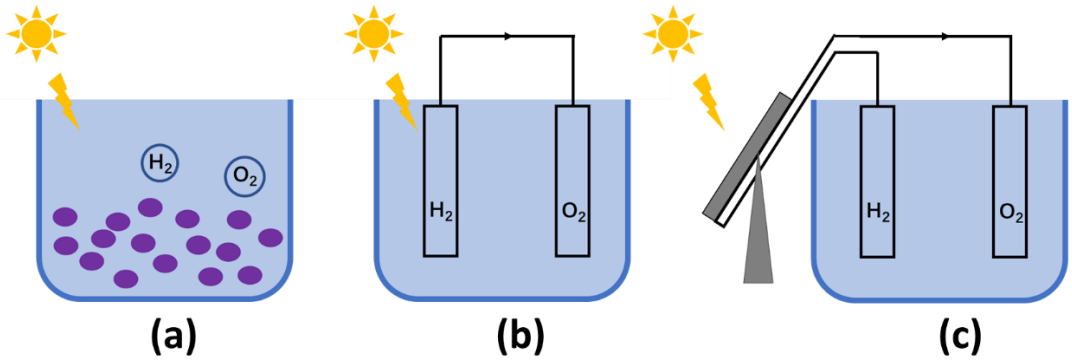

Figure 1-1 Three typical water splitting devices powered by solar energy: photocatalytic particle-based cell (a), decoupled solar water splitting cell (b) and PV devices connected to electrolyzer cell (c).

reaction atmosphere than decoupled systems owing to the presence of electrolyte solutions, which is beneficial to the achievement of high photovoltage and energy conversion efficiency in the process of PEC water splitting from a thermal point of view.[13] In addition, the direct water splitting using solar energy reduces the external energy loss (e.g., external interfaces) in comparison with PV devices connected to electrolyzer (PV+E) systems. From an economic perspective, with identical STH conversion efficiency of 9.8%, the levelized costs for hydrogen generation (LCHG) are \$11.4 kg^{-1} and \$12.1 kg^{-1} for PEC systems and PEC+E system, respectively.[14] In this case, PEC systems have cost-advantages in comparison with PEC+E systems, because the PEC+E systems require additional costs for the electricity transport and conditioning from the PV device to the electrolyzer, increasing the overall cost, as estimated by Lewis's group.[14] However, the LCHG of grid assisted PEC+E system can be lowered to \$5.5 kg^{-1} under the same STH conversion efficiency of 9.8%. The LCHG is highly dependent of energy conversion efficiency.[14] Obviously, the increase of energy conversion efficiency can lead to the cost reduction due to the areal dependencies of some components (e.g., photoabsorbers).[14-16] For example, the concentrated PEC system shows a STH conversion efficiency of 20%, thereby lowering the LCHG to \$9.2 kg^{-1}.[14] As for particulate PC systems, Pinaud et al. reported that its LCHG are as low as \$1.6-3.2 kg^{-1} under the STH conversion efficiency of 10%.[16] Although the estimation methods of LCHG for PC systems may be slightly different from that for the other two systems mentioned above, it is clear and unambiguous that LCHG for PC systems is relatively cheap compared with PEC and PV+E systems under the similar STH conversion efficiency of 10%.[17] However, it should be mentioned that the STH conversion efficiency of current PC systems can only reach around 1%;[16-18] in contrast, it is possible for current PEC and PV+E systems to achieve a STH conversion efficiency of 10%, which will be shown in the following sections. This means the current LCHG of PC systems are far higher than \$1.6-3.2 kg^{-1}. In addition, due to the particle-based systems, a number of scientific

characterisations such as photoelectrochemical measurement fails to characterise the advantages and/or disadvantages of PC systems, limiting the further investigation to a certain extent.[17,18]

Due to the maturity of PV technology, the use of the PV+E systems tends to be commercially available to produce solar hydrogen. However, the progress in all PEC water splitting devices is being slowly developed and beset with numbers of challenges, such as prototype design, conversion efficiency, system stability, and sustainability. These represent significant hurdles for the scalable application of PEC water splitting technologies.[8] Based on the above, this thesis will focus on the innovation of direct PEC water splitting cells. It is hoped that feasible strategies can be found to overcome those formidable challenges.

1.2 Principles and Definitions

This section introduces some key principles and definitions in the field of PEC water splitting, such as the working mechanism of photoelectrodes, band offset and various expressions of energy conversion efficiency.

1.2.1 Semiconductor

Semiconductors as solar energy absorbers are the basis of the development of PEC water splitting technology. Since Thomas J. Seebeck discovered the properties of semiconductor in 1821, semiconductors have a profound influence in the history of science. When there is no thermal vibration (e.g., zero Kelvin), part of energy bands in semiconductor are completely filled with electrons, whereas the rest of the energy bands are empty. There is a gap between the highest occupied electron states (valence band) and the lowest range of vacant electronic energies (conduction band), referred as to band gap. The electrical conductivity of semiconductors is between that of insulators and conductors, which is typically sensitive to various factors such as temperature, purity, and illumination. For example, at low temperature (e.g., zero

Kelvin), the electrons in semiconductor are bound in their respective bonds, leading to the nature of insulator. However, at room temperature, some covalent bonds are broken in semiconductor owing to the thermal vibration; consequently, the free electrons can move from valence band to conduction band, leaving holes in the valence band. The conduction band and valence band are typically both partially occupied by electrons in semiconductor, hence giving conduction. In the fields of solar energy conversion such as photocatalysis, PEC water splitting, and artificial photosynthesis, semiconductors are usually excited through sunlight with energy higher than bandgap, leading to the formation of photogenerated charge carriers. The photogenerated electrons and holes can transfer from conduction band and valence band of semiconductors to various chemical reactions.

An intrinsic semiconductor, however, typically cannot be directly used in such fields owing to its poor electrical conductivity at room temperature. Introducing impurities or 'doping' into intrinsic semiconductor is an effective approach to not only enhance its conductivity but also modulate the characteristics of electrical conductivity in semiconductors. For example, in silicon introducing electron donors (e.g., phosphorus atoms) or electron acceptors (e.g., boron) can lead to two different conduction behaviour.[19] The phosphorus atom has more valence electrons than silicon, as illustrated in Figure 1-2b; thus the phosphorus doped silicon is an electron-rich semiconductor (n-type), in which the majority charge carriers are electrons. The extra free electrons lead to the formation of a donor level that is close to conduction band, as shown in the band structure (Figure 1-2e). Therefore, the small energy gap enables the free electrons at the donor level to easily transfer to conduction band, thereby increasing the conductivity. As for boron doped silicon (Figure 1-2c), the dopant atom with fewer valence electrons than the host atom results in a hole-rich semiconductor (p-type), in which holes are the majority charge carriers. There is an acceptor level close to valence band in p-type semiconductor, as

shown in Figure 1-2f, due to the hole-rich property. Similarly, electrons from valence band can easily move to the acceptor level, leaving holes in the valence band, which contributes to the conductivity of p-type semiconductor.

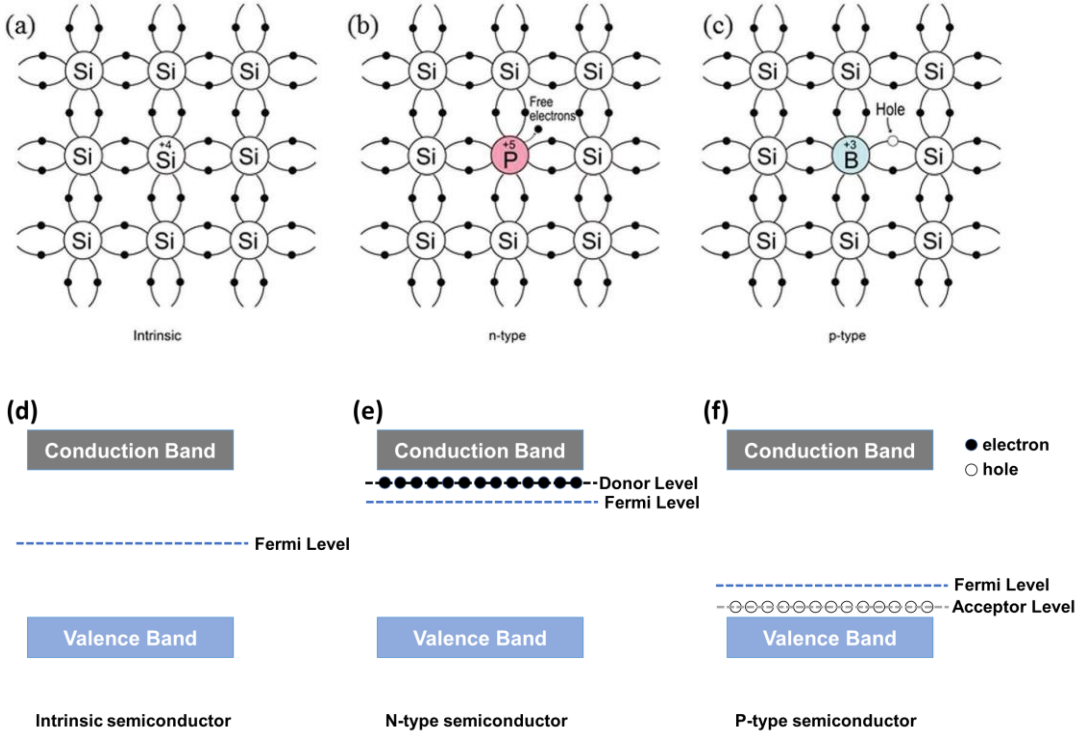

Figure 1-2 Schematic of chemical bond in silicon: (a) intrinsic Si, (b) n-type P-doped Si and (c) p-type B-doped Si. Image reproduced from ref 19, Copyright (2017), Royal Society of Chemistry. Band structure diagram: (d) intrinsic semiconductor, (e) n-type semiconductor and (f) p-type semiconductor.

Fermi level is another significant concept in the discussion of the semiconductors. The Fermi level is the highest energy level that an electron can occupy at absolute zero. The Fermi level of intrinsic semiconductor is located at the middle of the bandgap because there are no states in the bandgap, as shown in Figure 1-2d. But dopants can enable the distribution of electrons to alter in intrinsic semiconductors. As for the Fermi level of n-type semiconductor (Figure 1-2e), it is located close to conduction band, since the concentration of electrons in the conduction band is greater than that of holes in the valence band. In contrast, the Fermi level of p-type

semiconductors shown in Figure 1-2f shifts towards valence band, owing to the larger number of holes in the valence band in comparison with the number of electrons in the conduction band. It should be noted that the Fermi level positions discussed above are at thermodynamic equilibrium. When the thermodynamic equilibrium of a semiconductor is disturbed, the populations of charge carrier in the valence band and conduction band will accordingly change. If the disturbance (e.g., illumination) is not too great, the electrons and holes will respectively reach a state of quasi thermodynamic equilibrium. Therefore, quasi-Fermi level is introduced to describe the population of charge carrier in semiconductor band at thermodynamic nonequilibrium, using Fermi-Dirac statistics. This will be further discussed in next section.

1.2.2 Photoelectrochemical water splitting cell

Direct PEC water splitting technology employs n-type and/or p-type semiconductors to convert solar energy to electrolyse water and generate hydrogen and/or oxygen. Different methods (as elaborated in the following chapters) can be used to process semiconductors in a thin film form which can be employed as photoelectrodes in PEC water splitting cells. As a n-type semiconductor leads to PEC water oxidation reaction evolving oxygen and is thus referred to as photoanode. Whilst p-type semiconductor facilitates PEC water reduction reaction evolving hydrogen, thus referred to as a photocathode. The process of PEC water splitting can be briefly summarised into three steps: (i) semiconductor harvests solar energy to produce numbers of electron-hole pairs. (ii) these photogenerated charge carriers are separated and moved to the photoelectrode/electrolyte interface. (iii) different species in the water consume them to generate H_2 and O_2. The reactions of (iii) depend on pH of the electrolyte, as follows:

In acidic conditions: $2H^+ + 2e^- \rightarrow H_2$ (photocathode)

$$H_2O \rightarrow 1/2O_2 + 2H^+ + 2e^- \text{ (photoanode)}$$

In alkaline conditions: $2H_2O + 2e^- \rightarrow H_2 + 2OH^- \text{ (photocathode)}$

$$2OH^- \rightarrow 1/2O_2 + H_2O + 2e^- \text{ (photoanode)}$$

Figure 1-3 illustrates the working mechanism of photoanode (a) and photocathode (b), when they are immersed in electrolyte for direct solar water splitting. With regards to n-type semiconductor, the position of its Fermi level (E_F) is close to conduction band (CB) edge and is usually lower than water oxidation potential (+1.23 V vs RHE), as shown in Figure 1-3a. Therefore, at equilibrium between semiconductor - liquid junction (SLJ), the electrons from n-type semiconductor flow

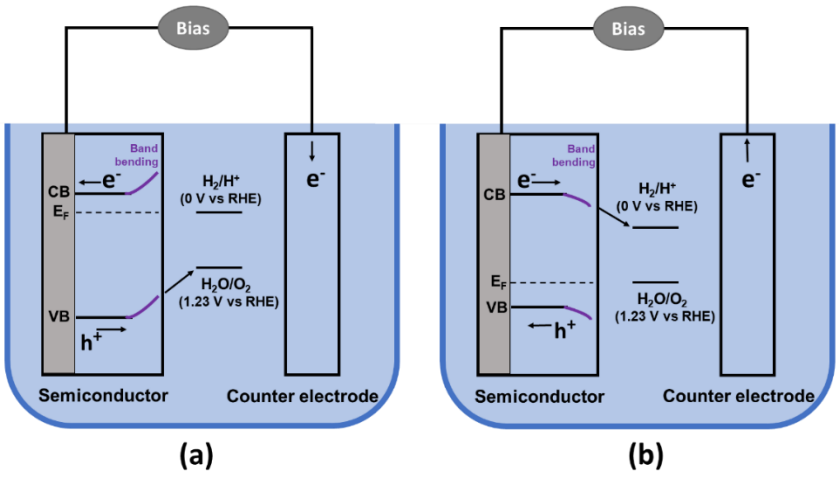

Figure 1-3 Schematic of the process of PEC water splitting: n-type semiconductor (a) and p-type semiconductor (b).

into solutions, leading to an upwards band bending. Similarly, photocathode shows a downwards band-bending owing to a transfer of electrons from electrolytes to photocathode, as the Fermin level of a p-type semiconductor, close to valence band (VB) edge, is typically higher than water reduction potential (0 V vs RHE).[20] The band bending can be altered through external bias. The potential that can change the semiconductor band from bending to flat is called flat band potential (U_{fb}). The band bending due to movement of charge carriers between semiconductors and

electrolyte also creates an electrically neutral region, named as space charge region (SCR).[19,21] This SCR results in a potential barrier at SLJ, restricting the minority carriers to move in the same direction as majority carriers, thus offering a driving force for the separation and transfer of photogenerated electrons and holes, which then takes part in PEC water splitting.

Taking n-type semiconductor as an example, Figure 1-4 contrasts the band energy of semiconductor-liquid junction in the dark and under illumination, indicating a decrease of SCR upon illumination due to the separation of photogenerated charge carriers. At dark equilibrium, the barrier height (V_{max}) shown in Figure 1-4a determines the theoretical maximum voltage that can be acquired from an electron-hole pair at the SLJ junction. When the semiconductor is illuminated (Figure 1-4b), the Fermi level will split to electron quasi-Fermi level (E_{qFn}) and hole quasi-Fermi level (E_{qFp}), as mentioned in previous section. The photovoltage (V_{ph}) is given by the difference between the quasi-Fermi level of electron and hole under illumination. Prior to the following discussion, the difference between 'photovoltage' and 'onset potential' needs to be explained. There are various definitions of onset potential. In general, when the photocurrent appears in photocurrent vs potential curve, the corresponding potential is referred as to onset potential. It should be noted that high photovoltage obtained from one semiconductor may not be able to achieve the enhancement of photocurrent onset potential in this semiconductor owing to the presence of an overpotential. The following section will introduce the formation of overpotential and strategies for overcoming it. Although 'photovoltage' is different from 'onset potential' in a strict sense, the improvement of the photocurrent onset potential is synonymous with the increase of photovoltage in this thesis, which has also been widely used in the field of PEC water splitting.

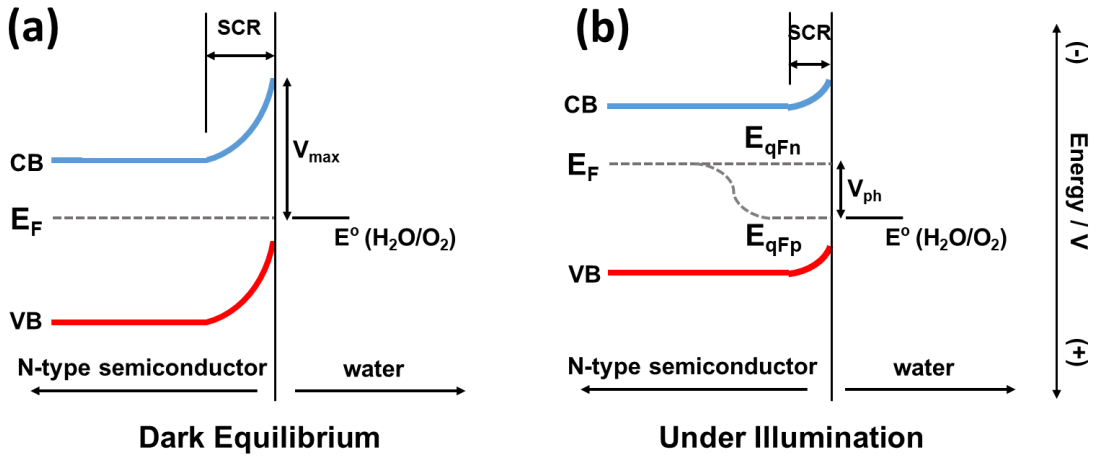

Figure 1-4 Band energy of n-type semiconductor-liquid junction (SLJ): in the dark equilibrium (a) and under illumination (b). E^o (H_2O/O_2) is the Nernst potential of H_2O/O_2 redox pair (+1.23 V vs RHE).

1.2.3 Tandem photoelectrochemical water splitting cell

The section 1.2.2 introduces a PEC water splitting cell built up from an isolated photoanode or photocathode with a counter electrode (e.g., glassy carbon and platinum) i.e. a half-cell. However, this system usually requires external driving force for PEC water splitting. Therefore, for unassisted water splitting technologies, a tandem PEC water splitting cell integrating two absorbers one n-type (photoanode) and second a p-type semiconductor (photocathode) is developed, as shown in Figure 1-5a. Each semiconductor facilitates one half of the water redox reaction. The advantages of tandem PEC cell are high conversion efficiency and being external bias-free.[22-24] For example, the solar-to-hydrogen (STH) conversion efficiency of tandem devices has the potential to reach up to 25%, which is much larger than that of single photoelectrode (below 15%).[25-27]

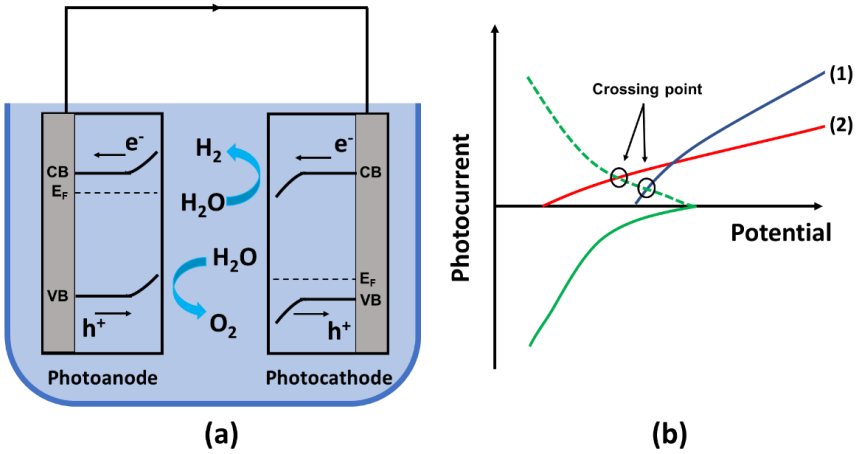

Figure 1-5 Schematic of the working mechanism of tandem PEC water splitting configuration (a) and an example for the selection of photoelectrodes in tandem PEC cells (b): photocurrent vs. potential plot of photocathode (green line), and two different photoanodes: photoanode 1 (blue line) and photoanode 2 (red line). In order to easily compare the photocurrent density, the photocathodic current (green line) is inverted to positive values, as shown by green dashed line.

In general, a wide bandgap n-type semiconductor is coupled with a narrow bandgap p-type semiconductor. This enables both absorbers to be illuminated at the same time, as the sunlight could go through wider bandgap photoanode first and those lower energy light cannot be used will be absorbed by the narrower bandgap photocathode.[28] Therefore bandgap is one of the factors that influence the options of two photoelectrodes. However, to achieve high conversion efficiency in tandem PEC water splitting devices, in practice, a more critical factor is the photocurrent onset potential.[29,30] The photoanode with a relatively negative onset potential will be attractive; by contrast, it is favourable for photocathode to have a positive onset potential. This is illustrated in Figure 1-5b. It is clear to see that photoanode 1 has a more positive onset potential and an overall larger photocurrent magnitude than photoanode 2. Though when it comes to the choice of photoanode to be integrated with the photocathode in Figure 1-5b, the desired option is photoanode 2. Because the photocurrent density of photoanode 2 is higher than photoanode 1 at the crossing point (circled in Figure 1-5b) between photoanode and photocathode that

represents the maximum photocurrent that both side photoelectrodes can achieve at a single potential. Photoanode 1 shows higher photocurrent density; however, the relatively positive onset potential restricts its suitability to a certain degree.

It is worth mentioning that although tandem PEC water splitting cells tend to perform better than single PEC cells, tuning two separate sets of criteria of stability, properties and activity for two different absorbers, makes developing tandem devices challenging.[31] An alternative strategy could be developing bifunctional photoelectrodes such as Bi_2WO_6[32] that can be used simultaneously for hydrogen evolution reaction (HER) and oxygen evolution reaction (OER). However, this requires the semiconductor with a suitable band alignment with its conduction band position should be higher than water oxidation potential, and its valence band position should be lower than water reduction potential. Yet, it is not easy to find too many materials with such band positions, since the band alignment of most semiconductors is only suitable for either HER or OER. As elaborated by Spitler et al., discovering novel materials is one of the main challenges in the development of tandem PEC water splitting technology.[33]

1.2.4 Band gap and band offset

As can be inferred from the above discussion that the bandgap is an essential parameter for solar water splitting. Bandgap energy is the difference between the valence band top and conduction band bottom of the semiconductor. It links to not only the band alignment of the semiconductor but also translates to available energy or photovoltage for PEC water splitting. A theoretical maximum photovoltage of PV devices is typically less than bandgap energy (around 400 mV) under standard conditions, except those ferroelectric materials.[34] According to Nernst equation, the conversion of one molecule of H_2O to H_2 and 1/2 O_2 ($H_2O \rightarrow H_2 + 1/2O_2$) requires the free energy change of $\Delta G = 237.2$ kJ/mol that equals to $\Delta E_o = 1.23$ V per electron transferred under standard conditions. This means, in an ideal case, the input

electricity should be higher than 1.23 V to split water. When it comes to the energy input in PEC water splitting devices, ideally the bandgap for photoelectrodes should be 1.6 - 2.4 eV.[28] These values additionally consider the energy losses attributed to the concentration and kinetic overpotentials for HER and OER in the process of charge transfer.[35] A wide bandgap can offer large driving forces, especially for unassisted PEC water splitting cells. However, Figure 1-6 shows the relationship between bandgap energy, theoretical maximum photocurrent magnitude and STH conversion efficiency under the irradiation of Air Mass 1.5 Global (AM 1.5 G) solar, indicating that the narrower bandgap materials can achieve much higher photocurrent and therefore solar-to-hydrogen (STH) conversion efficiency.

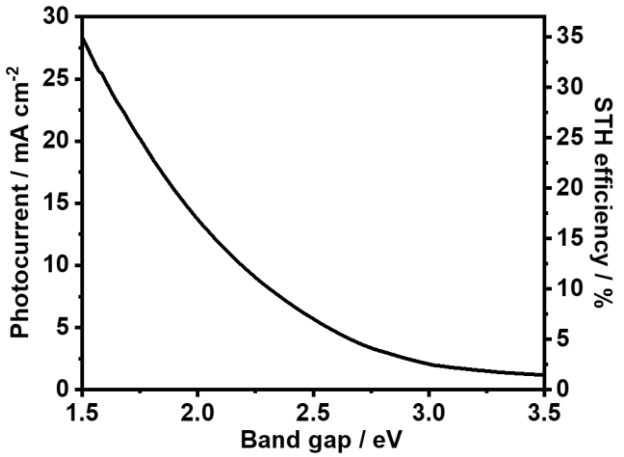

Figure 1-6 The bandgap energy as a function of theoretical maximum photocurrent magnitude and solar to hydrogen (STH) conversion efficiency under the irradiation of AM 1.5 G solar spectrum (data obtained from The American Society for Testing and Materials G-173 spectrum).

As mentioned above, the minimum energy requirement for PEC water splitting technology is approximately 1.6 eV after considering overpotentials. Also, the solar irradiance is strongest in visible light (3.1 eV to 1.65 eV), so that the bandgap of a semiconductor should be less than around 3 eV in order to obtain high STH conversion efficiency. Therefore, the bandgap energy from 1.6 eV to 3 eV is a favourable range in the process of PEC water splitting, which could balance both absorption and photovoltage.

When single semiconductor fails to achieve both satisfying photocurrent and photovoltage for PEC water splitting, heterostructure integrating two or even more semiconductors is a desirable strategy.[36-38] The combination of two dissimilar materials can lead to the formation of an interface. This interface is referred to as heterojunction (e.g., p-n junction). The relative alignment of the energy bands at the heterostructure is described by band offset. The types of heterojunction linked to different band offsets can be divided into three categories, as illustrated in Figure 1-7a.[19,39] Type I is a straddling gap, where both the conduction band (CB) and valence band (VB) of wider band gap semiconductor straddle that of narrower band gap semiconductor. In type II (staggered gap), both CB and VB of first semiconductor are more negative than that of the second semiconductor respectively, but the VB of

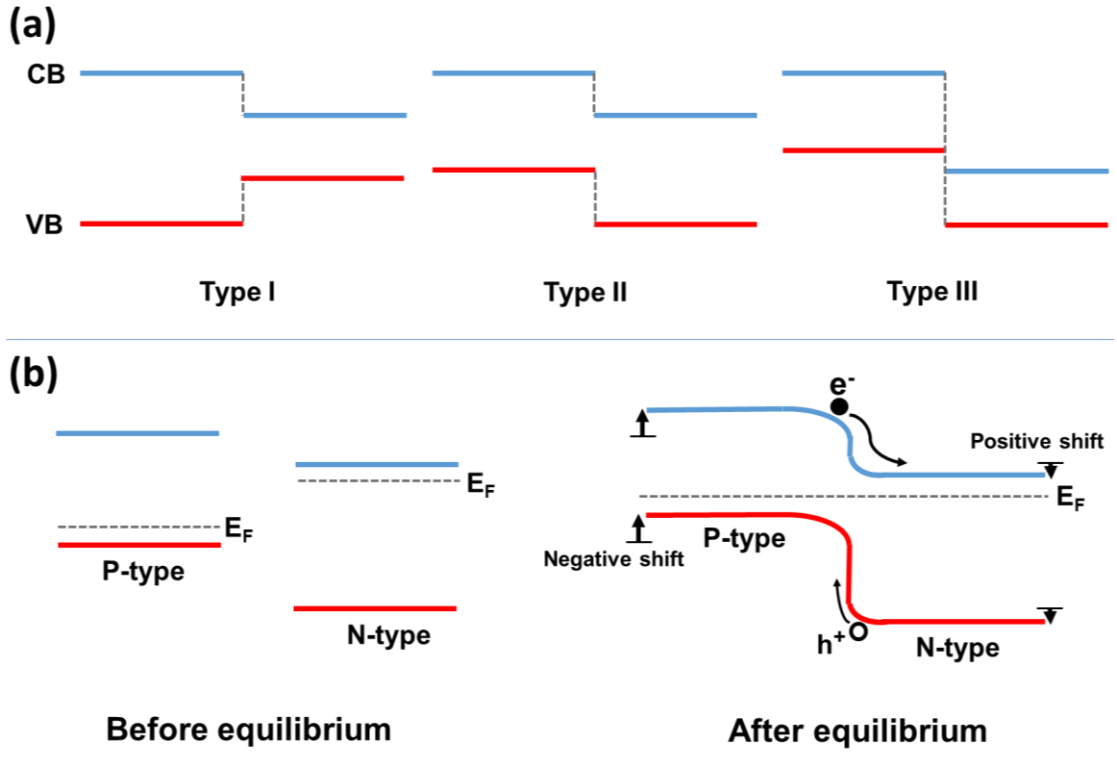

Figure 1-7 Schematic of three types of heterojunctions (a) and band diagram of p-n heterojunction before and after equilibrium (b).

the first one is still more positive than CB of the second one. Once VB of one semiconductor overlapped with CB of the other one leads to broken gap (type III), and there is no forbidden energy between the interface of two semiconductors. In general, the staggered gap is a common band offset employed in the field of PEC water splitting because it can enhance charge carrier separation and transfer assisted by built-in electric field at semiconduction heterojunction. Those heterostructures deal with many challenges in PEC water splitting technology in the following section also refer to the band alignment of type II.

The in-depth discussion of heterostructures associated with band offset needs to take band bending at interfaces into account. Taking p-n heterojunction as an example, before the equilibrium of Fermi level (E_F), the band offset is type II as shown in Figure 1-7a. When two semiconductors are in contact, there is an equilibrium of Fermi level between them, resulting in the shift of band position. As illustrated in Figure 1-7b, the band energy of p-type semiconductor moves towards negative direction in comparison with before the Fermi level equilibrium, whereas n-type semiconductor shifts towards positive direction. Therefore, a downwards band bending can be seen in the photocathode side, and photoanode side shows an opposite band bending. There is a formation of a build-in electric field in the band bending region. This internal field accelerates the transfer of photogenerated electrons (e^-) from p-type semiconductor to n-type semiconductor through conduction band, as shown in Figure 1-7b. Meanwhile, photoproduced holes (h^+) efficiently move from the n-type semiconductor to p-type semiconductor via the valence band, reducing the recombination of charge carrier. The p-n heterojunction diagram shown in Figure 1-7b does not consider the accurate band offsets, because band offset is determined by the properties of the interface, such as the built-in potential and the discontinuities of band position.[40] It should be noted that type II band alignment is not limited to a p-n junction. N-n junction and p-p junction also

belong to type II, as long as the band positions are aligned like a staggered gap. The isotype junction, however, tends to create some potential barriers that could trap electrons and/or holes, due to the different band bending from p-n junction. It is possible to overcome such barriers through external bias.[41]

1.2.5 Solar energy conversion efficiency

Efficiency is one of the most important criteria to evaluate the behaviour of PEC water splitting devices. In general, there are four different descriptions of efficiency, including solar-to-hydrogen (STH) conversion efficiency, applied bias photon-to-current conversion efficiency (ABPE), incident photon-to-current conversion efficiency (IPCE = external quantum efficiency, EQE) and also absorbed photon-to-current conversion efficiency (APCE = internal quantum efficiency, IQE).[42,43]

STH conversion efficiency is the only expression that can be directly used to compare with other technologies. It has strict measurement conditions to acquire an accurate result. Specifically, STH is measured in a short-circuited system (no external voltage applied), employing two electrodes, working electrode and counter electrode under the illumination of AM 1.5 G solar.[44] Besides, two electrodes should be in the same pH electrolytes in the absence of electrons and holes scavengers.[43] The calculation expression follows:

$$STH = \left[\frac{|J_{sc}| \times 1.23\ (V) \times \eta_F}{P_{total}}\right]_{AM\ 1.5\ G} \quad \text{Eqn. (1-1)}$$

where, P_{total} is the overall input incident light density through AM 1.5 G solar irradiation (mW cm^{-2}), J_{sc} is the photocurrent magnitude of one semiconductor in a short-circuited system (mA cm^{-2}), and η_F is the Faradaic efficiency for PEC hydrogen generation. It is worth noting that STH conversion efficiency expression takes account into various energy losses, such as the impedance of electrolyte, external wire contacts and so on, to define a benchmark efficiency.

ABPE is the STH conversion efficiency after employing an external bias. ABPE takes the applied potential into consideration; therefore, it can judge the performance of PEC water splitting more comprehensively than the STH conversion efficiency. The equation for ABPE calculation is modified upon Eqn. (1-1) as：

$$ABPE = \left[\frac{|J_{sc}|\times(1.23-|V_b|)\ (V)\times\eta_F}{P_{total}}\right]_{AM\ 1.5\ G} \quad \text{Eqn. (1-2)}$$

where, V_b is the applied potential between the working electrode and the counter electrode.

When the evaluation is narrowed to quantum scope in the process of PEC water splitting, IPCE (EQE) is an important parameter. The main difference between STH conversion efficiency and IPCE is their calculation objects. STH conversion efficiency stands in the judgment of power input/output, whereas IPCE focuses on the electrons output and photon input.[43] Unlike STH conversion efficiency measurement, IPCE can be characterised using either two or three electrodes systems (working electrode, a counter electrode and a reference electrode), and even external bias. Moreover, the IPCE measurement is performed under the illumination of monochromatic light at various wavelengths. Thus, if such an experiment is conducted in two electrodes system with no applied bias, the integrated IPCE value at every single wavelength of the whole solar spectrum can also be estimated as STH conversion efficiency.[43] IPCE describes the ratio between the overall number of photogenerated electrons output and the total number of photons input, following the equation:

$$IPCE = EQE = \frac{|J_{ph}|\times hc}{P_{mono}\times q\times\lambda} \quad \text{Eqn. (1-3)}$$

where, J_{ph} is the photocurrent density of photoelectrode under single-wavelength irradiation (mA cm^{-2}), h is Planck's constant, c is the speed of light, P_{mono} is the power

density of calibrated monochromatic light source (mW cm^{-2}), q is the charge of electron and λ is the wavelength of applied light (nm).

It can be seen that IPCE measurement covers the optical energy losses related to absorbers, including reflectance and transmittance that potentially reduce the efficiency values. In order to investigate the intrinsic properties of semiconductors in PEC water splitting process, APCE (IQE) is a suitable approach, directly describing the charge carrier separation and transfer efficiency inside a semiconductor and the kinetics of photoelectrode at interfaces. APCE is the ratio of photogenerated electrons rate versus absorbed-photons rate. Based on IPCE expression, APCE can be derived as follows:

$$APCE = IQE = \frac{IPCE}{A} \quad \text{Eqn. (1-4)}$$

where, A is the value of optical absorption. Although APCE calculation neglects photon losses due to reflectance and transmittance, those optical energy losses are a grand challenge in the practical applications.

1.3 Recent progress, challenges, and strategies of PEC water splitting

1.3.1 Overview of current progress and challenges

Since Fujishima and Honda reported the PEC performance of TiO_2 in 1972,[45] the prelude to direct water splitting driven by solar energy has begun. Currently, numerous researchers are devoted to the investigation of PEC water splitting technologies, indicating a worldwide interest in the field of solar fuel generation. However, as mentioned above, the PEC water splitting technology still incubates in

the laboratory instead of commercial application owing to numbers of grand challenges.

The challenges begin with the prototype design, including device scale rationalizations and production cost estimates, and then gradually narrow the scope to the discovery of novel photoelectrodes and the innovation of current materials. With regard to the initial challenge, prototype design requires a large number of complex industrial assessments. On the other hand, time also holds the key to this challenge. Based on the experience of commercial progress in PV devices, Spitler et al. elaborated that the commercial PEC hydrogen production is likely to start from small producers and then progressively attract large corporations that have the ability to optimize production process after considering the cost competition with PV based water electrolysis.[8] This means the challenge in prototype design could be solved over time.

When it comes to material design, the innovation of current absorbers and discovery of new materials for photoelectrodes are thornier than the former. Although various photoelectrode materials have been discovered over the past few decades, a viable and scalable material that can be applied in PEC water splitting cells has not been found up to now. Therefore, the innovation and discovery of photoelectrodes is the main area of research in the development of PEC water splitting technologies. The following content will also focus on the material design in this thesis.

1.3.2 The selectivity challenges in photoelectrodes

It is well-known that the materials employed in the field of PEC water splitting can be classified into photocathodes and photoanodes. The fundamental requirements for materials have also been mentioned in previous sections, for example, the semiconductor bandgap ranging from 1.6 eV to 3 eV is desirable for PEC water

splitting. This section will introduce some specific selectivity challenges in photocathodes and photoanodes.

Photocathodes used for PEC water splitting need to have the sufficient ability to convert photons to electrons for hydrogen evolution reaction. In order to achieve the reduction reaction of H^+ or H_2O species, the energy of the conduction band edge of the photocathode should be more negative than the hydrogen redox energy (0 V vs RHE). Similarly, the water oxidation reaction can occur only when the energy of valence band of photoanode is more positive than the H_2O/OH^- oxidation energy (+1.23 V vs RHE). Thus, although photocathodes (photoanodes) are made of p-type (n-type) semiconductors, not all p-type (n-type) semiconductors can be employed for PEC water splitting. However, in a PEC water splitting cell, the water redox reaction is not the only possible reaction. For example, the PEC oxygen reduction reaction may take place at the photocathode in oxygen-saturated solutions, since oxygen is a strong electron scavenger. As for photoanodes, it is much easier to oxidize hole scavengers (e.g., sulfite) than H_2O or OH^-.

The stability of photoelectrodes is another significant factor that should be considered when selecting photoelectrode materials. As the reduction reactions occur at the photocathode, the cathodic current is likely to protect the surface of photocathode from oxidation to some extent; in contrast, photocathodes are in oxidizing conditions, increasing the possibility of instability.[4] Therefore, photoanode materials show greater challenges than photocathode materials in terms of stability. However, it should be noted that this statement is just from a theoretical point of view. The following sections will discuss the stability of photoelectrodes in detail, based on reported experimental results.

The rest challenges in photoelectrode materials including cost, energy conversion efficiency and photovoltage are difficult to be introduced based on the classification of semiconductor type (photocathode and photoanode). Thus, according to the

literature, both photocathodes and photoanodes can be classified into two groups, PV-grade materials (silicon, II-VI group semiconductors, III-V group semiconductors, and I-III-VI_2 group semiconductors) and non-PV-grade materials (metal oxides, metal nitrides (oxynitrides/oxysulfide)).[46,47] Figure 1-8 illustrates their major challenges and corresponding strategies in the application of PEC water splitting. It can be seen that each group has its unique properties in the process of water photoelectrolysis. So, properly understanding their challenges and advantages not only lays a solid foundation for the innovation of current materials, but also clarifies the direction of novel material exploration.

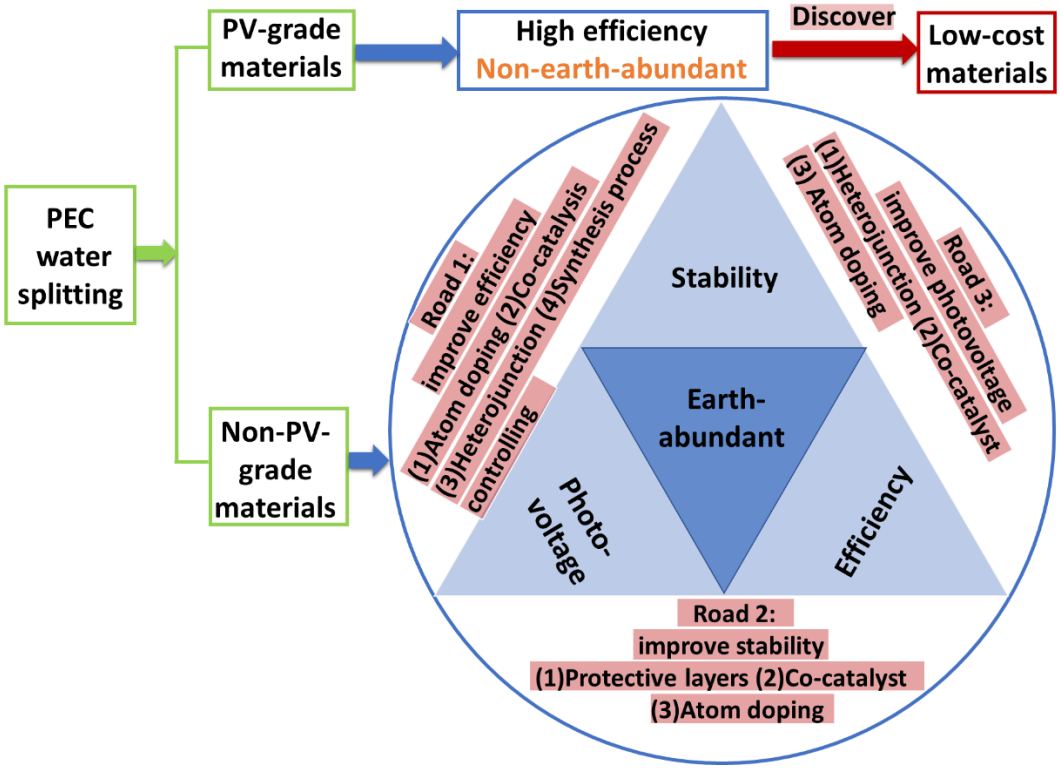

Figure 1-8 Schematic diagram of recent challenges and strategies for PEC water splitting.

1.3.3 PV-grade materials

Silicon, II-VI, III-V, and I-III-VI_2 group semiconductors are attractive materials for solar cell and a part of them are used to build water electrolysis powered by PV devices (shown in Figure 1-1c), so they are also termed PV-grade materials.[12,46,48] The

PV-grade materials have made great progress in PEC water splitting devices, for instance, the solar to hydrogen (STH) conversion efficiency is enhanced from 10% in 1998 to 19.3% in 2018, and the STH efficiency of certain materials can surprisingly reach theoretical maximum efficiency.[49] This grand performance tends to make the direct PEC water splitting configurations rival against PV connected to electrolyzer system. Such promising energy conversion efficiency in PV-grade materials is attributed to their superior charge transport properties in the bulk. However, most PV-grade materials that can be employed in PEC water splitting devices contain non-earth-abundant elements (e.g., indium), which not only increases the production cost, but also against the sustainable development for our planet. Therefore, discovering cost-efficient materials is the major challenges for PV-grade materials to achieve scalable PEC hydrogen generation.

It should be noted that although some PV-grade materials have achieved promising PEC behaviour, the relatively low photovoltage and poor stability are still challenging the study of most PV-grade photoelectrodes. For example, the largest onset potential for p-Si / electrolyte has been reported so far is +0.72 V vs RHE.[50] In addition, most of II-VI group photoanodes (e.g., CdS, CdSe and ZnSe) are only stable in the presence of hole scavengers in the aqueous solutions, although the CdTe photoanode as a special case shows a stability of 1000 hours for the oxygen evolution reaction.[51] The photovoltage loss in PV-grade materials is ascribed to the negative valence band position and the multiple interfaces the charge carriers need to cross in comparison with non-PV-grade materials, and their photocorrosion and photooxidation are responsible for instability in electrolytes.[52-54] However, it has been reported that GaInP based top cell (n-p) and GaInAs based bottom cell (n-i-p) coupled with two-junction tandem absorber can enable the onset potentials for HER to shift towards positive direction by as much as +1.9 V vs RHE.[55] In addition, stabilization of semiconductor surfaces via ultrathin TiO_2 film deposited by atomic

layer deposition has generated a strong impact in the family of PV-grade materials.[56] This approach has been able to expand the stability of photoanodes by hundreds of hours under continuous illumination.[57] However, it could be reasonable that the lifetime of PEC water splitting devices should be extended to more than tens of thousands of hours (e.g., 10 years) to achieve commercial applications,[8,14] although it is difficult to do such long stability test at laboratory scales.

In brief, integrated III-V tandem absorbers have pushed STH conversion efficiency to values above 19.3%, re-injecting new momentum to the field of PEC water splitting. Although a vast family of PV-grade compounds still show different drawbacks, such as poor stability and photovoltage in PEC water splitting process, certain strategies mentioned above have been developed to innovate them, achieving attractive results. However, it is crucial to replicate the performance of PV-grade materials with low cost and scalable processing methods at present.

1.3.4 Non-PV-grade materials

The investigation of metal oxides has attracted widespread attention in the field of PEC water splitting, since most of non-PV-grade materials are earth-abundant and can be processed on a large scale.[47,58] According to the composition of metal oxides, they can be classified into binary oxides, ternary oxides and complex oxides. Binary oxides, such as anatase TiO_2[59], Cu_2O[60], and α-Fe_2O_3[61] are the benchmark of oxide-based photoelectrodes. However, they remain significantly below the target required for viable PEC water splitting devices. To be specific, the relatively large band-gap energy of anatase TiO_2 (3.2 eV) limits the maximum STH efficiency from a theoretical perspective,[59] although it shows attractive stability and photovoltage. Cu_2O and Fe_2O_3 have a much narrower band gap of around 2.1 eV; however, cuprous oxide suffers from significant photo corrosion and the presence of surface state results in the photovoltage loss in hematite for water oxidation reaction.[62,63] Various strategies have been developed to innovate those binary oxides at present, while the

ternary oxides are relatively overlooked in the field of PEC water splitting. The composition of ternary oxides is two metal ions combined in an oxide matrix. Therefore, the electronic and composition structure of ternary oxides have more possibilities to be tuned, which plays an important role in the enhancement of PEC performance.

Table 1-1 summarises the PEC behaviour of some attractive ternary oxides from the aspects of IPCE, photovoltage and stability. The IPCE values that are not mentioned in the table notes are extracted at the potential of +1.23 V vs RHE. These three factors hold the key to the viable metal oxides-based PEC water splitting technology, as shown in the triangle in Figure 1-8. In Table 1-1, the $BiVO_4$ photoanode shows a relatively promising onset potential and IPCE for oxygen evolution reaction. However, the PEC performance of the rest ternary oxides, especially for energy conversion efficiency, is worse than the binary oxides (e.g., Cu_2O and Fe_2O_3). Generally, this is due to the lattice mismatches, grain boundaries, poor charge carrier separation and transfer, etc., leading to serious electron-hole recombination in binary oxides.[64,65] Yet, our current knowledge on their structure-performance relationships remains very limited.

On the other hand, it is worth noticing that a large percentage of ternary oxides are chemically stable in the PEC water splitting process to some extent, except for $CuBi_2O_4$ and $Ca_2Fe_2O_5$ in Table 1-1. In addition, most of the ternary oxides can not only keep those advantages from binary oxides, but also overcome certain shortcomings. For example, ferrite-based absorbers, such as $LaFeO_3$, $BiFeO_3$ and $ZnFe_2O_4$ are cost-effective, stable, sensitive in visible region and so on, similar with hematite, but their photovoltages obtain improvements.[61,79,80] The specific properties of ferrite-based ternary oxides will be mentioned and discussed in the later chapters.

Table 1-1 PEC performance of some attractive ternary oxides

Photoelectrode	Type	Onset potential vs RHE	IPCE at 400 nm	Stability	Electrolyte pH	Notes and Reference
$CuBi_2O_4$	p	+1 V	2%	Poor	6.65	IPCE at +0.6 V [66]
$CuFeO_2$	p	+0.9 V	10%	Good	13	IPCE at +0.4 V for O_2 reduction [67]
$CuCrO_2$	p	+1.06 V	Below 0.1%	Good	1	[68]
$LaFeO_3$	p	+1.2 V	0.35%	Good	12	IPCE at +0.3 V [69]
$YFeO_3$	p	+1.05 V	Below 0.01%	Good	13	[70]
$CaFe_2O_4$	p	+0.1 V	3%	Good	13	IPCE at +0.1 V [71]
$Ca_2Fe_2O_5$	p	+1.22 V	3%	Poor	11	IPCE at +0.65 V for O_2 reduction [72]
$BiVO_4$	n	+0.47 V	10%	Good	7.3	[73]
Bi_2WO_6	n	+0.9 V	2%	Good	7.3	IPCE at +1.4 V [74]
$CuFe_2O_4$	n	+0.8 V	4%	Good	14	$NiFeO_x$ as cocatalyst [75]
$BiFeO_3$	n	+0.6 V	22%	Good	11	In the presence of hole scavengers [76]
$ZnFe_2O_4$	n	+0.9 V	2%	Good	13	[77]
$MgFe_2O_4$	n	+0.64 V	3.5%	Good	14	$NiFeO_x$ as cocatalyst [75]
$FeVO_4$	n	+0.68 V	1%	Good	7	IPCE at +1.6 V [78]

All in all, the efficiency, stability and photovoltage are challenging researchers who are devoted to investigating non-PV-grade photoelectrodes. Unfortunately, no one metal oxide can naturally fulfil three corners in the triangle in Figure 1-8 up to now, so that the ultimate goal of oxide-based PEC water splitting devices is the integration of high efficiency, long-term durability and favorable photovoltage in one photoelectrode. In this thesis, the research of ferrite-based ternary oxides for PEC water splitting is targeted. Thus, the following strategies are also focused on

non-PV-grade photoelectrodes, although certain approaches are universal for both PV-grade and non-PV-grade materials.

Three ‘‘corners’’ derive three main directions (road 1 to 3 in Figure 1-8) for the innovation of photoelectrodes. It should be noted that one strategy (e.g., atom doping) may have effects on more than one ‘‘corner’’. Besides, probing novel materials can expand the material space, significantly prospering the development of PEC water splitting field, and even directly solve all issues in these three corners, though the discovery of new materials for photoelectrodes is one of the most challenging studies in the field of PEC solar fuels generation. Thus, discovering novel semiconductors should be the fourth road. Here some typical strategies for each direction (road 1 to 3) are described:

1.3.5 Strategies for improving efficiency

Atom doping is an effective approach to change the electronic structure and composition of photoelectrodes, which plays an important role in the improvement of PEC performance. For example, various dopants can not only optimize charge carrier densities and mobilities, but also narrow the band-gap energy of absorbers.[81-83] TiO_2 as the first discovered photoelectrodes has a fairly large band gap of around 3.2 eV, limiting the STH value (maximum 1%) from theoretical perspective. But the IPCE of TiO_2 obtains a dramatical increase to 18% at a wavelength close to 375 nm and potential bias of +0.6 V vs RHE upon the doping of Fe^{3+}, which is not only attributed to the increase of carrier density, but also the promotion of visible light absorption assisted by the presence of new defect states near the conduction band.[84]

In addition, because a semiconductor normally acts as a light absorber instead of active sites, the surface charge-transfer kinetics of photoreduction or photooxidation of water are very slow at most semiconductors.[85,86] Introducing a co-catalyst can

increase the number of reactive sites at the photoelectrodes surface, thereby accelerating charge transfer at the material/water interface, which is another prevalent approach to improve energy conversion efficiency.

The third strategy for enhancing energy conversion efficacy is to construct heterojunction. The investigation of heterojunction has made breakthroughs in many fields. The Nobel Prize in physics was awarded jointly to three scientists, Herbert Kroemer, Santa Barbara, and Zhores I. Alferov in 2000, in order to reward their enormous contributions in the development of semiconductor heterostructures used in optical physics. The heterojunction also has a grand effect on PEC water splitting technology. As introduced in section 1.2.4, it can enhance the charge carrier separation and transfer assisted by the built-in electric field that is generated by the equilibrium of Fermi energy at interfaces in PEC water splitting process.[87]

Finally, although controlling synthesis processes is a relatively complex method, it may achieve attractive results in the improvement of energy conversion efficiency. It can be conducted from various aspects. For example, the simplest one is to control synthesis conditions, such as temperature, gas atmosphere, and so forth.[88,89] Furthermore, the adjustment of morphologies, including orientations, film thickness and nano-structuring contribute to efficient solar oxygen and hydrogen generation.[90,91]

1.3.6 Strategies for improving stability

The deposition of protective layers is one of the fundamental approaches to stable photoelectrodes in PEC water splitting process. The compact protective layers with suitable thickness coated onto the surface of semiconductors have the ability to prevent the main absorbers to suffer from photooxidation and photocorrosion, prolonging their service life.[55,57,92,93] Currently, the protective layers include and are

not limited to TiO_2, Al_2O_3 and SnO_2.[94] Since Moehl and co-workers reported the principles of TiO_2 protective layers using atomic layer deposited (ALD) technology,[95] ALD-TiO_2 has been a mature method to protect various semiconductors (e.g., $Cu(In,Ga)(S,Se)_2$ photocathode[96]) after several years of development. It is worth mentioning that except for improving chemical stability, ALD-TiO_2 deposited onto photocathodes has multiple significant PEC effects, such as enhancing energy conversion efficiency, and even achieving favorable photovoltage, owing to the formation of heterojunction.[87,97] In addition, combining co-catalyst (e.g., Pt) with ALD-TiO_2 could further strengthen protective effects. For example, many researchers have reported that a sandwiched assembly (TiO_2/Pt/TiO_2) exhibits a better chemical stability than bare TiO_2 film.[98,99]

Atom doping can also enable photoelectrodes to remain active for long term applications, although it is less widely used than the former. The principle of this approach is totally different from the previous one. For example, $CuBi_2O_4$ as a photocathode has attracted much attention, but it suffers from serious photocorrosion.[66] The Choi group reported that the stability of $CuBi_2O_4$ for oxygen photoreduction obtains enhancement upon the doping of Ag^+, because the introduction of Ag^+ into $CuBi_2O_4$ photocathode optimizes the charge transfer of photogenerated holes, inhibiting anodic photocorrosion.[83]

1.3.7 Strategies for optimizing photovoltage

Surface states linked to Fermi level pinning are one of the most major reasons that cause the photovoltage loss in many semiconductors. The surface states located within the bandgap are mainly discussed in the field of PEC water splitting. The different electronic nature of the surface from the bulk material leads to the formation of surface states. It is well-known that Fermi level pinning refers to a case where the semiconductor band bending at semiconductor-metal junction is independent of the work function of metal. The Fermi level pinning effect can also

be seen at semiconductor-liquid junction in the presence of surface states, resulting in a constant band bending due to the charging or discharging of these surface states. Fermi level pinning leads to the narrower splitting of quasi Fermi level of electrons and holes, thereby decreasing the photovoltage, which can be confirmed by an output photovoltage that is independent of the electrolyte potential.[100] Therefore, modifying the heterostructure is an effective strategy to achieve favorable photovoltage (cathodic shift for photoanodes and anodic shift for photocathodes). The surface state can be passivated by the deposition of another material on the surface of the main absorber. Hematite is a well-known example of surface-state-induced photovoltage loss. After the deposition of Ga_2O_3 thin film, the onset potential of Fe_2O_3 changes from +1.2 V (vs RHE) to +0.8 V (vs RHE) owing to the passivation of surface state.[101] But the heterostructure is not the only approach to remove surface states. Controlling synthesis conditions also has the similar effects, for instance, the onset potential of ALD-Fe_2O_3 calcined at 800 ^oC presents a negative shift of 300 mV in comparison with the sample calcined at 500 ^oC.[102] It is noted that the heterojunction for improving photovoltage is not limited in those materials equipped with surface state. In general, modifying the interface of materials can also help a large number of absorbers without surface states to obtain favorable photovoltage via various effects (e.g., band bending), but this requires a much higher quality band-energy match. For example, the insertion of CdS layer between Sb_2Se_3 and TiO_2 enables the onset potential of Sb_2Se_3 photocathode to positively shift by 0.24 V, since the CdS layer mediates the relatively large valence band energy difference between Sb_2Se_3 and TiO_2.[103]

Furthermore, various co-catalysts (e.g., Pt, MoS_2 and IrO_2)[104] show a much lower overpotential than photoelectrodes for hydrogen evolution reaction and oxygen evolution reaction. Therefore, loading such co-catalysts at photoelectrodes surface tends to boost the photovoltage.[105] Last but not least, appropriate atom doping also

has the ability to shift the flat band potential of semiconductors towards beneficial directions (negative shift for n-type semiconductor and positive shift for p-type semiconductor), which potentially enables the onset potential to move towards favorable directions.[106]

1.4 Thesis Outline

Prototype design and material performance are two grand challenges, limiting the scalable and viable application of PEC water splitting devices. The former tends to be solved over time, while various factors, such as photovoltage, energy conversion efficiency and stability enable the latter to be problematic. This thesis will encompass the innovation and discovery of photoelectrode materials in the field of PEC water splitting. After multiple comparison, the investigation of ferrite-based ternary oxides for PEC water splitting is targeted, due to their promising stability, band-gap energies in visible region and low cost.

Chapter 2 introduces some key principles and definitions in the process of PEC water splitting and the experimental set-ups, especially for PEC characterisation employed in this thesis.

Chapter 3 and 4 focus on the enhancement of photoelectrochemical properties at $LaFeO_3$ photocathode. In Chapter 3, $LaFeO_3$ films are modified by Pt nanoparticles as co-catalysts and a TiO_2 layer as heterostructure and hole blocking layer, which results in the onset potentials over +1.4 V vs. RHE and 10-fold increase in the photocurrent responses for the hydrogen evolution reaction. Chapter 4 discusses the investigation of how the substitution of divalent alkaline-earth metal cations, including Mg^{2+}, Ca^{2+}, Sr^{2+} and Ba^{2+} into $LaFeO_3$ thin films leads to changes in the electronic structure close to the valence band edge with a strong impact in PEC

performance, achieving more than 3 times increase in the external quantum efficiency for solar oxygen reduction.

Chapter 5 shows a novel photoanode, $GaFeO_3$, which has no background in photoelectrochemical water splitting. It is the first time to systemically report its structural, optical and photoelectrochemical properties.

Chapter 6 is an overall conclusion for previous chapters and suggests the future work.

1.5 References

(1) World Energy Resources 2016. World Energy Council 2016, 6–46. Retrieved March 15, 2020, from https://www.worldenergy.org/assets/images/imported/2016/10/ World-Energy- Resources-Full-report-2016.10.03.pdf

(2) May, M. M.; Lewerenz, H. J.; Lackner, D.; Dimroth, F.; Hannappel, T. Efficient Direct Solar-to-Hydrogen Conversion by in Situ Interface Transformation of a Tandem Structure. *Nat. Commun.* **2015**, *6*, 4–10.

(3) The world's energy system must be transformed completely. The Economist. 2020. Retrieved March 15, 2020, from https://www.economist.com/schools-brief/2020/05/23/the-worlds-energy-system-must-be-transformed-completely

(4) Walter, M. G.; Warren, E. L.; McKone, J. R.; Boettcher, S. W.; Mi, Q.; Santori, E. A.; Lewis, N. S. Solar Water Splitting Cells. *Chem. Rev.* **2010**, *110*, 6446–6473.

(5) This incredible fact should get you psyched about solar power. Published by Rebecca Harrington,Sep 29, 2015. Retrieved March 21, 2020, from www.businessinsider.com /this -is-the-potential-of-solar-power-2015-9%3famp

(6) Battaglia, C.; Cuevas, A.; De Wolf, S. High-Efficiency Crystalline Silicon Solar Cells: Status and Perspectives. *Energy Environ. Sci.* **2016**, *9*, 1552–1576.

(7) Solar cell production: worldwide 2005-2019 Published by Ian Tiseo, Feb 20, 2020. Retrieved March 21, 2020, from https://www.statista.com/statistics/278917/global-solar-cell-production/

(8) Spitler, M. T.; Modestino, M. A.; Deutsch, T. G.; Xiang, C. X.; Durrant, J. R.; Esposito, D. V.; Haussener, S.; Maldonado, S.; Sharp, I. D.; Parkinson, B. A.; Ginley, D. S.; Houle, F. A.; Hannappel, T.; Neale, N. R.; Nocera, D. G.; McIntyre, P. C. Practical Challenges in

the Development of Photoelectrochemical Solar Fuels Production. *Sustain. Energy Fuels* **2020**, *4*, 985–995.

(9) Yang, W.; Prabhakar, R. R.; Tan, J.; Tilley, S. D.; Moon, J. Strategies for Enhancing the Photocurrent, Photovoltage, and Stability of Photoelectrodes for Photoelectrochemical Water Splitting. *Chem. Soc. Rev.* **2019**, *48*, 4979–5015.

(10) Cook, T. R.; Dogutan, D. K.; Reece, S. Y.; Surendranath, Y.; Teets, T. S.; Nocera, D. G. Solar Energy Supply and Storage for the Legacy and Nonlegacy Worlds. *Chem. Rev.* **2010**, *110*, 6474–6502.

(11) Staffell, I.; Scamman, D.; Velazquez Abad, A.; Balcombe, P.; Dodds, P. E.; Ekins, P.; Shah, N.; Ward, K. R. The Role of Hydrogen and Fuel Cells in the Global Energy System. *Energy Environ. Sci.* **2019**, *12*, 463–491.

(12) Jacobsson, T. J.; Fjällström, V.; Edoff, M.; Edvinsson, T. Sustainable Solar Hydrogen Production: From Photoelectrochemical Cells to PV-Electrolyzers and Back Again. *Energy Environ. Sci.* **2014**, *7*, 2056–2070.

(13) Tembhurne, S.; Nandjou, F.; Haussener, S. A Thermally Synergistic Photo-Electrochemical Hydrogen Generator Operating under Concentrated Solar Irradiation. *Nat. Energy* **2019**, *4*, 399–407.

(14) Shaner, M. R.; Atwater, H. A.; Lewis, N. S.; McFarland, E. W. A Comparative Technoeconomic Analysis of Renewable Hydrogen Production Using Solar Energy. *Energy Environ. Sci.* **2016**, *9*, 2354–2371.

(15) Kim, J. H.; Hansora, D.; Sharma, P.; Jang, J.; Lee, J. S. Toward Practical Solar Hydrogen Production – An Artificial Photosynthetic Leaf-to-farm Challenge. *Chem. Soc. Rev.* ***2019,*** 48, 1908-1971.

(16) Pinaud, B. A.; Benck, J. D.; Seitz, L. C.; Forman, A. J.; Chen, Z.; Deutsch, T. G.; James, B. D.; Baum, K. N.; Baum, G. N.; Ardo, S.; Wang, H.; Miller, E.; Jaramillo, T. F. Technical and Economic Feasibility of Centralized Facilities for Solar Hydrogen Production via Photocatalysis and Photoelectrochemistry. *Energy Environ. Sci.* **2013**, *6*, 1983–2002.

(17) Chen, S.; Takata, T.; Domen, K. Particulate Photocatalysts for Overall Water Splitting. *Nat. Rev. Mater.* **2017**, *2*, 1–17.

(18) Hisatomi, T.; Kubota, J.; Domen, K. Recent Advances in Semiconductors for Photocatalytic and Photoelectrochemical Water Splitting. *Chem. Soc. Rev.* **2014**, *43*, 7520–7535.

(19) Jiang, C.; Moniz, S. J. A.; Wang, A.; Zhang, T.; Tang, J. Photoelectrochemical Devices for Solar Water Splitting-Materials and Challenges. *Chem. Soc. Rev.* **2017**, *46*, 4645–4660.

(20) SATO, N. Electrocthemistry of Semiconductors. *Tetsu-to-Hagane* **1990**, *76*,

1423–1436.

(21) Zhang, Z.; Yates, J. T. Band Bending in Semiconductors: Chemical and Physical Consequences at Surfaces and Interfaces. *Chem. Rev.* **2012**, *112*, 5520–5551.

(22) Zhang, K.; Ma, M.; Li, P.; Wang, D. H.; Park, J. H. Water Splitting Progress in Tandem Devices: Moving Photolysis beyond Electrolysis. *Adv. Energy Mater.* **2016**, *6*, 1–16.

(23) Young, J. L.; Steiner, M. A.; Döscher, H.; France, R. M.; Turner, J. A.; Deutsch, T. G. Direct Solar-to-Hydrogen Conversion via Inverted Metamorphic Multi-Junction Semiconductor Architectures. *Nat. Energy* **2017**, *2*, 17028.

(24) Kang, D.; Young, J. L.; Lim, H.; Klein, W. E.; Chen, H.; Xi, Y.; Gai, B.; Deutsch, T. G.; Yoon, J. Printed Assemblies of GaAs Photoelectrodes with Decoupled Optical and Reactive Interfaces for Unassisted Solar Water Splitting. *Nat. Energy* **2017**, *2*, 17043.

(25) Haussener, S.; Xiang, C.; Spurgeon, J. M.; Ardo, S.; Lewis, N. S.; Weber, A. Z. Modeling, Simulation, and Design Criteria for Photoelectrochemical Water-Splitting Systems. *Energy Environ. Sci.* **2012**, *5*, 9922–9935.

(26) Rongé, J.; Bosserez, T.; Martel, D.; Nervi, C.; Boarino, L.; Taulelle, F.; Decher, G.; Bordiga, S.; Martens, J. A. Monolithic Cells for Solar Fuels. *Chem. Soc. Rev.* **2014**, *43*, 7963–7981.

(27) Fountaine, K. T.; Lewerenz, H. J.; Atwater, H. A. Efficiency Limits for Photoelectrochemical Water-Splitting. *Nat. Commun.* **2016**, *7*, 13706-1–9.

(28) Walter, M. G.; Warren, E. L.; McKone, J. R.; Boettcher, S. W.; Mi, Q.; Santori, E. A.; Lewis, N. S. Solar Water Splitting Cells. *Chem. Rev.* **2010**, *110*, 6446–6473.

(29) Nurlaela, E.; Sasaki, Y.; Nakabayashi, M.; Shibata, N.; Yamada, T.; Domen, K. Towards Zero Bias Photoelectrochemical Water Splitting: Onset Potential Improvement on a Mg:GaN Modified-Ta_3N_5 Photoanode. *J. Mater. Chem. A* **2018**, *6*, 15265–15273.

(30) Peng, G.; Albero, J.; Garcia, H.; Shalom, M. A Water-Splitting Carbon Nitride Photoelectrochemical Cell with Efficient Charge Separation and Remarkably Low Onset Potential. *Angew. Chemie - Int. Ed.* **2018**, *57*, 15807–15811.

(31) Chu, S.; Li, W.; Yan, Y.; Hamann, T.; Shih, I.; Wang, D.; Mi, Z. Roadmap on Solar Water Splitting: Current Status and Future Prospects. *Nano Futur.* **2017**, *1*, 1–75.

(32) Ullah, R.; Pei, M.; Wu, J.; Tian, Y.; Gu, Z.; Zhang, Q.; Song, C.; Yang, Y.; Ahmad, M.; Zeb, J.; Qayyum, F.; Liu, Y.; An, X.; Gu, L.; Wang, X.; Zhang, J. Bifunctional Photoelectrode Driven by Charged Domain Walls in Ferroelectric Bi_2WO_6. *ACS Appl. Energy Mater.* **2020**, *3*, 4149–4154.

(33) Spitler, M. T.; Modestino, M. A.; Deutsch, T. G.; Xiang, C. X.; Durrant, J. R.; Esposito, D. V.; Haussener, S.; Maldonado, S.; Sharp, I. D.; Parkinson, B. A.; Ginley, D. S.; Houle, F.

A.; Hannappel, T.; Neale, N. R.; Nocera, D. G.; McIntyre, P. C. Practical Challenges in the Development of Photoelectrochemical Solar Fuels Production. *Sustain. Energy Fuels* **2020**, *4*, 985–995.

(34) Polman, A.; Atwater, H. A. Photonic Design Principles for Ultrahigh-Efficiency Photovoltaics. *Nat. Mater.* **2012**, *11*, 174–177.

(35) Yang, W.; Prabhakar, R. R.; Tan, J.; Tilley, S. D.; Moon, J. Strategies for Enhancing the Photocurrent, Photovoltage, and Stability of Photoelectrodes for Photoelectrochemical Water Splitting. *Chem. Soc. Rev.* **2019**, *48*, 4979–5015.

(36) Sun, X.; Tiwari, D.; Fermin, D. J. Nanostructured $LaFeO_3$ Photocathodes with Onset Potentials for the Hydrogen Evolution Reaction Over 1.4 V vs. RHE. *J. Electrochem. Soc.* **2019**, *166*, H764–H768.

(37) Choudhary, S.; Upadhyay, S.; Kumar, P.; Singh, N.; Satsangi, V. R.; Shrivastav, R.; Dass, S. Nanostructured Bilayered Thin Films in Photoelectrochemical Water Splitting - A Review. *Int. J. Hydrogen Energy* **2012**, *37*, 18713–18730.

(38) Peerakiatkhajohn, P.; Yun, J.-H.; Wang, S.; Wang, L. Review of Recent Progress in Unassisted Photoelectrochemical Water Splitting: From Material Modification to Configuration Design. *J. Photonics Energy* **2016**, *7*, 012006.

(39) Jia, C.; Lin, Z.; Huang, Y.; Duan, X. Nanowire Electronics: From Nanoscale to Macroscale. *Chem. Rev.* **2019**, *119*, 9074–9135.

(40) Robertson, J. New High-K Materials for CMOS Applications. *Compr. Semicond. Sci. Technol.* **2011**, *1–6*, 132–176.

(41) Yaw, C. S.; Ruan, Q.; Tang, J.; Soh, A. K.; Chong, M. N. A Type II N-N Staggered Orthorhombic V_2O_5/Monoclinic Clinobisvanite $BiVO_4$ Heterojunction Photoanode for Photoelectrochemical Water Oxidation: Fabrication, Characterisation and Experimental Validation. Chem. Engineering J. **2019**, *364*, 177–185.

(42) Yao, T.; An, X.; Han, H.; Chen, J. Q.; Li, C. Photoelectrocatalytic Materials for Solar Water Splitting. *Adv. Energy Mater.* **2018**, *8*, 1–36.

(43) Chen, Z.; Jaramillo, T. F.; Deutsch, T. G.; Kleiman-Shwarsctein, A.; Forman, A. J.; Gaillard, N.; Garland, R.; Takanabe, K.; Heske, C.; Sunkara, M.; McFarland, E. W.; Domen, K.; Milled, E. L.; Dinh, H. N. Accelerating Materials Development for Photoelectrochemical Hydrogen Production: Standards for Methods, Definitions, and Reporting Protocols. *J. Mater. Res.* **2010**, *25*, 3–16.

(44) Glanz, K. Using Behavioral Theories to Guide Decisions of What to Measure , and Why. *Int. J. Hydrogen Energy* **2010**, *27*, 991–1022.

(45) Fujishima, A.; Honda, K. Electrochemical Photolysis of Water at a Semiconductor Electrode. *Nature* **1972**, *238*, 38–40.

(46) Yao, T.; An, X.; Han, H.; Chen, J. Q.; Li, C. Photoelectrocatalytic Materials for Solar Water Splitting. *Adv. Energy Mater.* **2018**, *8*, 1–36.

(47) Huang, Q.; Ye, Z.; Xiao, X. Recent Progress in Photocathodes for Hydrogen Evolution. *J. Mater. Chem. A* **2015**, *3*, 15824–15837.

(48) Luo, J.; Im, J. H.; Mayer, M. T.; Schreier, M.; Nazeeruddin, M. K.; Park, N. G.; Tilley, S. D.; Fan, H. J.; Grätzel, M. Water Photolysis at 12.3% Efficiency via Perovskite Photovoltaics and Earth-Abundant Catalysts. *Science.* **2014**, *345*, 1593–1596.

(49) Cheng, W. H.; Richter, M. H.; May, M. M.; Ohlmann, J.; Lackner, D.; Dimroth, F.; Hannappel, T.; Atwater, H. A.; Lewerenz, H. J. Monolithic Photoelectrochemical Device for Direct Water Splitting with 19% Efficiency. *ACS Energy Lett.* **2018**, *3*, 1795–1800.

(50) Oh, I.; Kye, J.; Hwang, S. Enhanced Photoelectrochemical Hydrogen Production from Silicon Nanowire Array Photocathode. *Nano Lett.* **2012**, *12*, 298–302.

(51) Sun, K.; Saadi, F. H.; Lichterman, M. F.; Hale, W. G.; Wang, H. P.; Zhou, X.; Plymale, N. T.; Omelchenko, S. T.; He, J. H.; Papadantonakis, K. M.; Brunschwig, B. S.; Lewis, N. S. Stable Solar-Driven Oxidation of Water by Semiconducting Photoanodes Protected by Transparent Catalytic Nickel Oxide Films. *Proc. Natl. Acad. Sci. U. S. A.* **2015**, *112*, 3612–3617.

(52) Bard, A. J.; Bocarsly, A. B.; Fan, F. R. F.; Walton, E. G.; Wrighton, M. S. The Concept of Fermi Level Pinning at Semiconductor/Liquid Junctions. Consequences for Energy Conversion Efficiency and Selection of Useful Solution Redox Couples in Solar Devices. *J. Am. Chem. Soc.* **1980**, *102*, 3671–3677.

(53) Oh, S.; Oh, J. High Performance and Stability of Micropatterned Oxide-Passivated Photoanodes with Local Catalysts for Photoelectrochemical Water Splitting. *J. Phys. Chem. C* **2016**, *120*, 133–141.

(54) Shaner, M. R.; Hu, S.; Sun, K.; Lewis, N. S. Stabilization of Si Microwire Arrays for Solar-Driven H_2O Oxidation to O_2(g) in 1.0 M KOH(Aq) Using Conformal Coatings of Amorphous TiO_2. *Energy Environ. Sci.* **2015**, *8*, 203–207.

(55) May, M. M.; Lewerenz, H. J.; Lackner, D.; Dimroth, F.; Hannappel, T. Efficient Direct Solar-to-Hydrogen Conversion by in Situ Interface Transformation of a Tandem Structure. *Nat. Commun.* **2015**, *6*, 8286.

(56) Hu, S.; Shaner, M. R.; Beardslee, J. A.; Lichterman, M.; Brunschwig, B. S.; Lewis, N. S. ChemInform Abstract: Amorphous TiO_2 Coatings Stabilize Si, GaAs, and GaP Photoanodes for Efficient Water Oxidation. *Science* **2014**, *45*, 1005.

(57) Verlage, E.; Hu, S.; Liu, R.; Jones, R. J. R.; Sun, K.; Xiang, C.; Lewis, N. S.; Atwater, H. A. A Monolithically Integrated, Intrinsically Safe, 10% Efficient, Solar-Driven

Water-Splitting System Based on Active, Stable Earth-Abundant Electrocatalysts in Conjunction with Tandem III-V Light Absorbers Protected by Amorphous TiO_2 Films. *Energy Environ. Sci.* **2015**, *8*, 3166.

(58) Lee, D. K.; Lee, D.; Lumley, M. A.; Choi, K. S. Progress on Ternary Oxide-Based Photoanodes for Use in Photoelectrochemical Cells for Solar Water Splitting. *Chem. Soc. Rev.* **2019**, *48*, 2126–2157.

(59) Yin, W.; Tang, H.; Wei. S.; Al-Jassim, M. M.; Turner, J.; Yan, Y. Band Structure Engineering of Semiconductors for Enhanced Photoelectrochemical Water Splitting: The Case of TiO_2. *Phys. Rev. B* **2010**, *82*, 045106.

(60) Luo, J.; Steier, L.; Son, M. K.; Schreier, M.; Mayer, M. T.; Grätzel, M. Cu_2O Nanowire Photocathodes for Efficient and Durable Solar Water Splitting. *Nano Lett.* **2016**, *16*, 1848.

(61) Wang, L.; Hu, H.; Nguyen, N. T.; Zhang, Y.; Schmuki, P.; Bi, Y. Plasmon-Induced Hole-Depletion Layer on Hematite Nanoflake Photoanodes for Highly Efficient Solar Water Splitting. *Nano Energy* **2017**, *35*, 171–178.

(62) Zhang, Z.; Wang, P. Highly Stable Copper Oxide Composite as an Effective Photocathode for Water Splitting via a Facile Electrochemical Synthesis Strategy. *J. Mater. Chem.* **2012**, *22*, 2456–2464.

(63) Ling, Y.; Wang, G.; Reddy, J.; Wang, C.; Zhang, J. Z.; Li, Y. The Influence of Oxygen Content on the Thermal Activation of Hematite Nanowires. *Angew. Chemie - Int. Ed.* **2012**, *51*, 4074–4079.

(64) Montoya, J. H.; Seitz, L. C.; Chakthranont, P.; Vojvodic, A.; Jaramillo, T. F.; Nørskov, J. K. Materials for Solar Fuels and Chemicals. *Nat. Mater.* **2016**, *16*, 70–81.

(65) Abdi, F. F.; Savenije, T. J.; May, M. M.; Dam, B.; Van De Krol, R. The Origin of Slow Carrier Transport in $BiVO_4$ Thin Film Photoanodes: A Time-Resolved Microwave Conductivity Study. *J. Phys. Chem. Lett.* **2013**, *4*, 2752–2757.

(66) Berglund, S. P.; Abdi, F. F.; Bogdanoff, P.; Chemseddine, A.; Friedrich, D.; Van De Krol, R. Comprehensive Evaluation of $CuBi_2O_4$ as a Photocathode Material for Photoelectrochemical Water Splitting. *Chem. Mater.* **2016**, *28*, 4231–4242.

(67) Prévot, M. S.; Guijarro, N.; Sivula, K. Enhancing the Performance of a Robust Sol-Gel-Processed p-Type Delafossite $CuFeO_2$ Photocathode for Solar Water Reduction. *ChemSusChem* **2015**, *8*, 1359–1367.

(68) Díaz-García, A. K.; Lana-Villarreal, T.; Gómez, R. Sol-Gel Copper Chromium Delafossite Thin Films as Stable Oxide Photocathodes for Water Splitting. *J. Mater. Chem. A* **2015**, *3*, 19683–19687.

(69) Celorrio, V.; Bradley, K.; Weber, O. J.; Hall, S. R.; Fermín, D. J. Photoelectrochemical

Properties of $LaFeO_3$ Nanoparticles. *ChemElectroChem* **2014**, *1*, 1667–1671.

(70) Díez-García, M. I.; Celorrio, V.; Calvillo, L.; Tiwari, D.; Gómez, R.; Fermín, D. J. $YFeO_3$ Photocathodes for Hydrogen Evolution. *Electrochim. Acta* **2017**, *246*, 365–371.

(71) Ida, S.; Yamada, K.; Matsunaga, T.; Hagiwara, H.; Matsumoto, Y.; Ishihara, T. Preparation of P-Type $CaFe_2O_4$ Photocathodes for Producing Hydrogen from Water. *J. Am. Chem. Soc.* **2010**, *132*, 17343–17345.

(72) Wheeler, G. P.; Choi, K. S. Investigation of P-Type $Ca_2Fe_2O_5$ as a Photocathode for Use in a Water Splitting Photoelectrochemical Cell. *ACS Appl. Energy Mater.* **2018**, *1*, 4917–4923.

(73) She, H.; Yue, P.; Ma, X.; Huang, J.; Wang, L.; Wang, Q. Fabrication of $BiVO_4$ Photoanode Cocatalyzed with NiCo-Layered Double Hydroxide for Enhanced Photoactivity of Water Oxidation. *Appl. Catal. B Environ.* **2020**, *263*, 118280.

(74) Bhattacharya, C.; Lee, H. C.; Bard, A. J. Rapid Screening by Scanning Electrochemical Microscopy (SECM) of Dopants for Bi_2WO_6 Improved Photocatalytic Water Oxidation with Zn Doping. *J. Phys. Chem. C* **2013**, *117*, 9633–9640.

(75) Guijarro, N.; Bornoz, P.; Prévot, M.; Yu, X.; Zhu, X.; Johnson, M.; Jeanbourquin, X.; Le Formal, F.; Sivula, K. Evaluating Spinel Ferrites MFe_2O_4(M = Cu, Mg, Zn) as Photoanodes for Solar Water Oxidation: Prospects and Limitations. *Sustain. Energy Fuels* **2018**, *2*, 103–117.

(76) Moniz, S. J. A.; Blackman, C. S.; Southern, P.; Weaver, P. M.; Tang, J.; Carmalt, C. J. Visible-Light Driven Water Splitting over $BiFeO_3$ Photoanodes Grown via the LPCVD Reaction of $[Bi(OtBu)_3]$ and $[Fe(OtBu)_3]_2$ and Enhanced with a Surface Nickel Oxygen Evolution Catalyst. *Nanoscale* **2015**, *7*, 16343–16353.

(77) Hufnagel, A. G.; Peters, K.; Müller, A.; Scheu, C.; Fattakhova-Rohlfing, D.; Bein, T. Zinc Ferrite Photoanode Nanomorphologies with Favorable Kinetics for Water-Splitting. *Adv. Funct. Mater.* **2016**, *26*, 4435–4443.

(78) Zhang, M.; Ma, Y.; Friedrich, D.; Van De Krol, R.; Wong, L. H.; Abdi, F. F. Elucidation of the Opto-Electronic and Photoelectrochemical Properties of $FeVO_4$ Photoanodes for Solar Water Oxidation. *J. Mater. Chem. A* **2018**, *6*, 548–555.

(79) Wang, G.; Ling, Y.; Wheeler, D. A.; George, K. E. N.; Horsley, K.; Heske, C.; Zhang, J. Z.; Li, Y. Facile Synthesis of Highly Photoactive α-Fe_2O_3-Based Films for Water Oxidation. *Nano Lett.* **2011**, *11*, 3503–3509.

(80) Sivula, K.; Le Formal, F.; Grätzel, M. Solar Water Splitting: Progress Using Hematite (α-Fe_2O_3) Photoelectrodes. *ChemSusChem* **2011**, *4*, 432–449.

(81) Díez-García, M. I.; Gómez, R. Metal Doping to Enhance the Photoelectrochemical Behavior of $LaFeO_3$ Photocathodes. *ChemSusChem* **2017**, *10*, 2457–2463.

(82) Wheeler, G. P.; Baltazar, V. U.; Smart, T. J.; Radmilovic, A.; Ping, Y.; Choi, K. S. Combined Theoretical and Experimental Investigations of Atomic Doping to Enhance Photon Absorption and Carrier Transport of $LaFeO_3$ Photocathodes. *Chem. Mater.* **2019**, *31*, 5890–5899.

(83) Kang, D.; Hill, J. C.; Park, Y.; Choi, K. S. Photoelectrochemical Properties and Photostabilities of High Surface Area $CuBi_2O_4$ and Ag-Doped $CuBi_2O_4$ Photocathodes. *Chem. Mater.* **2016**, *28*, 4331–4340.

(84) Wang, C.; Chen, Z.; Jin, H.; Cao, C.; Li, J.; Mi, Z. Enhancing Visible-Light Photoelectrochemical Water Splitting through Transition-Metal Doped TiO_2 Nanorod Arrays. *J. Mater. Chem. A* **2014**, *2*, 17820–17827.

(85) Wheeler, G. P.; Choi, K. S. Photoelectrochemical Properties and Stability of Nanoporous P-Type $LaFeO_3$ Photoelectrodes Prepared by Electrodeposition. *ACS Energy Lett.* **2017**, *2*, 2378.

(86) Kim, J. H.; Kim, H. E.; Kim, J. H.; Lee, J. S. Ferrites: Emerging Light Absorbers for Solar Water Splitting. *J. Mater. Chem. A* **2020**, *8*, 9447–9482.

(87) Sun, X.; Tiwari, D.; Fermin, D. J. Nanostructured $LaFeO_3$ Photocathodes with Onset Potentials for the Hydrogen Evolution Reaction Over 1.4 V vs. RHE. *J. Electrochem. Soc.* **2019**, *166*, H764–H768.

(88) Dias, P.; Schreier, M.; Tilley, S. D.; Luo, J.; Azevedo, J.; Andrade, L.; Bi, D.; Hagfeldt, A.; Mendes, A.; Grätzel, M.; Mayer, M. T. Transparent Cuprous Oxide Photocathode Enabling a Stacked Tandem Cell for Unbiased Water Splitting. *Adv. Energy Mater.* **2015**, *5*, 1–9.

(89) Radmilovic, A.; Smart, T. J.; Ping, Y.; Choi, K. S. Combined Experimental and Theoretical Investigations of N-Type $BiFeO_3$ for Use as a Photoanode in a Photoelectrochemical Cell. *Chem. Mater.* **2020**, *32*, 3262−3270.

(90) Yang, W.; Ahn, J.; Oh, Y.; Tan, J.; Lee, H.; Park, J.; Kwon, H. C.; Kim, J.; Jo, W.; Kim, J.; Moon, J. Adjusting the Anisotropy of 1D Sb_2Se_3 Nanostructures for Highly Efficient Photoelectrochemical Water Splitting. *Adv. Energy Mater.* **2018**, *8*, 1–11.

(91) Li, D.; Liu, Y.; Shi, W.; Shao, C.; Wang, S.; Ding, C.; Liu, T.; Fan, F.; Shi, J.; Li, C. Crystallographic-Orientation-Dependent Charge Separation of $BiVO_4$ for Solar Water Oxidation. *ACS Energy Lett.* **2019**, *4*, 825–831.

(92) Fountaine, K. T.; Lewerenz, H. J.; Atwater, H. A. Efficiency Limits for Photoelectrochemical Water-Splitting. *Nat. Commun.* **2016**, *7*, 1–9.

(93) Young, J. L.; Steiner, M. A.; Döscher, H.; France, R. M.; Turner, J. A.; Deutsch, T. G. Direct Solar-to-Hydrogen Conversion via Inverted Metamorphic Multi-Junction Semiconductor Architectures. *Nat. Energy* **2017**, *2*, 17028.

(94) Yang, W.; Prabhakar, R. R.; Tan, J.; Tilley, S. D.; Moon, J. Strategies for Enhancing the Photocurrent, Photovoltage, and Stability of Photoelectrodes for Photoelectrochemical Water Splitting. *Chem. Soc. Rev.* **2019**, *48*, 4979–5015.

(95) Moehl, T.; Suh, J.; Sévery, L.; Wick-Joliat, R.; Tilley, S. D. Investigation of (Leaky) ALD TiO_2 Protection Layers for Water-Splitting Photoelectrodes. *ACS Appl. Mater. Interfaces* **2017**, *9*, 43614–43622.

(96) Baek, M.; Zafar, M.; Kim, S.; Kim, D. H.; Jeon, C. W.; Lee, J.; Yong, K. Enhancing Durability and Photoelectrochemical Performance of the Earth Abundant Ni–Mo/TiO_2/CdS/CIGS Photocathode under Various PH Conditions. *ChemSusChem* **2018**, *11*, 3679–3688.

(97) Wang, K.; Huang, D.; Yu, L.; Gu, H.; Ikeda, S.; Jiang, F. Environmentally Friendly Cu_2ZnSnS_4-Based Photocathode Modified with a ZnS Protection Layer for Efficient Solar Water Splitting. *J. Colloid Interface Sci.* **2019**, *536*, 9–16.

(98) Li, S.; Zhang, P.; Song, X.; Gao, L. Photoelectrochemical Hydrogen Production of TiO_2 Passivated Pt/Si-Nanowire Composite Photocathode. *ACS Appl. Mater. Interfaces* **2015**, *7*, 18560–18565.

(99) Yang, F.; Aguiar, J. A.; Fairchild, M.; Vakki, W.; Younan, S.; Zhou, Y.; Zhuo, L.; Gu, J. Dual Protection Layer Strategy to Increase Photoelectrode–Catalyst Interfacial Stability: A Case Study on Black Silicon Photoelectrodes. *Adv. Mater. Interfaces* **2019**, *6*, 1–8.

(100) Bard, A. J.; Bocarsly, A. B.; Fan, F. R. F.; Walton, E. G.; Wrighton, M. S. J. The Concept of Fermi Level Pinning at Semiconductor/liquid Junctions. Consequences for Energy Conversion Efficiency and Selection of Useful Solution Redox Couples in Solar Devices. *Am. Chem. Soc.* **1980**, *11*, 3671-3677.

(101) Hisatomi, T.; Le Formal, F.; Cornuz, M.; Brillet, J.; Tétreault, N.; Sivula, K.; Grätzel, M. Cathodic Shift in Onset Potential of Solar Oxygen Evolution on Hematite by 13-Group Oxide Overlayers. *Energy Environ. Sci.* **2011**, *4*, 2512–2515.

(102) Zandi, O.; Hamann, T. W. Enhanced Water Splitting Efficiency through Selective Surface State Removal. *J. Phys. Chem. Lett.* **2014**, *5*, 1522–1526.

(103) Park, J.; Yang, W.; Oh, Y.; Tan, J.; Lee, H.; Boppella, R.; Moon, J. Efficient Solar-to-Hydrogen Conversion from Neutral Electrolytes Using Morphology-Controlled Sb_2Se_3 Light Absorbers. *ACS Energy Lett.* **2019**, *4*, 517–526.

(104) Morales-Guio, C. G.; Stern, L. A.; Hu, X. Nanostructured Hydrotreating Catalysts for Electrochemical Hydrogen Evolution. *Chem. Soc. Rev.* **2014**, *43*, 6555–6569.

(105) Luo, J.; Li, Z.; Nishiwaki, S.; Schreier, M.; Mayer, M. T.; Cendula, P.; Lee, Y. H.; Fu, K.; Cao, A.; Nazeeruddin, M. K.; Romanyuk, Y. E.; Buecheler, S.; Tilley, S. D.; Wong, L. H.;

Tiwari, A. N.; Grätzel, M. Targeting Ideal Dual-Absorber Tandem Water Splitting Using Perovskite Photovoltaics and $CuIn_xGa_{1-x}Se_2$ Photocathodes. *Adv. Energy Mater.* **2015**, *5*, 1–8.

(106) Xi, L.; Bassi, P. S.; Chiam, S. Y.; Mak, W. F.; Tran, P. D.; Barber, J.; Chye Loo, J. S.; Wong, L. H. Surface Treatment of Hematite Photoanodes with Zinc Acetate for Water Oxidation. *Nanoscale* **2012**, *4*, 4430–4433.

CHAPTER 2.

Experimental set-up and methods

2.1 Abstract

Different experimental set-ups, especially for PEC characterisation, and synthesis methods employed in this thesis are illustrated in this chapter. In order to make the thesis be read clearly and easily, the detailed synthesis procedures are described in the Experimental Section of each chapter.

2.2 Experimental set-up and methods

2.2.1 XRD

The structure of as-prepared samples is determined employing powder X-ray diffraction (XRD, Bruker AXS D8 Advance) consisting of a Ni-filtered Cu-Kα source (λ = 1.54016 Å) and position-sensitive detector. Structural information such as the phase and crystallinity of samples, the size of the crystallites and lattice parameters is derived from quantitative full-profile refinement based on Pawley and Rietveld schemes.

2.2.2 SEM, EDX and TEM

Scanning electron microscopy (SEM, Jeol iT300) and with energy-dispersive X-rays analysis (EDX, Oxford Xmax-80 detector coupled to SEM) were used to analyse thin film morphology and composition, respectively. The cross-sectional SEM imaging was also used to measure the thickness of films. Nanometric structural characterization is conducted using high-resolution transmission electron microscopy (HR-TEM, JEOL JEM 2100). The samples for HR-TEM are prepared by drop-casting an ethanolic suspension of powder obtained by scraping the films and sonicating in ethanol, on to a holey-carbon grid (200 mesh).

2.2.3 XPS

The X-ray photoelectron spectroscopy (XPS) of as-received thin films was carried out at the Bristol NanoESCA Facility. All samples used in XPS characterisation were spin-coated onto F:SnO_2 (FTO) substrate to minimise sample charging. The XPS spectra aided to explore the chemical states of different elements, surface chemical composition as well as valence-bandedge electronic structure. The spectra were obtained by excitation from a non-monochromatic Al Kα line in a chamber with a base pressure of 4 x 10^{-11} mbar. The emitted photoelectrons are analysed with an ARGUS spectrometer with an overall energy resolution of 0.9 eV. The detail scans of the core levels and survey scans are recorded with pass energies 20 eV and 50 eV, respectively. The films ($GaFeO_3$ thin films) exhibit considerable charging, which was compensated using charge neutralization through electron flood-gun. Charge-correction was performed against the adventitious C 1s peak assumed at 284.8 eV. The deconvolution of the core bands is done using Gaussian-Lorentzian composite functions after Shirley background subtraction using XPSPEAK code.

2.2.4 Diffuse reflectance and transmittance spectra

For optical characterisation, the UV-visible diffuse reflectance and transmittance spectra were measured by a Shimadzu UV-2401 PC spectrophotometer fitted with an integrating sphere. Critical optical parameters such as absorption coefficient (α) and bandgaps were evaluated from the transformation of optical spectra.

2.2.5 Photoelectrochemical characterisations

The methods for PEC characterisation were employed in this thesis including the cyclic voltammetry (CV), linear sweep voltammetry (LSV), transient photocurrent (TP) and quantum efficiency (QE) measurements. In particular, photocurrent measurement is one of the most significant analysis to assess the quality of different semiconductors for PEC water splitting. The values of photocurrent density also used

for the calculation of various energy conversion efficiencies, as shown in Eqn. (1-1) to (1-4). In addition, the photocurrent responses can provide a wealth of information related to photoelectrodes, such as parameters determining dynamics of charge carrier transfer and recombination, flat band position, etc.

The Gartner equation is a quantitative model for the expression of photocurrent (J_{ph}) as a function of potential:[1]

$$J_{ph} = eI_0\left(1 - \frac{e^{-\alpha W}}{1 + \alpha L_n}\right)$$

where, e is the charge of elementary, I_0 is incident photon flux, α is absorption coefficient of the thin film, W is the length of space charge region, and L_n is the diffusion length of minority carrier. Gartner equation assumes there is no surface recombination in the space charge region. It can be seen that this quantitative model results in two crucial parameters, W and L_n, which can be used to explore the intrinsic characteristics of absorbers for PEC water splitting. The detailed analysis of photocurrent responses based on Gartner equation will be presented in the following chapters.

The composition of the basic set-up for PEC characterisations is a photoelectrochemical cell, a light source and a potentiostat. In this thesis, there are two set-ups that support different PEC experiments. To be specific, the measurements for CV, LSV and TP were performed by the equipment in Figure 2-1. The components of (1) to (7) constitutes the PEC cell, and the physical photo is displayed on the left-hand side. The three-electrode system, including working electrode (1), reference electrode (Ag/AgCl, 3 M saturated KCl) (2) and counter electrode (glassy carbon) (3) is immersed into the electrolyte (4). It should be noted that all (photo)electrochemical characterization employed glassy carbon as counter electrode instead of the platinum, because the platinum counter electrode can typically contaminate the electrolyte solutions, making characterization inaccurate.

The photoelectrode (5) was covered with tape (epoxy), which enables the exposed geometric area of the thin film around 1 cm^2 within the illumination area in the electrolyte. The photoelectrode is connected to the working electrode through a crocodile clip attached to the exposed FTO back contact. The plastic tube (6) is used as the channel of gas, such as argon and oxygen, providing an appropriate atmosphere. PEC measurements were performed after purging the electrolytes with argon or oxygen for over 30 minutes. The photoelectrochemical cell includes a glass vessel with a transparent quartz window (7) for light.

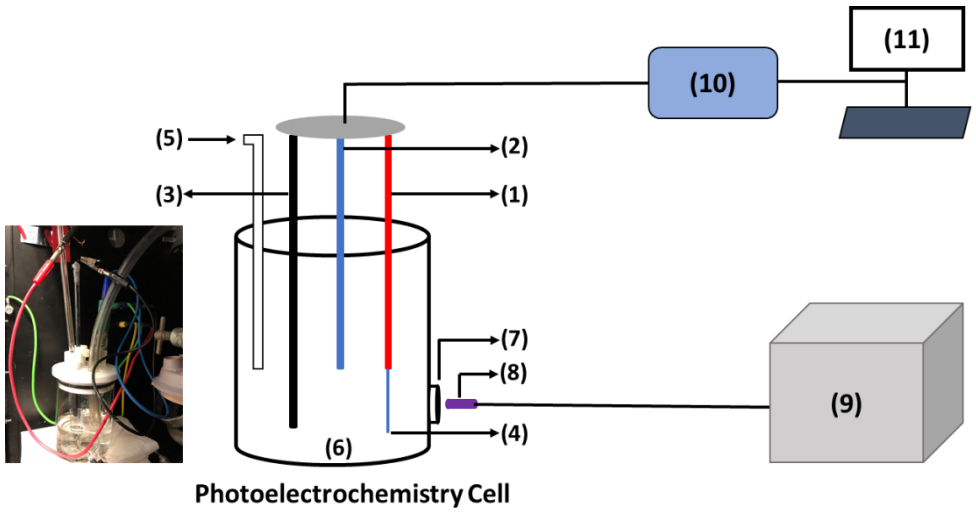

Figure 2-1 Photoelectrochemical set-up I.

The single-wavelength light source includes LEDs (Thorlabs) (8) driven by a waveform generator (Stanford Research Systems) (9) in Figure 2-1. Photon flux is referenced against a silicon photodiode (Newport corporation, NREL calibrated). The input PEC signals are controlled by an Ivium Compactstat potentiostat (10) linked to the three electrodes. Meanwhile, the output photocurrent responses are received and analysed by PC operated Ivium software (11).

Another PEC measurement set-up shown in Figure 2-2 conducted the EQE (IPCE) spectra, using the lock-in amplifier approach. The composition of the PEC cell (1) is the same as the previous set-up in Figure 2-1. Though instead of LEDs, a 100 W quartz halogen lamp (Bentham ILD-D2-QH) and a monochromator (Bentham TMc

300) are employed as light sources (2), calibrated by a Si photodiode. An optical chopper (3) driven by a controller can generate square wave lights with a specific frequency (usually 17 Hz). The chopping frequency is also input to the lock-in amplifier (4) (Stanford Research Systems SRS 830). The phase lag of the assembly was nulled against the fast Si-photodiode. The three-electrode system is connected to an Ivium Compactstat potentiostat (5) for bias and controlled by a signal generator (6). At the same time, the output signals (current) from the potentiostat (along with input from chopper) were acquired by the lock-in amplifier. Finally, a custom LabView built script (7) is used to control the lock-in amplifier and collect the photocurrent responses.

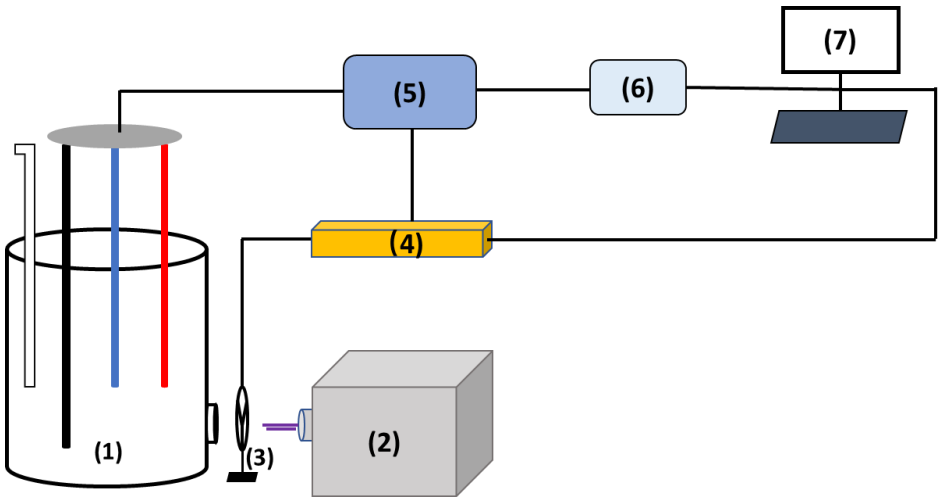

Figure 2-2 Photoelectrochemical set-up II.

The PEC set-up II (Figure 2-2) is much easier to change different illumination energies with small step sizes than LED-based set-up I (Figure 2-1), which is beneficial to acquire a complete EQE spectrum. The EQE calculation method has been shown in the previous chapter. Both photoelectrochemical experiments were carried out in Ar (or O_2)-saturated aqueous solutions containing 0.1 M Na_2SO_4 (or Na_2SO_3) at pH 12. Sodium hydroxide aqueous solutions were used to adjust the pH of the electrolyte. Sodium sulfate, sodium sulfite and sodium hydroxide were purchased from Sigma-Aldrich company with a high purity of 99.99+%. The scan rate

of photocurrent measurements usually is 5 mV s^{-1} in this thesis. The photon flux values vary with the illumination conditions and are shown alongside the results in the following chapters. In order to easily compare the as-received data with literature, all applied potentials with respect to Ag/AgCl are referred to against the reversible hydrogen electrode (RHE), following Nernst equation:

$$E_{RHE} = E_{Ag/AgCl} + 0.059\,pH + E^{o}_{Ag/AgCl}$$

where, E_{RHE} is the potential vs RHE, $E^{\circ}_{Ag/AgCl}$ is the standard Ag/AgCl potential at 25 °C (+0.197 V vs RHE), and $E_{Ag/AgCl}$ is the applied potential vs Ag/AgCl.

2.2.6 Electrochemical characterisations

Electrochemical characterisations can give a clear insight into the electrochemical behaviours of various thin films at SLJ, which is able to support the analysis of PEC measurements. The set-up of electrochemical characterisations, including CV (e.g., Figure 3-4 and Figure 4-9) and LSV (e.g., Figure 4-17) are the same as the equipment shown in Figure 2-1, except for the light source ((8) and (9)) in this thesis. The electrolyte conditions are also the same as PEC measurements. The electrochemical performances, such as Faradaic current, capacitance and so forth were observed using Ivium software in the dark.

Electrochemical Impedance Spectra (EIS) were recorded with a Modulab potentiostat and frequency response analyser with 13 mV RMS amplitude of modulation between 1.7 Hz and 11.7 kHz in Ar (or O_2)-saturated 0.1 M Na_2SO_4 aqueous solutions at pH 12. The experimental configurations are the same as PEC cell, employing a three-electrode system. In this thesis, the EIS data was converted into two expressions: capacitance-voltage curves and Mott-Schottky plots. The Mott-Schottky equation is a widespread approach to study the properties of thin films at film/electrolyte interface. It can not only indicate the characteristics of electrical conductivity (n- or p-type) but also (semi-)quantitatively show the charge

carrier density and flat band position of various thin films. The Mott-Schottky expression and detailed analysis will be shown in the following chapters.

2.2.7 Thin films preparation

All thin film synthesis procedures in this thesis can be summarized into four steps, as shown in Figure 2-3. The first step is the preparation of precursor solutions or nanoparticle suspensions. The aim of this step is to obtain a precursor that can be homogeneously spin-coated onto FTO substrates. Secondly, the solutions (suspensions) were dropped onto a FTO substrate (2.5 cm × 2.5 cm) using a 100 μL pipette, followed by spin-coating to acquire a thin film. Thirdly, the wet film was dried on a hot plate for a few minutes. Finally, the second calcination of the as-received film was processed in a furnace at relatively high temperature (e.g., 600°C) to remove chemical additives, and/or crystallise thin films.

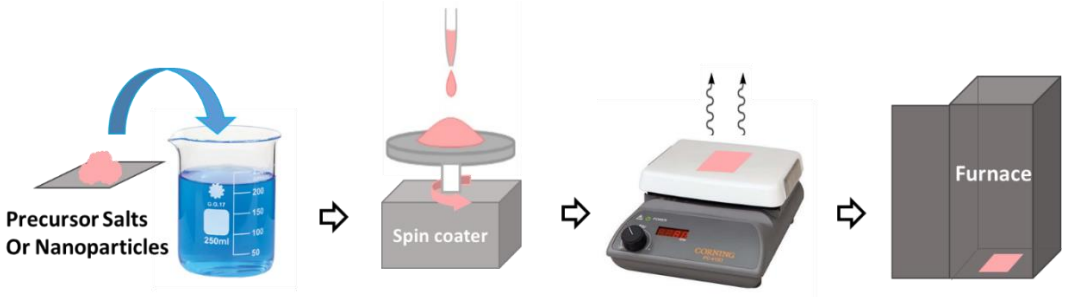

Figure 2-3 The process of thin films preparation.

Figure 2-4a displays various precursor solutions that are used to spin coat on FTO substrates. After the deposition of those precursors and annealing at appropriate temperatures, the as-received thin films are shown in Figure 2-4b. The nanostructured $LaFeO_3$ film (LFO (1)) was prepared based on nanoparticle suspensions, and the rest three thin films, $LaFeO_3$ (LFO (2)), $GaFeO_3$ (GFO), and $BiFeO_3$ (BFO) were synthesised by sol-gel method. The detailed procedures of thin film synthesis can be found in the Experimental Section of each chapter. After

comparing more than 20 samples, the direct sol-gel thin film synthesis (e.g., LFO (2) and GFO) shows high reproducibility of the deposition method, while nanostructured thin film synthesis (e.g., LFO (1)) is affected by various factors such as particle grinding and suspension temperature, leading to relatively large differences in film thickness and morphology. The detailed differences linked to PEC performance between two thin film preparation approach will be discussed later. All thin films are optically transparent and mirrorlike, which is described based on the Figure 2-4b. The diffuse reflectance and transmittance spectra and SEM images will reveal the accurate nature of thin films in terms of transparency and smoothness, for example, SEM images of nanostructured LFO film show a highly corrugated surface morphology. The similar bandgap values of these samples lead to an almost identical colour, though many factors such as the different grain sizes and film thickness may play a significant effect on the sample colours.

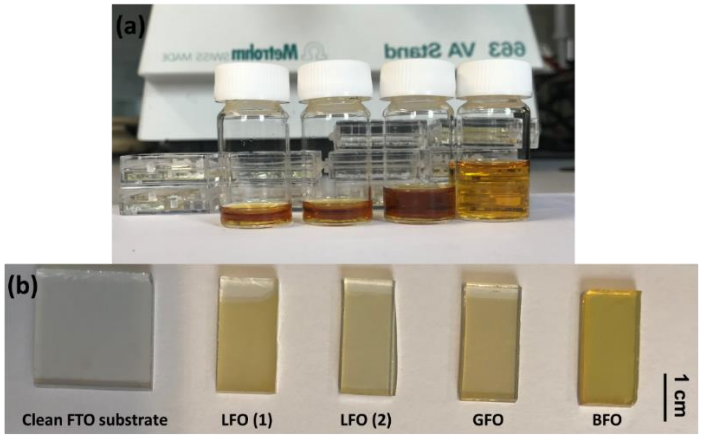

Figure 2-4 Various precursor solutions (a); and FTO-coated glass substrates before and after the deposition of thin films (b).

2.3 References

(1) Gärtner, W. W. Depletion-Layer Photoeffects in Semiconductors. *Phys. Rev.* **1959**, *116*, 84–87.

CHAPTER 3.

Heterojunction and cocatalyst for improving the EQE and onset potential of nanostructured $LaFeO_3$ photocathode

Portions of this chapter were published in:

Sun, X.; Tiwari, D.; Fermin, D. J. Nanostructured $LaFeO_3$ Photocathodes with Onset Potentials for the Hydrogen Evolution Reaction Over 1.4 V vs. RHE. *J. Electrochem. Soc.* **2019**, *166*, H764–H768.

X.S. prepared all samples and conducted all experiments reported in this thesis. The SEM and EIS characterisations were performed in collaboration with D.T.

3.1 Abstract

The photoelectrochemical properties of phase-pure $LaFeO_3$ (LFO) nanostructured films are investigated upon modification with a thin TiO_2 film and Pt nanoparticles as a catalyst. $LaFeO_3$ with crystallite domains in the range of 60 nm are prepared by thermolysis of an ionic-liquid precursor and subsequently deposited onto FTO-coated glass by spin-coating. Deposition of a TiO_2 layer by solution-based methods leads to the formation of a heterojunction, attenuating dark current associated with hole-transfer (water oxidation) at potential above +1.4 V vs the reversible hydrogen electrode (RHE). The LFO/TiO_2 heterojunction features photocurrent onset potential for the hydrogen evolution reaction of +1.47 V vs RHE, which is one of the most positive values reported for a single absorber. Deposition of Pt nanoparticles at the LFO/TiO_2 heterostructure generates a significant increase in the HER photocurrent, although bulk recombination remains an important challenge in these constructs.

3.2 Introduction

3.2.1 Overview of current photocathodes

Many p-type materials have been studied as photocathodes for hydrogen evolution reaction (HER). Currently, PV-grade photocathodes such as InP, $GaInP_2$, CdTe and $CdIn_{1-x}Ga_xSe_2$ attract widespread attention, mainly due to their efficient energy conversion efficiency.[1] However, as introduced in Chapter 1, PV-grade materials are typically non-earth-abundant, especially for those materials that contain indium. In contrast, a large percentage of non-PV-grade materials (e.g., metal oxides) are cost-efficient and stable, which increases the scalability of PEC water splitting technology. Complex transition metal oxides comprise a vast family of

compounds, as shown in Table 1-1 and recently reviewed by Rajeshwar and co-workers[2]. Although significant efforts have been devoted to investigating metal oxides-based PEC cells, transition metal oxides as photocathodes for the HER have been significantly less studied than photoanodes materials. Cu_2O remains the benchmark, showing external quantum efficiency (EQE) values as high as 76% and photocurrent onset potential of +0.48 V vs RHE in the presence of a TiO_2 stabilization layer deposited by ALD.[3] On the other hand, Chapter 1 mentions that ferrite-based ternary oxides can keep those advantages from hematite, such as chemical stability and favorable band-gap energies in PEC water splitting process. Several ferrite photocathodes have been reported including $YFeO_3$,[4] $CaFe_2O_4$,[5] $BiFeO_3$,[6] $PrFeO_3$[7] and so on.

However, it should be noted that the performance of these oxides-based photocathodes mentioned above remains significantly below the target required for commercial water splitting technologies. Although they may hold the key to viable and scalable PEC water splitting devices, our current knowledge on their structure-performance relationships remains very limited.

3.2.2 The selection of absorber ($LaFeO_3$)

Lanthanum iron oxide, $LaFeO_3$ (LFO), is also a promising ferrite-based photocathode material in the field of direct generation of H_2 from water, using solar energy.[8–12] It has a perovskite oxide structure (ABO_3), where A site is occupied by the larger cation with 12-fold oxygen coordination, the smaller cation tends to be in B site with 6-fold oxygen coordination and they are surrounded by cuboctahedral anions (O). It is well known that the composition and structure of perovskites are flexible. Consequently, there are more opportunities to tune the electronic structure and composition of the perovskite oxides, which has significant effects on the enhancement of PEC behaviour, as shown in the next chapter. In addition, numbers of perovskite oxides have attractive band alignments for PEC water splitting. To be

specific, earth-abundant LFO photocathode presents a band-gap energy in visible light region (2.1-2.7 eV).[8-12] More importantly, the valence band position and conduction band position of LFO straddle the chemical potential for both OER and HER, respectively, so that LFO can be either photocathode or photoanode under appropriate synthesis conditions. This band alignment also suggests LFO can be a superior candidate of bifunctional photoelectrode in the application of tandem PEC water splitting cells. Secondly, LFO photocathode can remain active for a long-term application.[9] Besides, Celorrio et al.[8] reported photovoltages as high as +1.2 V vs RHE for the HER at LFO, indicating that LFO photocathode can split water without external bias applied. Other studies involving LFO have also observed high photovoltages but EQE for the HER less than 1%.[9–11] Such low EQE value limits the development of LFO photocathode in practical applications of solar water splitting. It has been reported that the origin of carrier losses at LFO is ascribed to low overpotential for oxygen evolution and poor catalytic ability for water reduction;[8,9] however, it remains to be fully elucidated and solved. Thus, LFO photocathode is selected as the research object in this chapter.

3.2.3 The strategies for improving PEC performance of nanostructured $LaFeO_3$ photocathode

Currently, the innovation of LFO photocathode has mainly focused on atom doping and synthesis method optimization, which will be further discussed in the next chapter. In this work, building heterojunction and loading co-catalyst are chosen as two approaches for enhancing the PEC properties of LFO film. As mentioned before, semiconductor electrodes coated by thin film layers of TiO_2 can not only decrease photo-corrosion, but also improve the separation and transfer of carriers inside semiconductors.[13–16] Considering LFO band alignment, TiO_2 is a potential candidate to introduce benefits to LFO photocathode in the process of PEC water splitting. Because the combination of LFO and TiO_2 can form a heterojunction

(type II), achieving highly efficient charge separation and transfer. Moreover, Cameron and Laurence[17] reported that TiO_2 as a blocking layer can prevent the migration of photoinduced carriers to react at interface. This tends to imply that TiO_2 thin film has the potential to block photogenerated holes for oxygen evolution at LFO. On the other hand, platinum as an effective co-catalyst has been widely accepted for the enhancement of HER, as the Gibbs free energy of Pt for hydrogen adsorption close to zero leads to high activity.[18] Therefore, loading Pt nanoparticles (NPs) is likely to make LFO increase the surface charge-transfer kinetics.

The PEC properties of nanostructured LFO photocathodes by introducing a thin TiO_2 film as a hole-blocking layer and Pt nanoparticles as electrocatalysts are systematically explored. The fabrication of the photoactive constructs only involves solution-based methods. Systematic analysis of the electrochemical responses as a function of the LFO modifications provides information about the band edge energy offset of the oxide, while generating a 10-fold increase in the photocurrent responses. The photocurrent onset potentials also achieved more positive than +1.4 V (vs RHE) for the HER in this study. To the best of my knowledge, this is the largest onset potential reported for a single absorber photocathode.

3.3 Experimental Section

3.3.1 Materials

$La(NO_3)_3{\cdot}6H_2O$ (99.999%), $Fe(NO_3)_3{\cdot}9H_2O$ (99.999%), trisodium citrate (99%), $Na_2PtCl_6{\cdot}6H_2O$ (98%), $NaBH_4$ (98%), titanium isopropoxide (97%), $K_4Fe(CN)_6$ (99.999%), KNO_3 (99.999%), and FTO-coated glass (surface resistivity ~ 7 Ω sq^{-1}) were purchased from Sigma-Aldrich company. Ethyl cellulose (48%) was purchased from Acros company. Solvents: ethanol (99.8%), iso-propanol (99.8%), acetone (99.5%) and terpineol were purchased from Sigma-Aldrich company. Distilled water was

produced by Milli-Q systems (18.4 MΩ cm). All materials were used directly without further purification.

3.3.2 The purifying of FTO substrates

FTO-coated glass substrates were cleaned ultrasonically (prior to spin coating) by soapy water (Decon), iso-propanol and acetone approximately five minutes each, in that order. Finally, FTO substrates were washed with distilled water to remove any remaining organic substances and dried with argon gas.

3.3.3 The synthesis of $LaFeO_3$ nanoparticles

LFO nanoparticles were prepared by employing a highly versatile ionic liquid-based precursor used for synthesizing a wide range of perovskite nanostructures. Specifically, stoichiometric amounts of $La(NO_3)\cdot 6H_2O$ aqueous solution (1 mL), $Fe(NO_3)\cdot 9H_2O$ aqueous solution (1 mL) and 1-ethyl-3 -methylimiamidizolium acetate (ionic liquid, 2 mL) were mixed, stirred with a rotation speed of 400 rpm and dried at 80 ^oC for 3 hours on a hotplate. Then, 200 mg cellulose was added into the mixture with further stirring around 10 minutes to obtain homogenous gel. Finally, the gel was calcined at 900 ^oC (ramp rate: 5 $^oC\ min^{-1}$) for 2 hours in air, followed by cooling naturally to room temperature to form orange LFO nanoparticles.

3.3.4 The synthesis of Pt nanoparticles precursor

Pt NPs precursor was synthesized by borohydride reduction of platinum salts in an ice bath condition in a vial.[19] 38.8 mM trisodium citrate was added to 1 mM $Na_2PtCl_6\cdot 6H_2O$ aqueous solution (10 mL), stirred at 300 rpm for 5 minutes. Subsequently, 10 mM ice-cold freshly prepared $NaBH_4$ aqueous solutions were quickly added dropwise to this solution under vigorous stirring conditions. The colour of the solution changed from pale yellow to dark grey once the reduction was completed.

3.3.5 The synthesis of TiO_2 precursor

TiO_2 precursor was prepared by a simple solution process. Titanium isopropoxide (11.2%) was diluted in hydrochloric acid (0.3%) and ethanol (88.5%), followed by stirring at 800 rpm for 3 hours.

3.3.6 The preparation of various thin film-based photoelectrodes

All thin film constructs were prepared by spin-coating these precursors mentioned above onto FTO substrate. For LFO NPs precursor, the as-prepared nanoparticles were ultrasonically dispersed in an ethanol solution (3.8% wt.), containing ethyl cellulose (0.5% wt.) and terpineol (36.0% wt.). Then, the LFO precursor was spin-coated onto FTO glass with a rotation speed of 2000 rpm for 30 seconds. The final LFO thin film photoelectrode was heated at 500 ^oC for 15 minutes to remove additives. Similarly, as for TiO_2 thin films, TiO_2 precursor was spin-coated onto FTO glass (4000 rpm for 60 seconds). The films were dried at 225 ^oC for 5 minutes, followed by heating to 500 ^oC for 30 minutes after each coating step. Pt precursor was spin-coated (2000 rpm for 30 seconds), leading to a maximum Pt loading of 0.19 mg cm^{-2} for each deposition step. The films were subsequently heated at 400 ^oC for 30 minutes, leading to the formation of Pt nanoparticles.

3.4 Results and discussion

3.4.1 XRD characterisation of $LaFeO_3$, TiO_2 and Pt nanoparticles

Figure 3-1a displays powder XRD patterns of LFO, TiO_2 and Pt nanoparticles which are indexed employing JCPDS-ICDD Files No. 01-075-0541, 01-086-1157 and 00-001-1194, respectively. The diffractograms of LFO, TiO_2 and Pt NPs are consistent with pure cubic, tetragonal, and cubic phase, respectively. The TiO_2 coating (calcined at 500 ^oC) is the anatase phase.

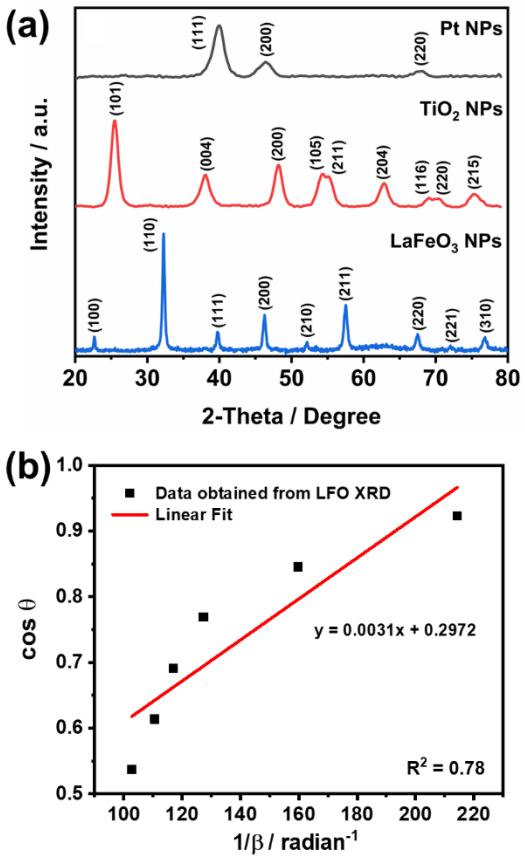

Figure 3-1 (a) XRD patterns of the LFO, TiO_2 and Pt nanoparticles (NPs) and (b) calculation of coherent diffraction domain size of LFO NPs, using Scherrer equation.

The XRD patterns were recorded at a san rate of 0.5 degree 2-theta/minute (a step size of 0.02 degree 2-theta and 2.4 seconds per step) and a divergent slit of 2 cm. The coherent diffraction domain size of NPs can be estimated from XRD patterns, based on Scherrer equation:

$$L = \frac{K\lambda}{\beta cos\theta}$$

Where *L* is the coherent diffraction domain size, *K* is Scherrer constant, λ is incident wavelength of X-ray ($\lambda_{Cu\,K\alpha}$ = 0.154056 nm), β is the full width at half height of the diffraction peak in radian and θ is the angle of the diffraction peak. The coherent diffraction domain sizes of LFO, TiO_2 and Pt NPs are 26 nm, 7 nm, and 3 nm, respectively. The relatively small coherent diffraction domain sizes of TiO_2 and Pt NPs can also be predicted from the broadening of the XRD features. It should be

noted that those values mentioned above do not take into account the instrumental broadening. Thus, the β values extracted from Figure 3-1a may be overestimated. The instrumental broadening is typically measured by running a high-quality standard sample (e.g., LaB_6) with large particle sizes and no defects.

The peaks in the region from 20 degree 2-theta to 60 degree 2-theta were selected from the XRD pattern of LFO NPs. The linear fit of cosθ versus 1/β plot for those peaks is shown in Figure 3-1b. According to Scherrer equation, the slope of the fit equation shown in Figure 3-1b is equal to Kλ/L, thereby giving the coherent diffraction domain size of 27 nm. The y-intercept of the fit equation has no physical meaning. However, if the linear fit plot is forced to pass through the origin, the value of R^2 will be very low. Table 3-1 summaries the coherent diffraction domain sizes of LFO calculated from each peak. Their average value is 26 nm, which matches well with the linear fit results.

Table 3-1 The coherent diffraction domain sizes of LFO NPs estimated from each peak

Peak	coherent diffraction domain size / nm
(100)	31.83
(110)	25.90
(111)	22.70
(200)	23.19
(210)	24.70
(211)	26.23

3.4.2 Morphology characterisation of $LaFeO_3/TiO_2$ construct

Figure 3-2a shows the morphology of LFO thin film, which reveals the grains of LFO NPs with a mean size of 60 nm. After the deposition of TiO_2 thin film onto LFO

surface, the film morphology changes are shown in Figure 3-2b, indicating cracked morphologies and entirely coating over the LFO assembly. Although the TiO_2 layer cracked due to once coating and the uneven LFO NPs, it has little impact on PEC properties, which will be discussed later. The SEM cross-section image in Figure 3-2c reveals the film with a highly corrugated surface and little contrast between the LFO and TiO_2 domains. EDX cross-section analysis of the thin film (Figure 3-2d) shows a contrast between Si Kα1 and Sn Lα1 signal and those associated with La Lα1, Fe Lα12 and Ti Kα1. The intensities maps suggest that the total thickness of the LFO/TiO_2 film is in the range of 250 to 300 nm.

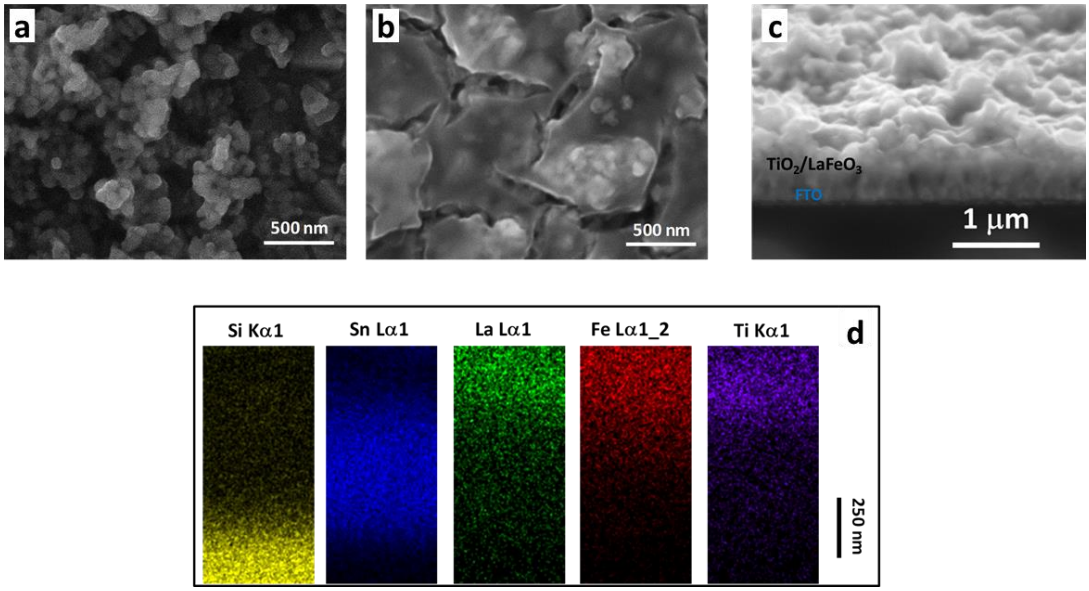

Figure 3-2 Morphology of the LFO/TiO_2 photoelectrodes: top view scanning electron micrographs (SEM) image of the LFO film prior (a) and after (b) TiO_2 deposition; cross-sectional SEM image (c) and EDX maps (d) of LFO/TiO_2 films, revealing domains associated with FTO, LFO and TiO_2.

The EDX mapping images show some unexpected features, for example, Si signals can be seen everywhere in the image of Si Kα1 (Figure 3-2d), though they should concentrate at the bottom as glass at the bottom is the only Si source. This can be rationalized in terms of the mounting angle of the sample. The cross-sectional EDX analysis instrument (Oxford Xmax-80 detector, in the School of Chemistry, University of Bristol) requires that the sample mounting should be tilted to around 70^o, as

shown in Figure 3-3. The electron beam penetrates the sample and excites a pear-shape volume for each point/pixel analysed. When the electron beam (15 keV) scans from glass to FTO (Figure 3-3a) or samples (Figure 3-3b), it can still excite the glass (Si element) due to the tilt of the sample and the way X-Rays travel through the sample to the EDX detector. On the other hand, the charging of samples also tends to result in such unexcepted features due to the movement of samples.

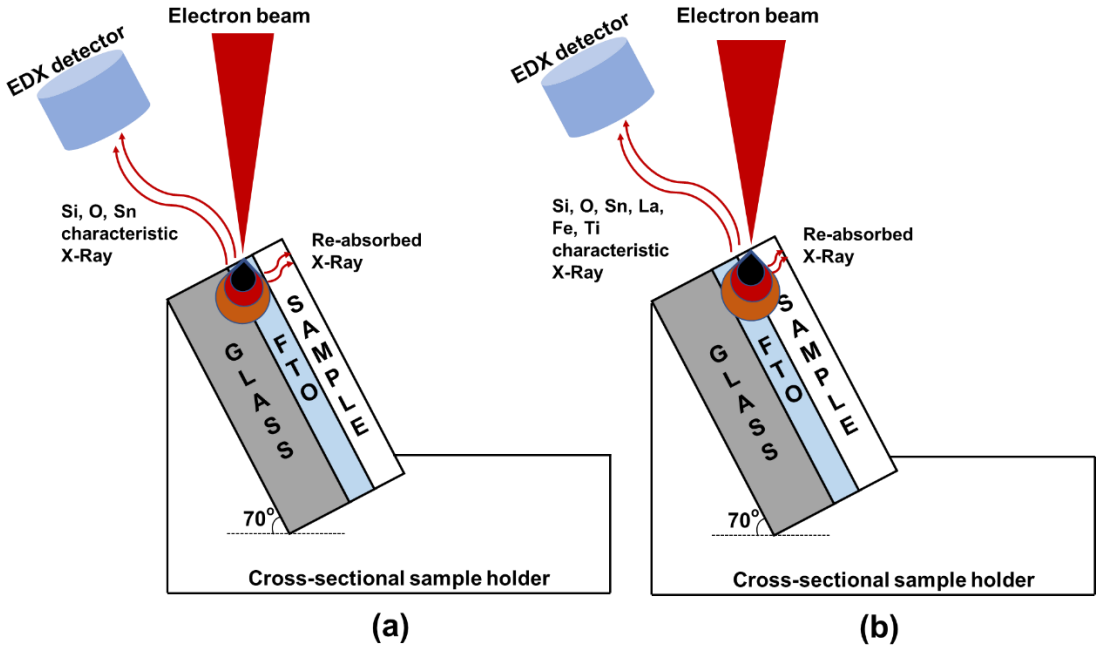

Figure 3-3 The schematic diagram of the cross-sectional EDX analysis: the electron beam moves from glass to FTO (a) and to samples (b).

3.4.3 Band offsets upon the modification of TiO_2 films and Pt NPs

Figure 3-4a contrasts cyclic voltammograms (CV) of as-deposited LFO films and after various modifications recorded at 50 mV s^{-1} in Ar-saturated electrolyte solution containing 0.1 M Na_2SO_4 at pH 12 in the dark. The LFO electrode shows a small capacitive current of the order of 1×10^{-6} A cm^{-2} across a large potential range, with a noticeable broadening at potentials above +1.2 V vs RHE, suggesting interfacial hole accumulation. Indeed, we have constructed a Mott-Schottky plot of LFO film (Figure

3-4b) from electrochemical impedance data, showing the characteristic p-type behavior. The density of acceptor states (N_A) and flat-band potential (E_{FB}) in LFO are calculated from slope and x-intercept of the linear portion of plot, respectively, employing the Mott-Schottky equation:

$$\frac{1}{C^2} = \frac{2}{A^2 q \varepsilon \varepsilon_0 N_A}\left[(E_{FB} - E) - \frac{kT}{q}\right]$$

where *A* is the area of electrode and is assumed to be equal to the geometric area, ε and ε_0 are the relative and free space permittivity, respectively. A relative permittivity of 7890 (±200) is calculated from the geometric capacitance, which is in agreement with previously reported values.[21] The x-intercept expresses LFO with a flat band potential of +1.44 (±0.01) V vs RHE. This value is consistent with the recent report by Choi and co-workers on LFO thin films.[20] A doping density of the order of 6×10^{17} cm^{-3} can be estimated from the slope of the Mott-Schottky, although this value should be considered with caution. On the one hand, we have used the geometric surface area that is smaller than the actual surface area of electrode due to the rough electrode surface, which may significantly overestimate the density of acceptor states. When the slope of Mott-Schottky plot is determined, the majority carrier density will decrease with the increase of the electrode surface area, following the Mott-Schottky equation. On the other hand, there is also uncertainty in the relative permittivity of ferrites which are rather large (of the order of 10^4) and strongly dependent on the material structure.[21] As the interface going into accumulation regime, the onset of the oxygen evolution reaction (OER) can be observed close to +1.5 V vs RHE in Figure 3-4a.

Deposition of Pt nanoparticles (LFO/Pt, maximum loading of 0.19 mg cm^{-2}) leads to an increase of the capacitance across the whole potential range. By contrast, the capacitive current marginally increases upon deposition of TiO_2 thin film onto LFO (LFO/TiO_2), which promotes interfacial charge accumulation at potentials lower than

+0.6 V vs RHE. The CV of a TiO_2 film deposited onto the FTO electrode (labelled as TiO_2 in Figure 3-4a) shows similar responses to the LFO/TiO_2 films but displaced by approximately 200 mV towards more negative potentials. The shift in the onset potential for electron accumulation in the TiO_2 layer is a manifestation of the built-in potential generated upon equilibrating the Fermi levels at the LFO/TiO_2 heterojunctions.

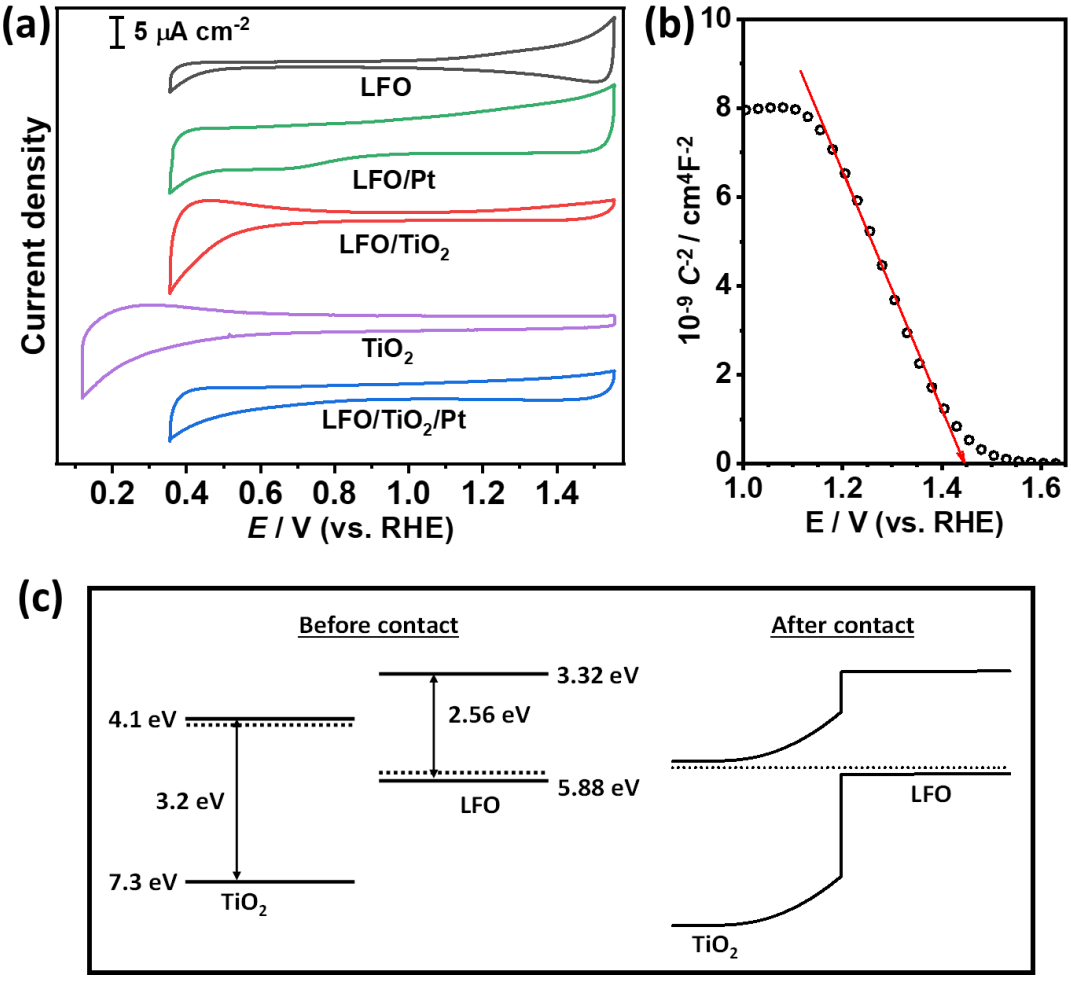

Figure 3-4 Cyclic voltammograms of the various constructs recorded at 50 mV s^{-1} in Ar-purged aqueous 0.1 M Na_2SO_4 solution at pH 12 in the dark (a); Mott-Schottky plot of LFO in Ar-saturated 0.1 M Na_2SO_4 aqueous solution at pH 12 (b); and estimation of the band alignment of LFO and TiO_2 before and after the formation of the heterojunction, based on the Mott-Schottky plot of LFO and the majority carrier density of the order of 10^{17} cm^{-3} in the TiO_2 film (c).

Based on CV, Mott-Schottky plot and band-gap energy (discussed in the section of 3.4.6), the band diagram of LFO and TiO_2 prior and after contact (Figure 3-4c) is constructed to visualize the built-in electric field between LFO and TiO_2. The majority carrier density in the TiO_2 film is assumed to be the same as LFO with the order of 10^{17} cm^{-3} since the majority carrier density has little effect on visualization analysis in Figure 3-4c. As the TiO_2 annealing was restricted to 500 ^oC, we expect a rather abrupt junction at LFO/anatase nanoscale domains with very little elemental interdiffusion. As the junction is formed, we predict a shift of approximately 0.2 V in the conduction band edge of TiO_2 towards more positive potentials in Figure 3-4c, following the shifts in the onset of electron accumulation of TiO_2 on FTO with respect to TiO_2 (Figure 3-4a). This case is expected to be rather different from epitaxial LFO films grown by pulsed laser deposition onto single-crystalline $SrTiO_3$ surfaces.[22] A slight shift of valance band edge position of LFO onwards more negative potentials is also expected; however, the main effect seen upon the formation of the LFO/TiO_2 junction is the suppression of the OER at positive potential. Such type II heterojunction (p-n junction) can promote the charge carrier transfer efficiency, which has a grand influence on PEC properties of LFO/TiO_2 and LFO/TiO_2/Pt constructs, as discussed later. In addition, features associated with carrier accumulation are less evident in the case of LFO/TiO_2/Pt heterostructure, due to the increase in the capacitance across the entire potential range introduced by the metallic domains.

3.4.4 PEC characterisation of various constructs

Figure 3-5a contrasts cyclic voltammograms of LFO and LFO/TiO_2 constructs at 5 mV s^{-1} in Ar-saturated 0.1M Na_2SO_4 aqueous solution at pH 12 under a square wave light perturbation at 464 nm and photon flux of 2.17×10^{15} cm^{-2} s^{-1}. Photocurrent responses associated with HER are clearly seen across the potential window, with a significantly larger amplitude in the case of LFO/TiO_2. These results bring about two

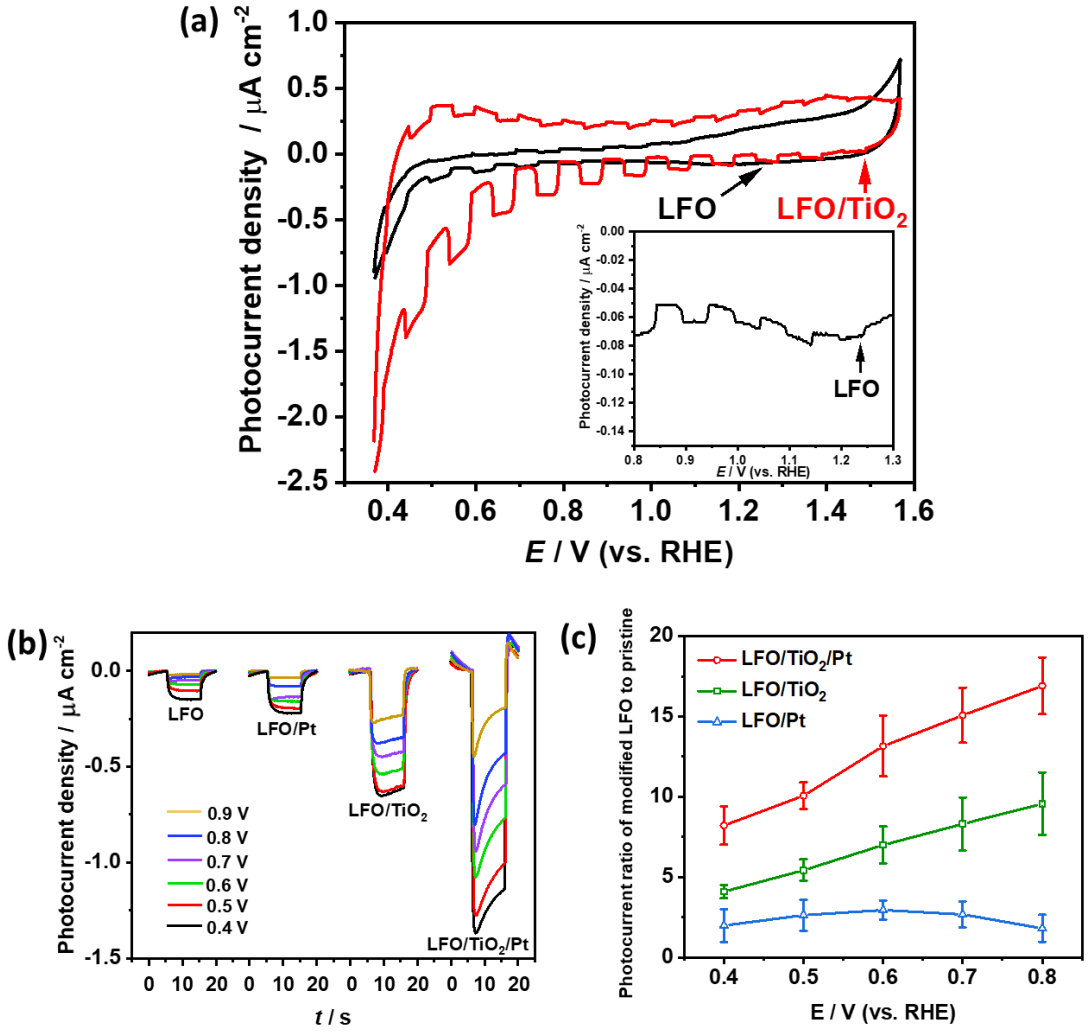

Figure 3-5 Photoelectrochemical responses of various nanostructured photocathodes in Ar-saturated 0.1 M Na_2SO_4 aqueous solutions (pH 12) under the illumination at 464 nm: (a) cycling voltammogram of LFO and LFO/TiO_2 under photon flux of 2.17×10^{15} cm^{-2} s^{-1}; (b) transit photocurrent responses under photon flux of 3.44×10^{15} cm^{-2} s^{-1}; and (c) photocurrent ratio of three LFO-based constructs to pristine as a function of potential.

interesting observations: (1) the deposition of an insulating layer leads to an increase of the cathodic photocurrent responses across the entire potential range and (2) the photocurrent onset potential is shifted to values as positive as +1.47 V vs RHE. Based on the proposed band alignment in Figure 3-4c, the conduction band of TiO_2 is estimated to be about 0.78 eV below the conduction band and 1.78 eV above the valence band of LFO. Consequently, TiO_2 can effectively block the OER mediated by

holes in the valence band of LFO, while photogenerated electrons can be transported via the conduction band of TiO_2. This mechanism is different from the trap-mediated transport observed in TiO_2 protected photoanodes.[23]

Photocurrent transient responses for the various thin film constructs recorded under 10 second illumination at 464 nm and different applied potentials are contrasted in Figure 3-5b. The deposition of Pt NPs onto the LFO films only leads to small increases in the photoresponses with respect to the as-deposited LFO electrodes. Pt NPs as co-catalyst can accelerate the transfer of photogenerated electrons to reach LFO/electrolyte interface for HER, increasing the photocurrents. It can also be seen that the photocurrent rise time in the light on-transient and the relaxation in the off-transient are significantly slower at lower potentials. As described by Zhang et al.,[24] this behavior can be rationalized in terms of trap-limited transport of majority carriers. At low potentials, trap-states are filled with electrons, slowing down the transport of holes to the back contact through the network of LFO nanoparticles. The photocurrent in the presence of TiO_2 film increases across the whole potential range while the photocurrent at the LFO/TiO_2/Pt construct shows the largest improvement in the photocurrent. The transient responses show a noticeable decrease after the initial response upon illumination, with a positive photocurrent overshoot in the off-transient. These responses provide evidence of surface recombination reactions, which are not apparent in the absence of the TiO_2 film. This may be due to the presence of defect states in TiO_2 layer, leading to charge carrier recombination. Pt NPs are likely to further strengthen the effect of defect states, which results in even larger photocurrent spikes in the on-transient and off-transient.

It is known that photocurrent magnitude is strongly dependent on various factors, such as photon flux, pH of electrolyte, film thickness and so on. The photocurrents of three constructs normalized by that of LFO at different potentials can provide a

straightforward information related to the effect of TiO_2 layer and Pt NPs on LFO photocathode in Figure 3-5c. The normalized photocurrents of constructs coated by TiO_2 display an increase trend as the voltage is swept towards more positive value, while that of LFO/Pt assembly almost remains at same level. The band bending of TiO_2 (Figure 3-4c) are increasingly shaper when the potential is applied from negative to positive direction, benefitting the photogenerated charge carrier separation and transfer, which is also likely to imply the onset potential of LFO shifts towards more positive. By contrast, Pt NPs as co-catalysts show the same effect in the process of charge carrier transfer across the whole potential range. It can also be seen that there are some relatively large error bars obtained from 20 samples in Figure 3-5c. Because it is difficult to generate totally same thickness LFO samples based on spin-coating suspensions, as shown the corrugated surface of LFO in Figure 3-2c. But this has a little influence on the comparison of various LFO based constructs (before and after the deposition of TiO_2 film and / or Pt NPs) in PEC performance, since those modifications were based on the same pristine LFO sample.

3.4.5 Optimization of TiO_2 film and Pt NPs thickness

In order to optimize the photogenerated charge carriers transfer efficiency between LFO and TiO_2 layer, the CVs of FTO/TiO_2 and photocurrent vs. potential (J-V) plots of LFO/TiO_2 electrodes modified by one to three TiO_2 coating steps are shown in Figure 3-6a and b, respectively. Each deposition step is followed by drying at 225 ^oC (5 min) and annealing at 500 ^oC (30 min). To be specific, the CVs of various FTO/TiO_2 electrodes were performed in a aqueous solution containing 1 mM $K_4Fe(CN)_6$ and 0.1 M KNO_3, recorded at a scan rate of 50 mV s^{-1}. Figure 3-6a shows an

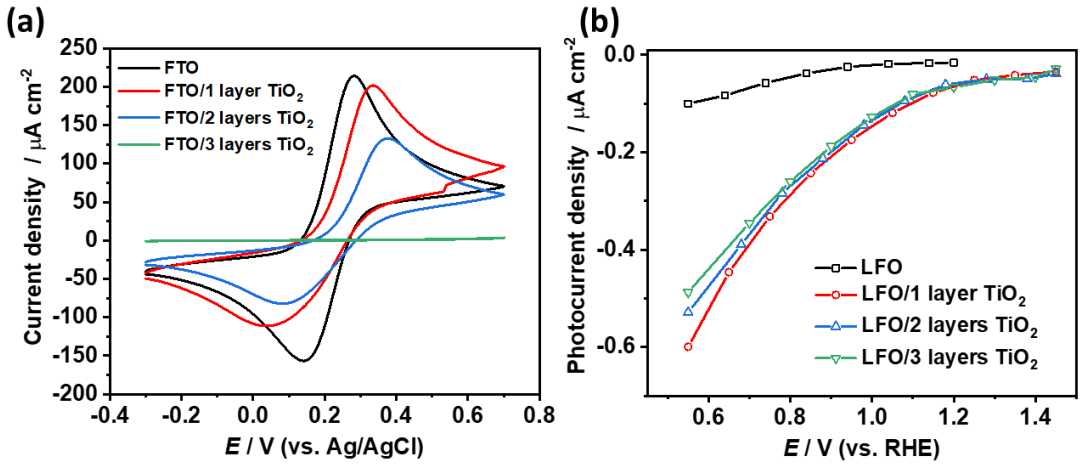

Figure 3-6 Cyclic voltammograms of TiO_2 with different thickness coated onto FTO substrate in a solution containing 1 mM $K_4Fe(CN)_6$ and 0.1 M KNO_3 measured at a scan rate of 50 mV s^{-1}(a); and photocurrent potential curves of as-deposited LFO films and after modified by TiO_2 with different thickness, measured in Ar-saturated 0.1 M Na_2SO_4 aqueous solution (pH 12) and a photon flux of 3.44×10^{15} cm^{-2} s^{-1}(b).

increase in the peak-to-peak separation after the first two deposition steps, while a significant drop in the current is observed after 3 deposition steps. Semi-quantitative analysis of the voltammetric responses employing the Nicholson-Shain formalism (Table 3-2) shows that the phenomenological charge transfer rate constant decreases by 40 times between 0 and 3 deposition coatings. The surface coverage of TiO_2 as a function of the number of coating steps is calculated on the basis of the partially covered electrode formalism.[28–31] We estimate that the TiO_2 coverage increases from 72.5% to 97.5% from 1 to 3 coating steps. Interestingly, the dependence of the photocurrent responses on the number of coating steps is rather small as shown in J-V plots (Figure 3-6b). The J-V curves were measured in Ar-saturated 0.1M Na_2SO_4 aqueous solution (pH 12) under a square wave light perturbation at 2.67 eV and recorded at 5 mV s^{-1}. A significant increase in the current is observed upon adsorbing the first TiO_2 layer, while less than 20% fall of the photocurrent is observed at negative potentials upon increasing the number of TiO_2 coating steps. This observation reveals that the coverage and thickness of the TiO_2 layer have little influence on the transport of photogenerated electrons. This is not

surprising given that the LFO conduction band edge is located well above the one of TiO_2 (see Figure 3-4), carrier transport to the surface occurs by the conduction band of the nanostructured TiO_2 layer. It can be anticipated that this process would manifest itself by the characteristic spectroscopic features of electrons in the TiO_2 conduction band which could be approached by time-resolved spectroscopy.

Table 3-2 Phenomenological first-order electron transfer rate for the oxidation of $Fe(CN)6^{4-}$ at TiO_2 modified electrodes

Sample	Charge transfer rate k^o / cm s^{-1} (±0.005)	Surface coverage
Clean FTO	0.47	0 %
FTO / 1 Layer TiO_2	0.13	72.5 %
FTO / 2 Layers TiO_2	0.10	78.6 %
FTO / 3 Layers TiO_2	0.01	97.5 %

Further information related to the effect of Pt NPs loading amount on LFO/TiO_2/Pt construct is also investigated in Figure 3-7. Photocurrent transient measurements of the LFO/TiO_2 with different Pt loading that is varied via the number of coating steps from 0.19 mg cm^{-2} to 0.76 mg cm^{-2} were conducted at different potentials under 10 seconds illumination at 464 nm in Ar-saturated 0.1M Na_2SO_4 aqueous solution (pH 12). The photocurrent responses exhibit a maximum value at Pt NPs loading of 0.38 mg cm^{-2}. The excessive loading amount forms Pt-based trapping sites, resulting in the photocurrent density increasingly drops. In addition, the excessive loading of Pt NPs (above 1 mg cm^{-2}) darkens the color of the film, which indicates that Pt NPs compete with LFO for light absorption. In this case, Pt NPs can be regarded as light blocking centers, further lowering the photocurrent magnitude. From a cost point of view, LFO/TiO_2/Pt assembly may not meet cost-efficient due to the non-Earth-abundant Pt metal, though this process requires a relatively small loading

amount of Pt NPs. Therefore, developing highly efficient and low-cost co-catalysts for LFO is likely to be an interesting subject.

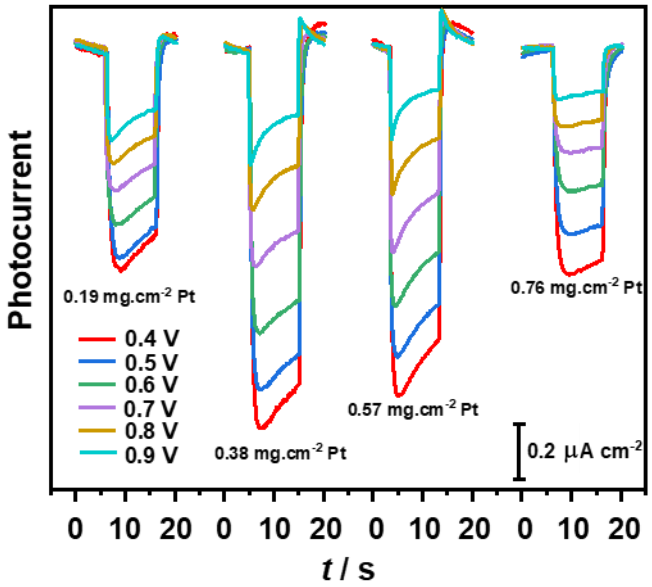

Figure 3-7 Photocurrent transient measurements of the LFO/TiO_2 with different Pt nanoparticles loading amount at different potentials in Ar-saturated 0.1 M Na_2SO_4 aqueous solution (pH 12) under illumination of 464 nm and photon flux of 3.44×10^{15} cm^{-2} s^{-1}.

3.4.6 Quantum efficiency and optical responses of various constructs

The quantum efficiency spectrum of various LFO based films at +0.5 V vs RHE is shown in Figure 3-8a and b, indicating that the deposition of TiO_2 and Pt co-catalyst onto LFO photocathode can increase external quantum efficiency (EQE) for HER over all wavelength window. The EQE as a function of wavelength can be contrasted with the optical responses of LFO films as probed by the diffuse reflectance spectra of the films in Figure 3-8c. The absorption coefficient of the LFO film is calculated from the transmittance and reflectance data in the region between 1.8 eV and 3.1 eV, and is larger than 3×10^4 cm^{-1} for the energies above around 2.5 eV in Figure 3-8d. Analysis of the optical responses based on Tauc plot (Figure 3-8e) shows two distinctive transitions separated by approximately 150 meV, which is similar to those reported in epitaxially grown LFO films.[32] Indeed, optical transitions in LFO are complex due to

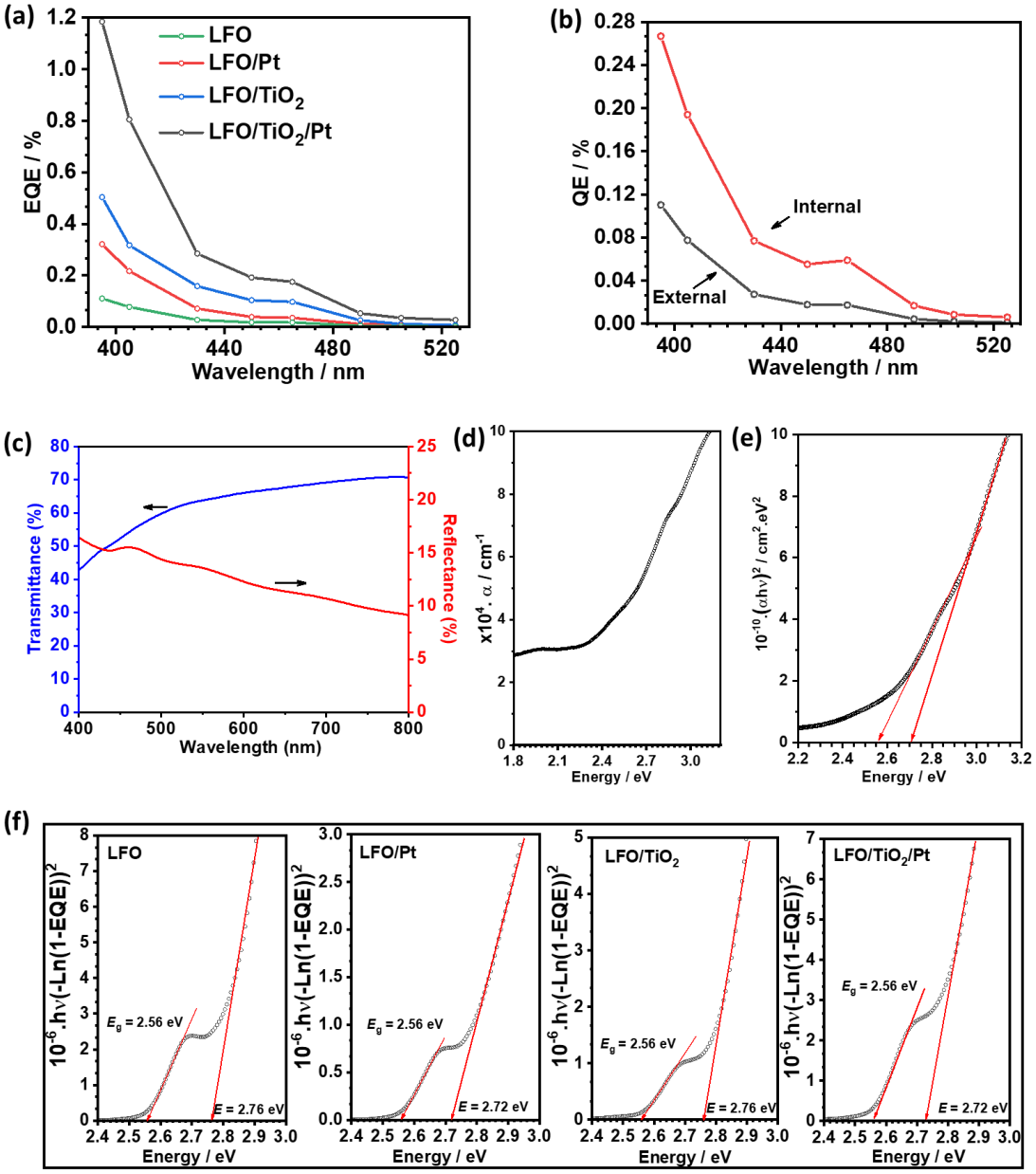

Figure 3-8 Quantum efficiency spectra of LFO based photocathodes at +0.5 V vs RHE in Ar-saturated 0.1 M Na_2SO_4 aqueous solution at pH 12: (a) external quantum efficiency spectra of various constructs and (b) internal and external quantum efficiency spectra of the LFO photoelectrode; Optical properties of the LFO film: (c) diffuse reflectance and transmittance spectrum, (d) absorption spectra, (e) Tauc plot analysis; and (f) equivalent plots estimated from the EQE spectra of the various photoelectrode constructs. Red arrows show the linear fitting of the Tauc plot, indicating two distinctive transitions in LFO.

multiple inter-band transitions involving majority and minority spin-states arising from the octahedral splitting of Fe 3d in t_{2g} and e_g levels, respectively.[32] This tends to

rationalise the quite wide LFO band-gap range (2.1 - 2.7 eV) reported,[8-12] though synthesis procedures may have effects on band-gap energy. The optics-based band gap calculation is contrasted with equivalent plots constructed from the EQE spectra of the various photoelectrode constructs shown in Figure 3-8f, which matches well with optical Tauc plot analysis. This close correlation between optical and photoelectrochemical responses demonstrates that carriers are generated and collected across the LFO spectral range with a fundamental bandgap at 2.56 eV. Moreover, the bandgap energy of LFO remains constant upon the deposition of TiO_2 layer and Pt NPs. We also observe some tailing in the optical and photoelectrochemical responses beyond the bandgap which can be associated with structural disorder in the nanostructured absorber layer.

Our findings offer an approach to improve the performance of these interesting and electrochemically robust materials. TiO_2 act as a hole-blocking layer increasing their collection efficiency at the back contact, while Pt nanostructures facilitate the HER reaction at the surface of the construct. Although evidence of surface recombination can be seen in the photoelectrochemical responses of LFO/TiO_2 heterostructures, bulk recombination remains the dominant carrier-loss pathway. Indeed, Figure 3-8b contrasts external and internal quantum efficiencies (IQE) spectra of LFO films, based on their reflectance and transmission spectra. The IQE is approximately three times larger than EQE across the whole visible spectrum, which further confirms the challenges associated with bulk recombination in this material. In this context, grain boundaries in the nanostructured films may represent a strong barrier to hole transport, given the tendency of La to segregate to the surface in the thermolysis of these type of precursors.[25–27] Consequently, improvement in EQE can be promoted by substantially increasing crystalline domains in LFO, as well as further optimization of the TiO_2 film thickness and HER catalysts size and loading.

3.5 Summary

Sequential deposition of TiO_2 thin films and Pt nanoparticles onto nanostructured LFO thin films employing entirely solution-based methods leads to a 10-fold increase in the photoelectrochemical responses towards the hydrogen evolution reaction. EQE values above 1% at 400 nm were recorded in alkaline solution (pH 12) at +0.5 V vs RHE. Integrating the EQE spectral response provides photocurrent responses up to -0.015 mA cm^{-2} under AM 1.5 illumination at +0.5 V vs RHE. However, the most striking observation of these constructs is the photocurrent onset potential close to +1.5 V vs RHE, which is the most positive value recorded for a single absorber photoelectrode. The TiO_2 layer acts as a barrier for hole transfer to the electrolyte, suppressing dark current and the loss of majority carriers (via water oxidation). The formation of a heterojunction at the LFO/TiO_2 interface is demonstrated by a positive shift in the onset potential of electron accumulation in the TiO_2 layer in the dark. These studies show the potential for this class of material to act as photocathode in sustainable integrated photoelectrochemical water-splitting. However, there are significant carrier losses in these systems which are dominated by bulk recombination in the nanostructured absorber layer.

3.6 References

(1) Walter, M. G.; Warren, E.; McKone, J. R.; Boettcher, S.; Mi, Q.; Santori, E.; Lewis, N. Solar Water Splitting Cells. *Chem. Rev.* **2010**, *110*, 6446.

(2) Rajeshwar, K.; Hossain, M. K.; Macaluso, R. T.; Janáky, C.; Varga, A.; Kulesza, P. J. Review—Copper Oxide-Based Ternary and Quaternary Oxides: Where Solid-State Chemistry Meets Photoelectrochemistry. *J. Electrochem. Soc.* **2018**, *165*, H3192.

(3) Luo, J.; Steier, L.; Son, M. K.; Schreier, M.; Mayer, M. T.; Grätzel, M. Cu_2O Nanowire Photocathodes for Efficient and Durable Solar Water Splitting. *Nano Lett.* **2016**, *16*, 1848.

(4) Díez-García, M. I.; Celorrio, V.; Calvillo, L.; Tiwari, D.; Gómez, R.; Fermín, D. J. $YFeO_3$ Photocathodes for Hydrogen Evolution. *Electrochim. Acta* **2017**, *246*, 365.

(5) Díez-García, M. I.; Gómez, R. Investigating Water Splitting with $CaFe_2O_4$ Photocathodes by Electrochemical Impedance Spectroscopy. *ACS Appl. Mater. Interfaces* **2016**, *8*, 21387.

(6) Radmilovic, A.; Smart, T. J.; Ping, Y.; Choi, K. S. Combined Experimental and Theoretical Investigations of N-Type $BiFeO_3$ for Use as a Photoanode in a Photoelectrochemical Cell. *Chem. Mater.* **2020**, *32*, 3262−3270.

(7) Freeman, E.; Kumar, S.; Thomas, S. R.; Pickering, H.; Fermin, D. J.; Eslava, S. $PrFeO_3$ Photocathodes Prepared Through Spray Pyrolysis. *ChemElectroChem* **2020**, *7*, 1365.

(8) Celorrio, V.; Bradley, K.; Weber, O. J.; Hall, S. R.; Fermín, D. J. Photoelectrochemical Properties of $LaFeO_3$ Nanoparticles. *ChemElectroChem* **2014**, *1*, 1667–1671.

(9) Wheeler, G. P.; Choi, K. S. Photoelectrochemical Properties and Stability of Nanoporous P-Type $LaFeO_3$ Photoelectrodes Prepared by Electrodeposition. *ACS Energy Lett.* **2017**, *2*, 2378–2382.

(10) Pawar, G. S.; Tahir, A. A. Unbiased Spontaneous Solar Fuel Production Using Stable $LaFeO_3$ Photoelectrode. *Sci. Rep.* **2018**, *8*, 3501.

(11) Díez-García, M. I.; Gómez, R. Metal Doping to Enhance the Photoelectrochemical Behavior of $LaFeO_3$ Photocathodes. *ChemSusChem* **2017**, *10*, 2457–2463.

(12) Wheeler, G. P.; Baltazar, V. U.; Smart, T. J.; Radmilovic, A.; Ping, Y.; Choi, K. S. Combined Theoretical and Experimental Investigations of Atomic Doping to Enhance Photon Absorption and Carrier Transport of $LaFeO_3$ Photocathodes. *Chem. Mater.* **2019**, *31*, 5890–5899.

(13) May, M. M.; Lewerenz, H. J.; Lackner, D.; Dimroth, F.; Hannappel, T. Efficient Direct Solar-to-Hydrogen Conversion by in Situ Interface Transformation of a Tandem Structure. *Nat. Commun.* **2015**, *6*, 8286.

(14) Fountaine, K. T.; Lewerenz, H. J.; Atwater, H. A. Efficiency Limits for Photoelectrochemical Water-Splitting. *Nat. Commun.* **2016**, *7*, 1–9.

(15) Verlage, E.; Hu, S.; Liu, R.; Jones, R. J. R.; Sun, K.; Xiang, C.; Lewis, N. S.; Atwater, H. A. A Monolithically Integrated, Intrinsically Safe, 10% Efficient, Solar-Driven Water-Splitting System Based on Active, Stable Earth-Abundant Electrocatalysts in Conjunction with Tandem III-V Light Absorbers Protected by Amorphous TiO_2 Films. *Energy Environ. Sci.* **2015**, *8*, 3166.

(16) Young, J. L.; Steiner, M. A.; Döscher, H.; France, R. M.; Turner, J. A.; Deutsch, T. G. Direct Solar-to-Hydrogen Conversion via Inverted Metamorphic Multi-Junction Semiconductor Architectures. *Nat. Energy* **2017**, *2*, 17028.

(17) Cameron, P. J.; Peter, L. M. Characterisation of Titanium Dioxide Blocking Layers in Dye-Sensitized Nanocrystalline Solar Cells. *J. Phys. Chem. B* **2003**, *107*, 14394–14400.

(18) Morales-Guio, C. G.; Stern, L. A.; Hu, X. Nanostructured Hydrotreating Catalysts for Electrochemical Hydrogen Evolution. *Chem. Soc. Rev.* **2014**, *43*, 6555–6569.

(19) Leuw, C. C.; Chen, S. T.; Liu, F. K. Spin-Coating-Derived Gold-Nanoparticle Memory. *J. Am. Ceram. Soc.* **2010**, *93*, 3142.

(20) Wheeler, G. P.; Baltazar, V. U.; Smart, T. J.; Radmilovic, A.; Ping, Y.; Choi, K.-S. Combined Theoretical and Experimental Investigations of Atomic Doping To Enhance Photon Absorption and Carrier Transport of $LaFeO_3$ Photocathodes. *Chem. Mater.* **2019**, *31*, 5890.

(21) Acharya, S.; Mondal, J.; Ghosh, S.; Roy, S. K.; Chakrabarti, P. K. Multiferroic Behavior of Lanthanum Orthoferrite ($LaFeO_3$). *Mater. Lett.* **2010**, *64*, 415–418.

(22) May, K. J.; Fenning, D. P.; Ming, T.; Hong, W. T.; Lee, D.; Stoerzinger, K. A.; Biegalski, M. D.; Kolpak, A. M.; Shao-Horn, Y. Thickness-Dependent Photoelectrochemical Water Splitting on Ultrathin $LaFeO_3$ Films Grown on Nb:$SrTiO_3$. *J. Phys. Chem. Lett.* **2015**, *6*, 977.

(23) Nunez, P.; Richter, M. H.; Piercy, B. D.; Roske, C. W.; Cabán-Acevedo, M.; Losego, M. D.; Konezny, S. J.; Fermin, D. J.; Hu, S.; Brunschwig, B. S.; Lewis, N. S. Characterisation of Electronic Transport through Amorphous TiO_2 Produced by Atomic Layer Deposition. *J. Phys. Chem. C* **2019**, *123*, 20116.

(24) Zhang, Q.; Celorrio, V.; Bradley, K.; Eisner, F.; Cherns, D.; Yan, W.; Fermín, D. J. Density of Deep Trap States in Oriented TiO_2 Nanotube Arrays. *J. Phys. Chem. C* **2014**, *118*, 18207.

(25) Celorrio, V.; Calvillo, L.; Granozzi, G.; Russell, A. E.; Fermin, D. J. $AMnO_3$ (A = Sr, La, Ca, Y) Perovskite Oxides as Oxygen Reduction Electrocatalysts. *Top. Catal.* **2018**, *61*, 154–161.

(26) Celorrio, V.; Calvillo, L.; Dann, E.; Granozzi, G.; Aguadero, A.; Kramer, D.; Russell, A. E.; Fermín, D. J. Oxygen Reduction Reaction at $La_xCa_{1-x}MnO_3$ Nanostructures: Interplay between A-Site Segregation and B-Site Valency. *Catal. Sci. Technol.* **2016**, *6*, 7231.

(27) Celorrio, V.; Calvillo, L.; van den Bosch, C. A. M.; Granozzi, G.; Aguadero, A.; Russell, A. E.; Fermín, D. J. Mean Intrinsic Activity of Single Mn Sites at $LaMnO_3$ Nanoparticles Towards the Oxygen Reduction Reaction. *ChemElectroChem* **2018**, *5*, 3044.

(28) Zhao, J.; Bradbury, C. R.; Huclova, S.; Potapova, I.; Carrara, M.; Fermín, D. J. Nanoparticle-Mediated Electron Transfer across Ultrathin Self-Assembled Films. *J. Phys. Chem. B* **2005**, *109*, 22985.

(29) Zhao, J.; Bradbury, C. R.; Fermín, D. J. Long-Range Electronic Communication between

Metal Nanoparticles and Electrode Surfaces Separated by Polyelectrolyte Multilayer Films. *J. Phys. Chem. C* **2008**, *112*, 6832.

(30) Bradbury, C. R.; Zhao, J.; Fermín, D. J. Distance-Independent Charge-Transfer Resistance at Gold Electrodes Modified by Thiol Monolayers and Metal Nanoparticles. *J. Phys. Chem. C* **2008**, *112*, 10153.

(31) Amatore, C.; Savéant, J. M.; Tessier, D. Charge Transfer at Partially Blocked Surfaces. A Model for the Case of Microscopic Active and Inactive Sites. *J. Electroanal. Chem.* **1983**, *147*, 39.

(32) Scafetta, M. D.; Xie, Y. J.; Torres, M.; Spanier, J. E.; May, S. J. Optical Absorption in Epitaxial $La_{1-x}Sr_x FeO_3$ Thin Films. *Appl. Phys. Lett.* **2013**, *102*, 081904.

CHAPTER 4.

Alkaline-earth metal substitution for the enhancement of photoelectrochemical properties in $LaFeO_3$ thin films via promoting active electronic states

Portions of this chapter were published in:

Sun, X.; Tiwari, D.; Fermin, D. J. Promoting Active Electronic States in $LaFeO_3$ Thin-Films Photocathodes via Alkaline-Earth Metal Substitution. ACS Appl. Mater. Interfaces **2020**, 12, 31486−31495.

X.S. prepared all samples and conducted all characterisations reported in this thesis. The SEM and EIS characterisations were performed in collaboration with D.T. The refinement of XRD and the deconvolution of XPS were completed by D.T.

4.1 Abstract

The effects of alkaline-earth metal cation (AMC: Mg^{2+}, Ca^{2+}, Sr^{2+} and Ba^{2+}) substitution on the photoelectrochemical properties of phase-pure $LaFeO_3$ (LFO) thin films are elucidated by X-ray Photoemission Spectroscopy (XPS), X-ray Diffraction (XRD), diffuse reflectance and electrochemical impedance spectroscopy (EIS). XRD confirms the formation of single-phase cubic LFO thin films, with a rather complex dependence on the nature of the AMC and extent of substitution. Interestingly, subtle trends in lattice constant variations observed in XRD are closely correlated with shifts in the binding energies of Fe $2p_{3/2}$ and O 1s orbitals associated with the perovskite lattice. We establish a scaling factor between these two photoemission peaks, unveiling key correlation between Fe oxidation state and Fe-O covalency. Diffuse reflectance shows that optical transitions are little affected by AMC substitution below 10%, which are dominated by a direct bandgap transition close to 2.72 eV. Differential capacitance data obtained from EIS confirm the p-type characteristic of pristine LFO thin films, revealing the presence of sub-bandgap electronic state (A-states) close to the valence band edge. The density of A-states is decreased upon AMC substitution, while the overall capacitance increases (increase in dopant level) and the apparent flat-band potential shifts towards more positive potentials. This behaviour is consistent with the change in the valence band photoemission edge. In addition, capacitance data of cation-substituted films show the emergence of deeper states centred around 0.6 eV above the valence band edge (B-states). Photoelectrochemical responses towards the hydrogen evolution and oxygen reduction reactions in alkaline solutions show a complex dependence on alkaline-earth metal incorporation, reaching incident-photon-to-current conversion efficiency close to 20% in oxygen saturated solutions. We rationalise the photoresponses of the LFO films in terms of the effect sub-bandgap states on majority carrier mobility, charge transfer and recombination kinetics.

4.2 Introduction

4.2.1 The selection of absorber

Lanthanum ferrite exhibits promising PEC properties that has been elaborated in the previous chapter. Although the low EQE is the significant challenge for LFO in the process of PEC water splitting, it can be substantially enhanced by depositing a thin TiO_2 film which acts as a hole-blocking layer at the LFO/water interface in Chapter 3. In addition, after the publication of Chapter 3, various studies such as depositing a thin Au interlayer between the FTO and LFO films,[1] building the C_3N_4/LFO heterostructure,[2] and optimizing preparation methods,[3,4] have been reported to enhance the PEC performance of LFO photocathodes. Those strategies pay attention to the surface modification of LFO for PEC water splitting. This chapter focuses on innovating the bulk properties of LFO thin film via the substitution of alkaline-earth metal cations.

4.2.2 The comparison of different synthesis methods for $LaFeO_3$ photoelectrode

In this chapter, the LFO thin film preparation is also different from previous method. As the widespread investigation of LFO photoelectrodes, there are numbers of preparation methods for $LaFeO_3$ thin films. Basically, they can be divided into two categories, powder-based LFO thin film synthesis and direct LFO thin film preparation. The powder-based LFO photoelectrodes firstly synthesizes LFO particles through various methods (e.g., sol-gel and solid-state reaction), followed by depositing those particles onto FTO-coated glass substrates.[5] Freeman et al. have demonstrated and compared series of strategies for the deposition of LFO nanoparticles.[3] The LFO films in Chapter 3 employs the powder-based LFO photoelectrode synthesis approach through spin-coating nanostructured LFO powders. The grand advantage for powder-based preparation is the highly crystalline

LFO lattice structure due to the permission of relatively high temperature treatment in the preparation of powders, which is beneficial to the achievement of ideal electronic structure and efficient charge carrier transfer at metal oxide photoelectrodes.[6,7] However, the process of the powder deposition onto FTO-coated glass substrates tends to create grain boundaries between particles, increasing electron-hole recombination at the interface of grain boundaries.[8] Moreover, it is difficult to obtain a compact and highly uniform photoelectrodes as shown the corrugated morphology in Figure 3-2c. Those non-repeatability of surface topographies lead to relatively large error bars in PEC characterisations (Figure 3-4c).

In contrast, using direct LFO thin film synthesis method can obtain a repeatable and high quality photoelectrode. But the relatively low calcination temperature that are limited by the stability of FTO-coated glass substrates results in poor crystallizations, especially for oxide-based photoelectrode. The methods for direct LFO thin film preparation include electrodeposition,[9,10] sol-gel synthesis,[11] sputtering deposition,[2,4] etc., indicating various band-gap energies and film morphologies linked to different PEC performances. In this chapter, the direct LFO thin films prepared via sol-gel synthesis is employed, since sol-gel method is much simpler and cheaper than other strategies; more importantly, it can achieve the reproducibility of film thickness and morphological properties, making comparable results between different samples in PEC characterisations.

4.2.3 Current progress of substituted (doped) $LaFeO_3$ photoelectrode

As mentioned in previous chapter, ternary metal oxides, especially for perovskite oxides show flexible tunability of electronic properties, which plays a significant role in PEC behaviour. Atom doping or substitution is an effective approach to tune their composition and structure. It is noted that the difference between the terms ‘‘substitution’’ and ‘‘doping’’ needs to be clarified. In general, most literature employs doping to describe the intentional introduction of a foreign element into a

crystal lattice to tune carrier concentration and conductivity. The phenomenon discussed throughout this chapter is relatively large numbers of foreign elements replace certain cations in LFO photoelectrodes, so ''substitution'' is more appropriate to be used than ''doping'' in the following discussions.

Metal cation substitution (doping) has also been put forward as a potential strategy to improve the photoelectrochemical responses of LFO photocathode. Wheeler et al. reported an increase in photoelectrochemical responses upon 3% K^+ doping at the A-site in LFO, which was primarily linked to changes in the light capture cross-section.[9] Substitution by Mg^{2+} and Zn^{2+} has also shown improvement in photocurrent responses, although it remains to be fully elucidated which sites are being replaced and how these affect the electronic properties of LFO.[11]

In this study, the complex trends in the photoelectrochemical responses of thin LFO films upon alkaline-earth metal cation (AMC: Mg^{2+}, Ca^{2+}, Sr^{2+} and Ba^{2+}) substitution of up to 10% were uncovered. The AMCs are introduced in the sol-gel precursor, keeping the Fe(III) precursor concentration constant. XRD shows a complex dependence of the lattice constant with the type and extent of AMC substitution. Interestingly, the Fe $2p_{3/2}$ and O 1s binding energies extracted from quantitative XPS analysis show a qualitatively similar compositional dependence, revealing a direct correlation between Fe oxidation state and Fe-O covalency. Electrochemical Impedance Spectroscopy (EIS) unveils the presence of sub-bandgap states generated upon AMC substitution, which plays key roles in the kinetics of photoelectrochemical oxygen and water reduction reactions, surface recombination kinetics and dynamics of majority carrier transport.

4.3 Experimental Section

4.3.1 Materials

All the chemical salts, including $La(NO_3)_3 \cdot 6H_2O$, $Fe(NO_3)_3 \cdot 9H_2O$, $Mg(NO_3)_2 \cdot 6H_2O$, $Ca(NO_3)_2 \cdot 4H_2O$, $Sr(NO_3)_2$ and $Ba(NO_3)_2$ have the purity of 99.999%, and were purchased from Sigma-Aldrich company. Citric acid was purchased from Fisher Scientific company. Solvents: ethanol (99.8%), iso-propanol (99.8%), acetone (99.5%) and ethylene glycol (99.5%) were purchased from Sigma-Aldrich company. FTO glass (surface resistivity ~ 7 Ω sq^{-1}) were purchased from Sigma-Aldrich company. Distilled water was produced by Milli-Q systems (18.4 MΩ cm). All materials were used directly without further purification.

4.3.2 The preparation of various thin films

Thin films were deposited using sol-gel methods in the presence of citric acid as a chelating agent.[11,12] $La(NO_3)_3 \cdot 6H_2O$ (0.116 M), $Fe(NO_3)_3 \cdot 9H_2O$ (0.116 M) and citric acid (0.232 M) were dissolved into 4.3 mL water and ethanol (5:4) and stirred for 2 hours, forming a clear solution. Ethylene glycol (0.06 mL) was added into the mixture and further stirred for 20 hours. The solution was spin-coated onto F: doped SnO_2 (FTO) substrates (the purifying of FTO-coated glass substrates, see 3.3.2) with a rotation speed of 3000 rpm for 30 seconds. The film was dried at 100 ^oC for 10 minutes on the hotplate, followed by heating to 400 ^oC for 1 hour. Subsequently, the same procedure was repeated three times to generate thin films with a thickness of approximately 95 nm. The films were finally calcined at 600 ^oC for 3 hours (ramp rate: 5 ^oC min^{-1}). In the case of AMC substituted thin films, the La^{3+} precursor was stoichiometrically substituted with either $Mg(NO_3)_2 \cdot 6H_2O$, $Ca(NO_3)_2 \cdot 4H_2O$, $Sr(NO_3)_2$ and $Ba(NO_3)_2$, keeping the concentration of Fe precursor and citric acid constant (La precursor substitution).

4.4 Results and discussion

4.4.1 XRD characterisation of various $LaFeO_3$ based thin films

Figure 4-1 illustrates XRD patterns of pristine and AMC substituted LFO thin films deposited onto glass. Figure 4-1a contrasts the pristine and 3% Ba^{2+} substituted LFO films, exhibiting the phase pure pattern associated with the pm-3m cubic phase (the JCPDS-ICDD database file No. 01-075-0541). Figure 4-1b focuses on the position of the (110) diffraction peak for 7% substituted LFO, revealing that the extent of lattice

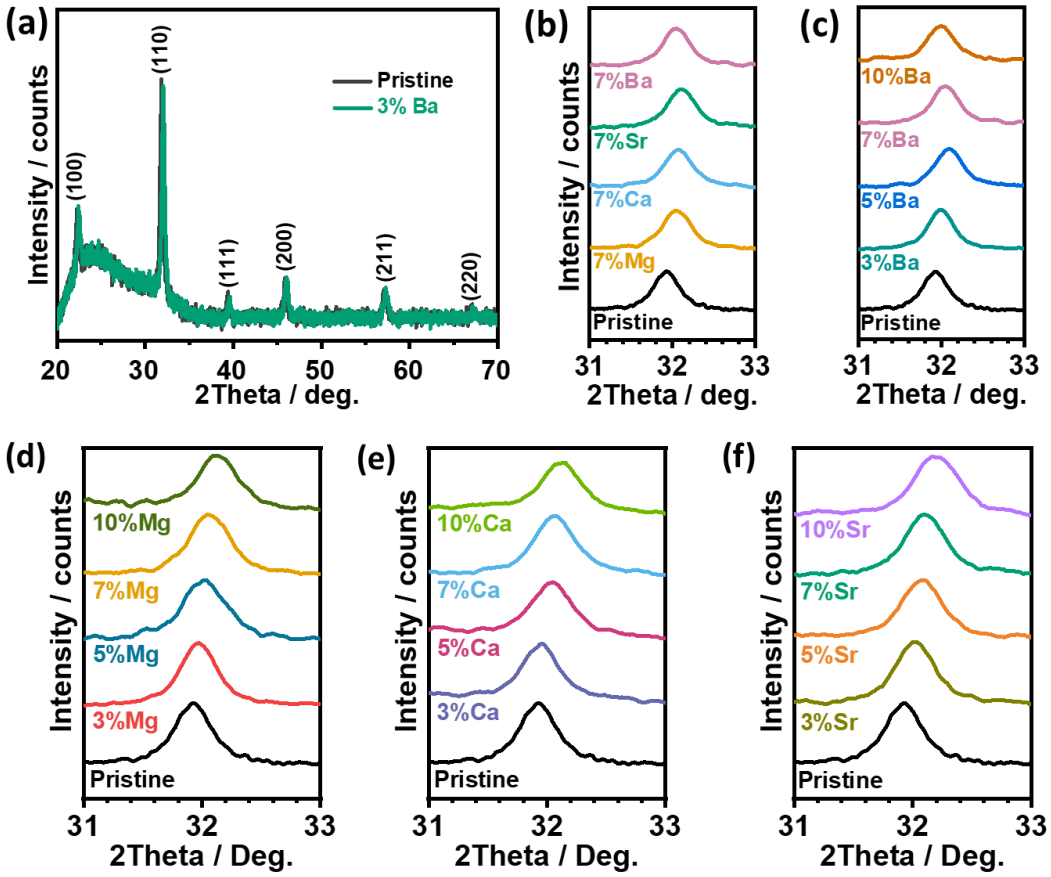

Figure 4-1 XRD of alkaline-earth metal cation (AMC) substituted $LaFeO_3$ (LFO) thin films: XRD patterns of pristine and 3% Ba^{2+} substituted LFO thin films (a), showing the key features associated with the pm-3m cubic phase. Evolution of the (110) peak upon 7% substitution of the various AMC (b) and as a function of the extent of Ba^{2+} (c), Mg^{2+} (d), Ca^{2+}(e), and Sr^{2+}(f) substitution.

distortion depends on the nature of AMC. The complex dependence of the diffraction angle with the extent of Ba^{2+} substitution is illustrated in Figure 4-1c, where an initial shift toward slightly higher 2θ values is then reversed to values closer to the pristine LFO. In contrast, the XRD patterns of the rest three cations (Mg^{2+}, Ca^{2+} and Sr^{2+}) display a monotonic shift toward higher 2θ values in figure 4-1d-f. This phenomenon will be further discussed below, primarily due to the different ionic radius among AMC.

The evolution of the structural parameters upon AMC substitution were investigated by Pawley refinement of the XRD pattern as described in Figure 4-2a. The XRD patterns of the pristine LFO and 7% AMC substituted films refined to the JCPDS-ICDD database file 01-075-0541, further confirming the phase purity of the thin films. More importantly, the analysis shows a decrease in the lattice constant by approximately 2 pm upon 7% AMC substitution in Figure 4-2b. Despite the flat difference curve, the refinement could not converge below Rp and Rwp of 18% and 23%, respectively. The uncertainty in the refinement arises from the scatter in the experimental XRD and nanoscale crystalline domain of the thin films (less than 100 nm). Therefore, it should be noted that although the trend is clear and unambiguous, the absolute values of the estimated lattice parameters should be considered cautiously. Figure 4-2b shows an interesting trend considering, for example, that the lattice constant of the cubic $BaFeO_3$ is reported as 3.971 Å.[13] We rationalise this behaviour in terms of the promotion of higher Fe oxidation states, which feature smaller ionic radius, as a result of charge compensation upon La^{3+} substitution by the divalent AMC. Although Ba^{2+} have larger ionic radius than La^{3+}, the net change in the unit-cell size is dominated by the decrease in the Fe ionic radius at this low substitution levels. The trend in Figure 4-2c shows that as Ba^{2+} substitution increases over 5%, the shrinking in lattice constant induced by the higher oxidation state in the B-site is partially compensated by the larger A-site cation. On the other hand, Mg^{2+},

Ca^{2+} and Sr^{2+} cations have a similar or smaller ionic radius, compared with La^{3+}, leading to the monotonic change (decrease) of lattice constant in Figure 4-2c. Although the behaviour observed in the XRD upon AMC substitution is highly reproducible, comparison with previous studies should be considered cautiously. Aspects such as nanocrystalline domain size, temperature and substrate induce strain can all play a role in the trends observed.

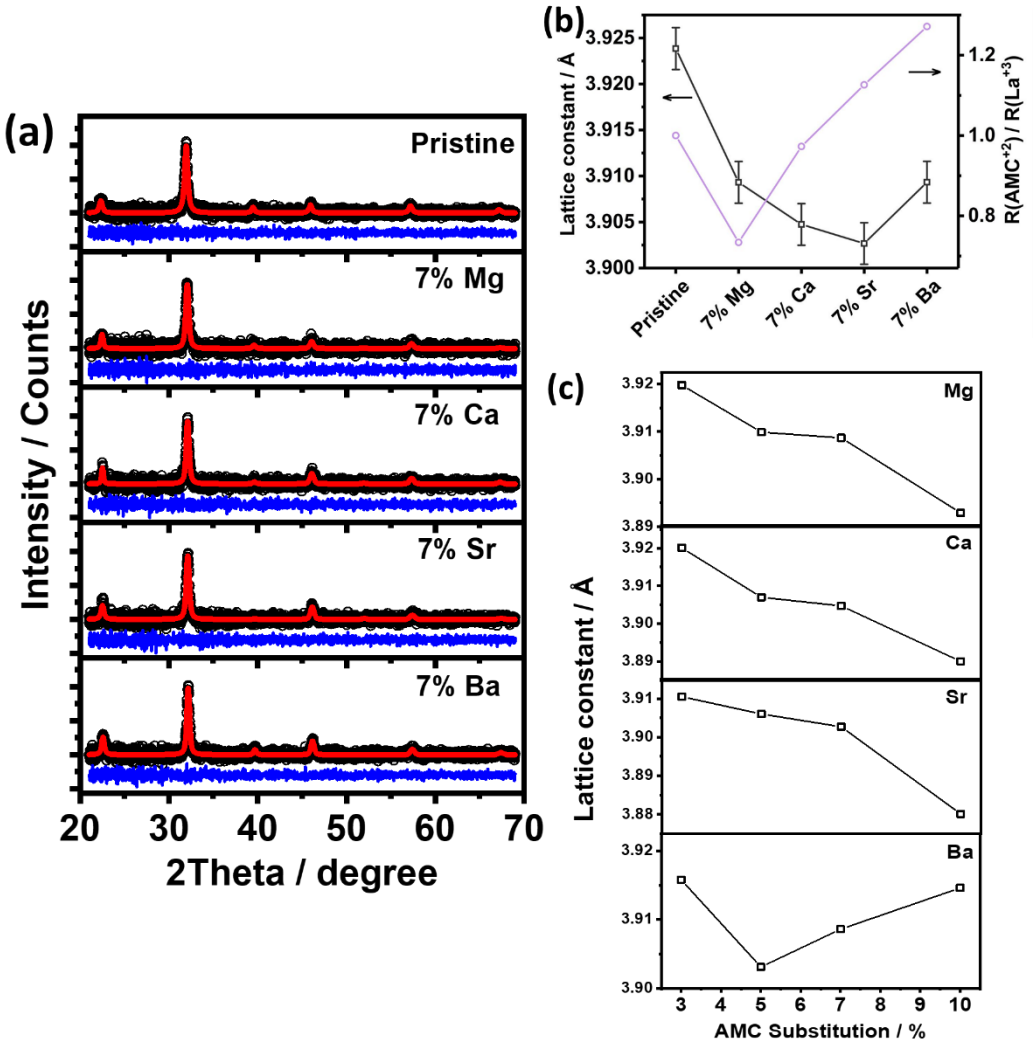

Figure 4-2 XRD patterns of the pristine and 7% AMC substituted LFO refined to the pm-3m cubic phase JCPDS-ICDD database file 01-075-0541 (a). The bule line represents the difference between observed (black) and calculated (red) XRD patterns. Lattice constant of substitution of the various AMC (b) and as a function of the extent of Mg^{2+}, Ca^{2+}, Sr^{2+} and Ba^{2+} substitution (c) extracted from full-profile structural Pawley refinement. The ionic radius ratio of AMC to La^{3+} (b).

4.4.2 Morphology characterisation of various $LaFeO_3$ based thin films

Figure 4-3a compares the SEM topographies of pristine and various AMC substituted thin films, indicating that no specific morphological feature was observed

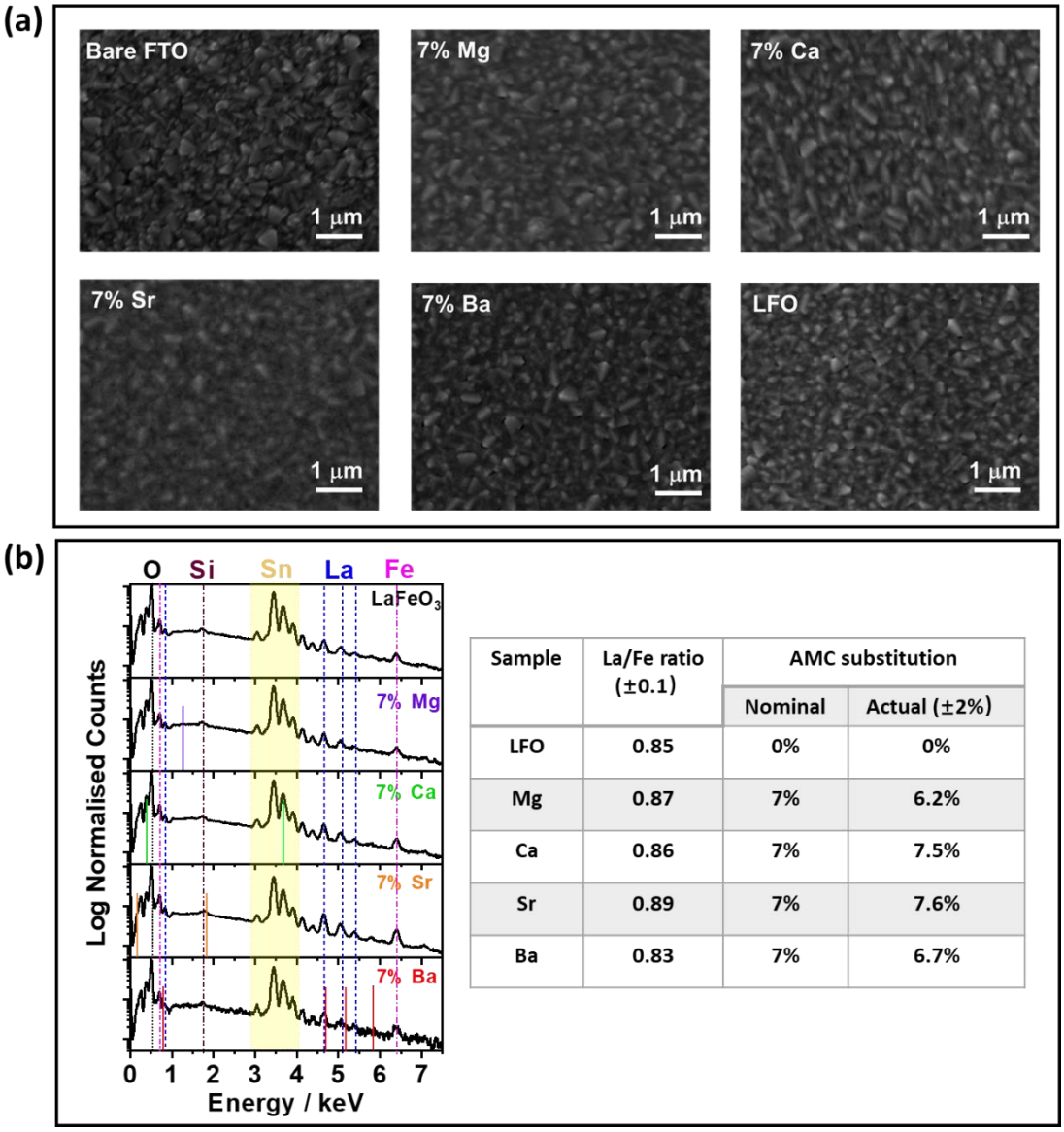

Sample	La/Fe ratio (±0.1)	AMC substitution	
		Nominal	Actual (±2%)
LFO	0.85	0%	0%
Mg	0.87	7%	6.2%
Ca	0.86	7%	7.5%
Sr	0.89	7%	7.6%
Ba	0.83	7%	6.7%

Figure 4-3 Top view scanning electron micrographs (SEM) of bare FTO-coated glass substrate and LFO-based thin films (a). Energy dispersive analysis of X-rays (EDX) spectra of pristine and AMC substituted LFO thin films (b).

after AMC substitution. Figure 4-3a also displays that the bare FTO-coated glass substrate has a rough surface with grain sizes in the region from ten to hundreds of nanometers, while the surface morphologies become relatively smooth after entirely coating the thin films. The shape of the FTO grains still can be seen in the SEM images of the thin films due to the extreme thin thickness of those films (95 nm). Although EDX analysis confirms that the AMC content in the films is very close to the composition in the sol-gel precursor, the values of actual AMC substitution shown in Figure 4-3b should be considered cautiously. On the one hand, there is a relatively large error bar (±2%) on measured values. On the other hand, those values are influenced by FTO-coated glass substrate or surface contamination that contains the same elements (e.g., Ca) as AMC. Similarly, the La/Fe ratios of AMC substituted LFO thin films are similar to the pristine one, which is also affected by the instrument error to some extent. Furthermore, AMC, especially for Mg^{2+}, tends to occupy both A- and B-site of perovskite lattice, leading to the constant value of La/Fe ratio upon AMC substitution, though the fact that Ca^{2+}, Sr^{2+} and Ba^{2+} substitute A-site (La^{3+}) of the perovskite lattice is widely recognized.[17,20,30]

4.4.3 XPS analysis of various photocathode constructs

The survey high-resolution X-ray photoelectron spectroscopy (XPS) was acquired from various LFO-based thin films deposited on FTO-coated glass substrate, displaying relevant photoelectron peaks for lanthanum (La 4d, La 4p and La 3d), iron (Fe 3p and Fe 2p) and oxygen (O 1s) in Figure 4-4. The C 1s peak assumed at 284.8 eV was used to do the charge-correction. It can be seen that there are certain unlabeled small signals that belong to AMC, except for Auger lines. However, these peaks from AMC are not reliable because of low-cross section and impurities from FTO substrate or surface contamination (e.g., Ca $2p_{3/2}$ at 347 eV).

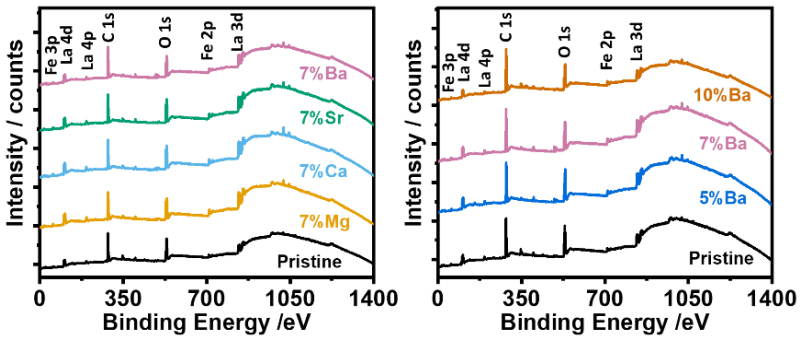

Figure 4-4 X-ray photoelectron spectroscopy for the survey of pristine and AMC substituted LFO thin films: 7% substitution of the various AMC (left) and as a function of the extent of Ba^{2+} (right).

Semi-quantitative XPS analysis was carried out across the whole range of AMC substituted LFO thin films, with representative deconvolutions of the La 3d, Fe 2p and O 1s photoemission bands shown in Figure 4-5. The La 3d region contains two photoemission peaks with binding energies (BE) at 833.9 and 850.9 eV associated with La $3d_{5/2}$ and La $3d_{3/2}$, respectively.[14–16] These peak positions confirm the La^{3+} oxidation state, which is also supported by the 17 eV spin-orbit component separation between the doublet. Three different components were presented in the deconvolution of the O 1s peak, with the lowest BE (529.2 eV) linked to oxygen in the perovskite lattice, and the other two components assigned to hydroxyl group and carbonated species.[15] The predominant Fe^{3+} oxidation state can be described by the peak positions of Fe $2p_{3/2}$ at around 709.6-710.6 eV and Fe $2p_{1/2}$ at 722.8-724.2 eV, with a spin-orbit splitting of around 13.6 eV and satellite peaks at approximately +8.6 eV from each doublet. The deconvolution of the broad Fe 2p photoemission is not straightforward given the complexity introduced by multiple-splitting, multiple oxidation states and charge transfer effects.[17–19] In this study, we have implemented a simple approximation based on previous photoemission studies of Fe oxides, supported by highly sensitive Mossbauer spectroscopy.[20,21] The Fe 2p peak can be deconvoluted into three components, with the most prominent being assigned to Fe^{3+} species. The smaller peaks at higher binding energies correspond to higher iron

oxidation states, with some studies linking these features to Fe^{4+},[9,20–23] although this would require systematic analysis of other Fe core levels.[24]

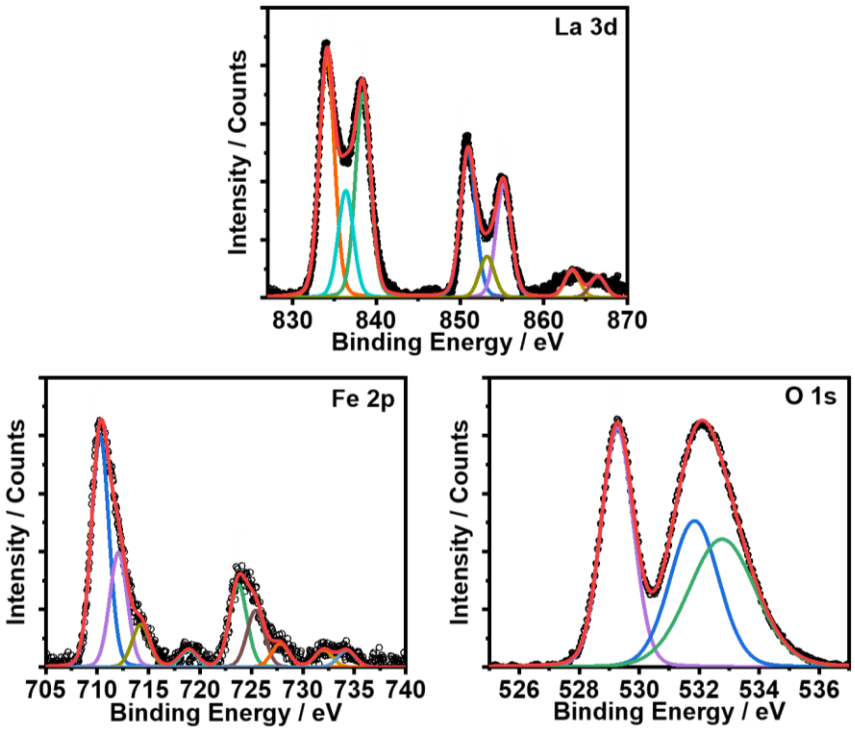

Figure 4-5 Deconvolution of La 3d, Fe 2p, O 1s XPS bands of 7% Sr substituted LFO thin film. All constructs show a similar deconvolution pattern.

Figure 4-6 displays the dependence of the binding energies of Fe $2p_{3/2}$ and O 1s orbitals associated with the perovskite lattice as a function of AMC substitution (7%), as well as various Ba^{2+} substitution levels. La 3d has absolutely no role in affecting the chemical state of active elements found close to valence band edge in LFO thin films. As reported by Wheeler et al.,[9] according to the DFT calculation of band composition, the contribution of lanthanum to the valence band edges of LFO is negligible. The BEs of Fe $2p_{3/2}$ and O 1s show similar nonmonotonic trends to those observed in the (110) XRD peak upon AMC substitution (Figure 4-1). This remarkable observation suggests that the interplay between changes in Fe site oxidation state and lattice distortion introduced by the AMC substitution affects the surface electronic structure of the thin film. The research target of this chapter is to

investigate the effect of electronic structure changes on PEC performance, so that the binding energies of oxygen in the perovskite lattice (528.5-529.6 eV) is mainly studied. We also noticed that the higher BE components of the O 1s appear to be affected by AMC substitution in Figure 4-6b and d. We rationalise this observation as variations in the relative intensity of the hydroxyl and carbonated photo-emission responses, as opposed to shifts in the binding energy.

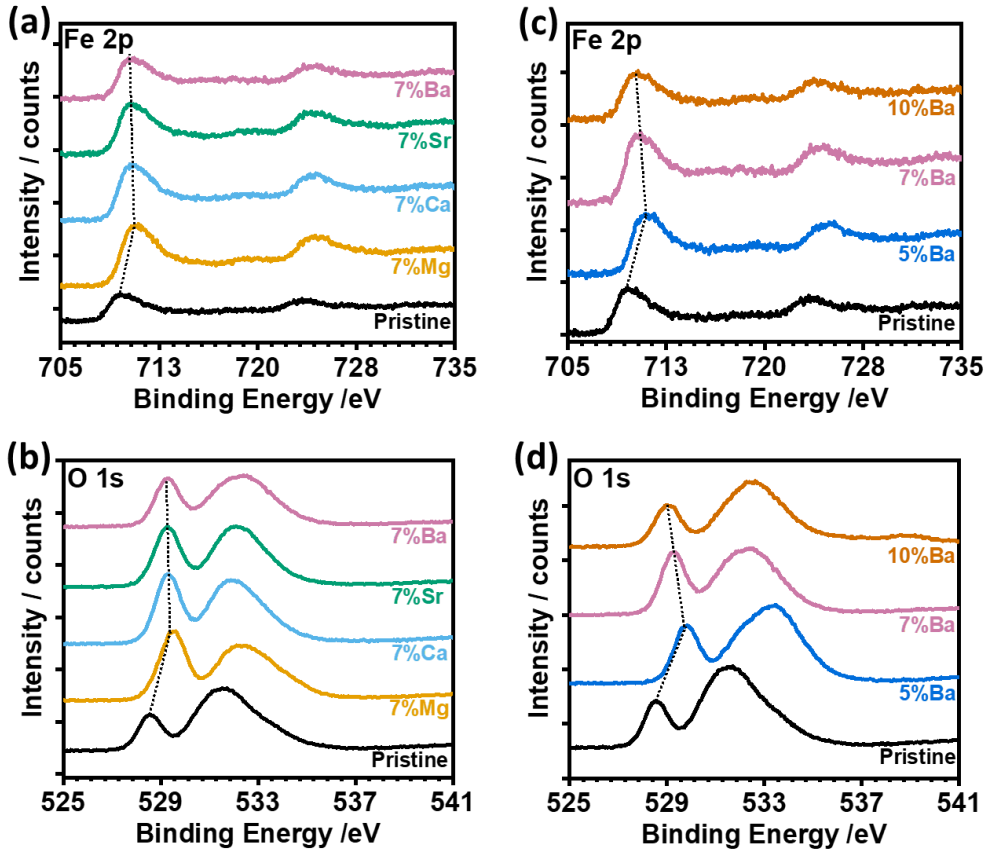

Figure 4-6 Evolution of the XPS spectra in the regions of Fe 2p (a,c) and O 1s (b,d) upon 7% AMC substitution and extent of Ba^{2+} substitution. The dashed lines show the shift of binding energies upon substitution.

The scaling relation between Fe oxidation state and bond covalency is displayed by the linear correlation between Fe $2p_{3/2}$ and O 1s binding energies in Figure 4-7. No such correlation is observed between O 1s and La 3d. This trend shows that the increase in the oxidation state of Fe sites promoted by AMC substitution manifests itself by a shift of the Fe $2p_{3/2}$ peak towards higher BE, a subtle decrease in the

perovskite lattice constant and an increase in the degree of covalency, which in turns drives the O 1s binding energy towards higher values. The correlation between XRD and XPS data in thin films demonstrates that AMC are present in the crystal lattice, promoting an increase in the Fe oxidation state. Should the AMC be sitting in grain boundaries, then changes in the structural and electronic state would be less pronounced. The thin film nature of our material, as well as the processing temperatures used, may also play a role in the trends observed, although Shen et al.[25] have also postulated that Fe^{4+} sites can lead to a stronger Fe-O bond.

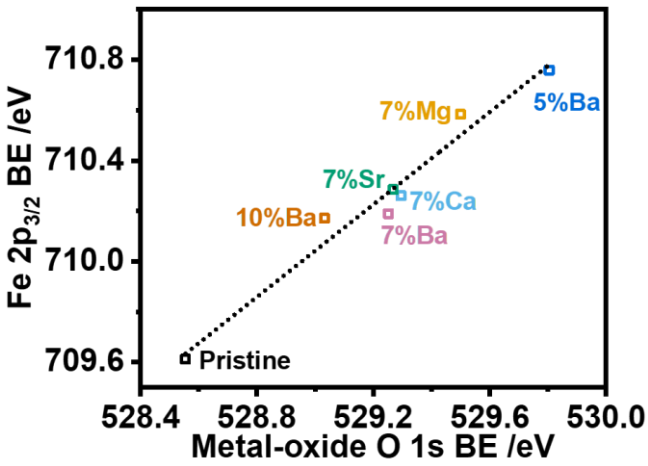

Figure 4-7 Correlation between binding energies (BEs) of Fe $2p_{3/2}$ and O 1s (perovskite lattice) in pristine and AMC substituted LFO films. This trend strongly suggests that Fe oxidation state and covalency of the Fe-O bond are strongly correlated.

4.4.4 Optical properties of pristine and 7% AMC substituted LFO thin films

Diffuse reflectance spectra shown in Figure 4-8a reveal that AMC substitution up to 7% has minimal effect in the optical properties of LFO. The data clearly shows that AMC substitution, in the concentration range investigated, have little influence on the optical properties of the thin film. Furthermore, the virtually identical values demonstrate the reproducibility of our deposition method in terms of thickness and film morphology, which strongly affect the film optical parameters. Tauc plots in Figure 4-8b shows the optical bandgap energy of pristine and all AMC substituted

films are all close to 2.72 eV. LFO shows a clear sub-bandgap transition which does not generate free charge carriers, as explained in Chapter 3. It should be mentioned that Wheeler et al. reported more substantial changes in the optical properties upon 3% K^+ substitution.[9] We have also observed spectral changes at AMC substituted LFO powders processed at temperatures above 800 °C.

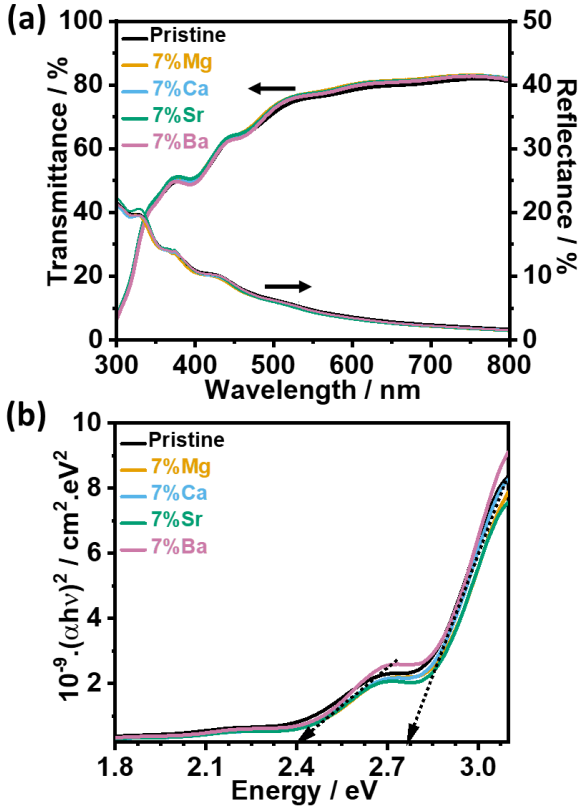

Figure 4-8 Optical properties of 95 nm pristine and 7% AMC substituted LFO thin films: (a) transmittance and reflectance spectra in the visible range and (b) Tauc plots showing the main absorption edge at 2.72 eV. Dashed arrows show the linear fit of pristine film, indicating two clear distinctive transitions.

4.4.5 Electrochemical characterisation of various constructs

Cyclic voltammograms of pristine and 7% AMC substituted LFO films in 0.1 M Na_2SO_4 pH 12 in the dark are displayed in Figure 4-9a. The voltammograms, recorded at 100 mV s^{-1}, show an increase in the capacitive current in the range of +0.4 to +1.5 V vs RHE with respect to the pristine LFO thin film. The onset of oxygen evolution can be seen at potentials beyond +1.4 V, indicating the transition from reverse to

forward bias. A broad pseudo-capacitive feature can be seen at potentials around +1.3 V in the case of pristine LFO while a more significant response can be seen at less positive potential upon 7% AMC substitution. Figure 4-9b shows that the pseudo-capacitive response between +0.8 and +1.0 V increases upon the increasing concentration of Ba^{2+} in the film. Plots of differential capacitance as a function of the

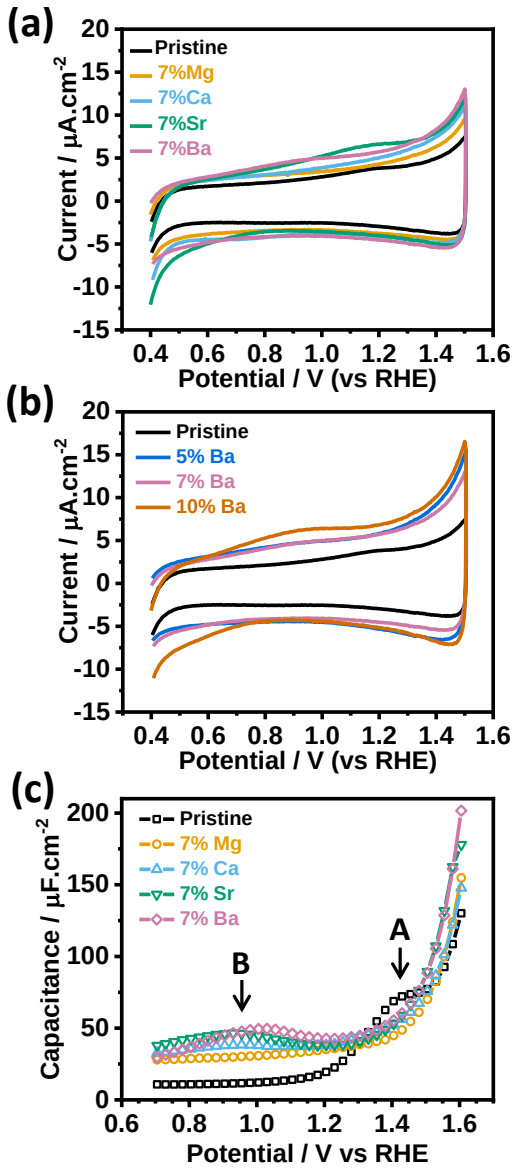

Figure 4-9 Electrochemical responses in 0.1 M Na_2SO_4 pH 12: (a) cyclic voltammograms of pristine and 7% AMC substituted LFO films at 0.1 V s^{-1}; (b) cyclic voltammograms as a function of the Ba^{2+} substitution extent at 0.1 V s^{-1}; and (c) Capacitance voltage curves extracted from electrochemical impedance spectra of pristine and 7% AMC substituted films, highlighting the pseudo-capacitive elements associated with A and B sub-bandgap states.

applied potential in Figure 4-9c further emphasise the trends observed in cyclic voltammetry. Each capacitance point shown in Figure 4-9c was calculated from electrochemical impedance spectra as described in Experimental Section. Indeed, AMC substitution promotes a significant increase in the capacitance across the whole potential range, suggesting a significant increase in the density of acceptor states (doping density). We also see an increase in the capacitance of the pristine LFO thin film from 1.2 eV and a prominent shoulder at 1.4 eV, which are linked to sub-bandgap surface states (A-states). The transition from reverse to forward bias in the AMC substituted films occurs about 0.2 V more positive than in the pristine LFO films, with a broad pseudo-capacitive feature in the range of 0.8 to 1.1 eV (B-states) depending on the AMC. The data in Figure 4-9 clearly show that the density of B-states depends on the extent of AMC substitution, while A-states appears to dampen by all AMC substantially.

Based on the link between the emergence of B-states and AMC substitution, these states are likely to involve a combination of Fe 3d and O 1s states as a result of the presence of higher Fe oxidation states.[9,26] On the other hand, A-states are linked to intrinsic defects which tend to generate states closer to the valence band edge. Indeed, Taylor et al., concluded that Schottky disorder compensated by cation vacancies could generate intrinsic sub-bandgap states near the valence band.[27] In principle, the position of these states probed by electrochemical methods can be strongly influenced by the hydration energy.[28] Consequently, we could have a rather complex picture in which these states may have different energies in bulk and at the surface. Further below, we will demonstrate that these states have a strong effect on the photoelectrochemical responses of LFO films.

4.4.6 Mott-Schottky plots and valence band edges of various thin films

Mott-Schottky plots of the pristine, 7% AMC and 17% Mg^{2+} substituted LFO thin films are displayed in Figures 4-10. As introduced in Chapter 1, the A- and B-states can cause a change in the band bending due to the discharging of these states. However, at semiconductor-liquid junctions, the Mott-Schottky equation (see Chapter 3) reveals the relationship between the capacitance linked to the extent of band bending and the applied potentials. In the absence of density of states, the dependence of capacitance and potential enables the Mott-Schottky to be linearly fitted to show some information related to semiconductor (e.g., flat band potential). The presence of A- and B-states introduces significant complexity and uncertainty in the analysis of these plots. From the linear segment of the pristine LFO plot, the p-type semiconductor behavior and a flat band potential (U_{fb}) of +1.32 (±0.01) V vs RHE can be determined, although this value would be affected by Fermi-level pinning (FLP) induced by the A-states (Figure 4-10a). On the other hand, FLP at B-states substantially distorts the Mott-Schottky plots up to +1.2 V. Extrapolating from this potential onwards; Figure 4-10b suggests a U_{fb} = +1.58 V vs RHE regardless of the type and extent of AMC substitution. It should be noted that the fit of Mott-Schottky plot in Figure 4-10b employs the data of 7% Sr^{2+} substituted LFO thin film. The U_{fb} of the other three AMC (the fitting is not shown) display similar values to 7% Sr^{2+} substitution, with a difference of only ±0.02 V. 7% Mg^{2+} substituted LFO thin film shows less FLP than other AMC (Figure 4-9c and Figure 4-10b), but it is clear to see the FLP when the substitution increases up to 17% in Figure 4-10c. The slightly different performance of Mg^{2+} substitution will be further explored in the following discussion.

Based on the Mott-Schottky equation (shown in Chapter 3), the majority carrier density can also be estimated from the data in Figure 4-10. However, quantification

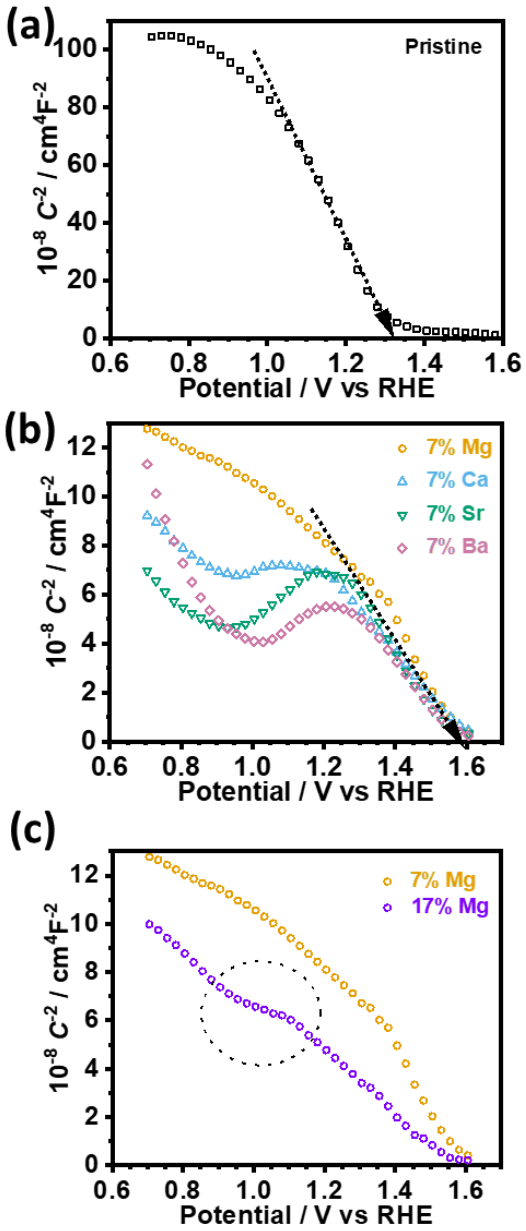

Figure 4-10 Mott-Schottky plots of LFO based thin films in 0.1 M Na_2SO_4 aqueous solutions at *pH 12: (a) pristine, (b) 7% AMC substitution and (c) 17% Mg^{2+} substitution. Dashed arrows show the fit of the Mott-Schottky plots. The linear fitting in (b) employs the data of the 7% Sr^{2+} substituted LFO thin film.*

of the majority carrier density is rather complex due to the FLP induced by the surface states and the acute dependence of the relative permittivity on parameters such as grain size and annealing temperature.[29] A rough estimation based on the linear portions highlighted in Figure 4-10a and b, suggests that pristine LFO would be in the range of 2.3×10^{17} cm^{-3}. At the same time, if the relative permittivity of AMC

substituted LFO is assumed to be the same as that of pristine LFO, AMC substituted LFO thin films in the range investigated are approximately 10 times larger. This observation is also consistent with the strong dependence of LFO conductivity on the extent of Sr^{2+} substitution reported by Shen et al.[25]

Figure 4-11 contrasts the valence band edges of the LFO films (pristine and 7% AMC substituted) estimated from XPS spectra. The valence band onset of the pristine and Sr^{2+} substituted LFO film with reference to Fermi level is 0.53 eV and 0.85 eV, respectively, as shown in Figure 4-11. Although there is an approximately 300 meV shift of the valence band edge in Sr^{2+} substituted LFO with respect to the pristine film, the actual valence band offset between them cannot be estimated in Figure 4-11 due to the change of Fermi level upon substitution (doping). With regards to the other AMC substitution, the valence band edges with reference to Fermi level are in the region between 0.63 eV to 1.12 eV. It should be pointed out that those values mentioned above show large error bars of around ± 100 meV. As the sub-bandgap states are close to valence band edge, they tend to have a significant effect on the shape of valence band edge. Unfortunately, they are not well resolved in energy owing to the small cross-section of these states under the X-ray excitation used. This leads to a complex or unreliable valence band edge determination to some extent. Thus, the valence band edges observed in Figure 4-11 should be considered with caution. However, Figure 4-11 clearly shows a sharper increase in photoemission intensity at the valence band edge of the AMC substituted with respect to the pristine film. Based on the Fermi-Dirac Distribution, this trend suggests an increase in acceptor states (conductivity) upon AMC substitution.

Similarly, the valence band spectrum of the pristine LFO appears to show a higher density of states at Fermi level, which can also be linked to the A-states that are not well resolved due to its small cross-section of A-states. Thus, a consistent picture of

the density of states near the valence band edge is emerging from the differential capacitance-voltage curve (Figure 4-8c) and the valence band spectra (Figure 4-10).

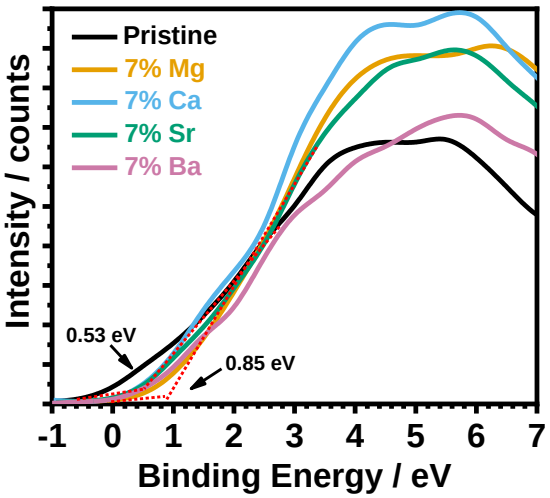

Figure 4-11 Valence band edge calculated from XPS analysis of the pristine and 7% AMC substituted films. The valence band edge of pristine and 7% Sr^{2+} substituted LFO is 0.53 eV and 0.85 eV with reference to Fermi level, respectively.

4.4.7 PEC characterisation of pristine and AMC substituted $LaFeO_3$ thin films

Linear sweep voltammograms (LSV) of various 7% AMC substituted LFO photocathodes (Figure 4-12a) and as a function various AMC content (Figure 4-12b-f) were recorded at 5 mV s^{-1} in O_2-saturated 0.1M Na_2SO_4 aqueous solution at pH 12, under a square wave 405 nm light perturbation and a photon flux of 3.25×10^{15} cm^{-2} s^{-1}. The photocurrent responses for all AMC substituted films are significantly higher than that for pristine LFO, with all showing a similar photocurrent-voltage dependence and an onset potential close to +1.2 V vs RHE. In order to directly compare the photocurrent responses as a function of the type and extent of AMC substitution, the photocurrent density of various AMC substituted LFO thin films at +0.45 V vs RHE were selected from Figure 4-12b-f and integrated into Figure 4-12g. Interestingly, it can be seen that the photocurrent response as a function of the Ba^{2+} content goes through a maximum at around 7%. A similar trend is observed for Ca^{2+}

and Sr^{2+} substituted LFO thin films, except Mg^{2+}. The photocurrents of Mg^{2+} substituted LFO photocathodes (La^{3+} was replaced by AMC, La precursor substitution) display a continuous increase in Figure 4-12g.

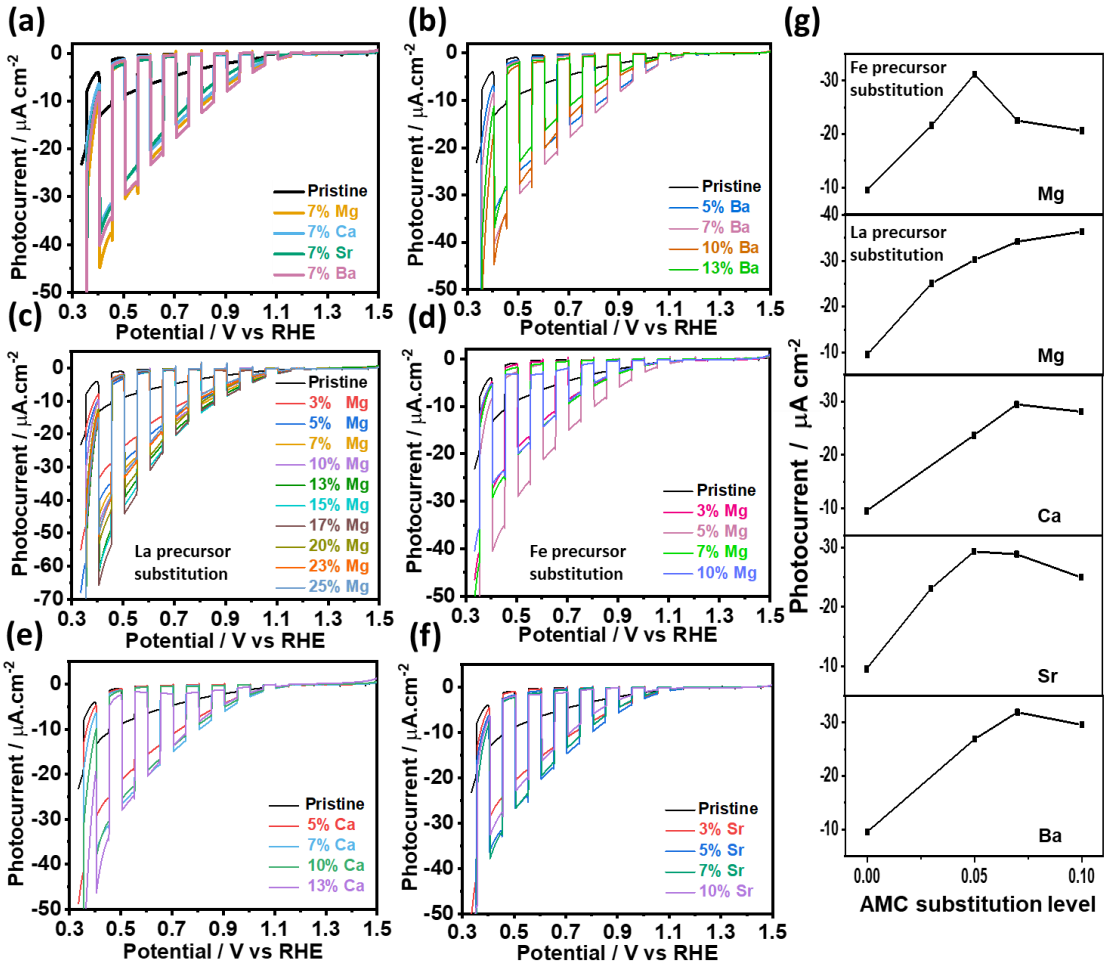

Figure 4-12 Photoelectrochemical responses in O_2-saturated 0.1M Na_2SO_4 aqueous solution pH 12: (a-f) 5 mV s^{-1} linear sweep voltammetry of pristine and AMC substituted LFO thin films under a square wave 405 nm light perturbation and photon flux of 3.25×10^{15} cm^{-2} s^{-1}; and (g) photocurrent response at +0.45 V vs RHE as a function of the type and extent of AMC substitution.

Indeed, Figure 4-12c shows a weak increase upon increasing Mg^{2+} substitution up to 17%. We rationalise this behaviour in terms of the affinity of Mg^{2+} to the B-site of the perovskite lattice as predicted by Taylor et al.[30] Diez-Garcia and Gomez have also reported the photocurrent enhancement in the presence of Mg^{2+}, although they only assume B-site substitution, which is not entirely supported by our XPS

observations.[11] We compared the photocurrent responses of Mg^{2+} substituted LFO thin films in terms of different sites substitution. The synthesis of Mg^{2+} substituted LFO thin films shown in Figure 4-12c followed the procedure described in Experimental Section, while the Fe^{3+} precursor was stoichiometrically substituted with $Mg(NO_3)_2 \cdot 6H_2O$ salts (Fe precursor substitution) for those samples shown in Figure 4-12d. Keeping B-site constant (Figure 4-12c) is beneficial to the PEC performance, with the photocurrents of nearly two times higher than that of Fe precursor substitution (Figure 4-12d). It should be noted that the Mg^{2+} cations will finally trigger the formation of Fe(IV) species to enhance the photoelectrochemical behaviour of LFO thin films, wherever it goes A-site and / or B-site. However, as elaborated in structure and EIS analysis, the change of majority carrier density and defect states linked to PEC performance in LFO thin films are mainly due to iron and AMC, while lanthanum plays a less significant role. Therefore, the B-site (Fe) precursor substitution tends to reduce the photoactive sites, leading to a decrease of photocurrent responses in comparison with A-site (La) precursor substitution.

Figures 4-13a shows the external quantum efficiency (EQE) spectra of the pristine and 7% AMC substituted films in O_2-saturated 0.1M Na_2SO_4 aqueous solutions at pH 12. EQE values closed to 20% are obtained in the case of 7% Ba^{2+} substituted at a wavelength close to 360 nm and potential bias of +0.45 V vs RHE, which is one of the highest EQE value reported for LFO photocathodes. Integrating the EQE spectral response of 7% Ba^{2+} substituted LFO thin film provides photocurrent responses up to -0.22 mA cm^{-2} under AM 1.5 illumination at +0.45 V vs RHE. Tauc plots constructed from EQE data (Figure 4-13b) clearly demonstrate that charge carriers are only generated upon excitation above 2.72 (±0.02) eV, which we have identified as the effective bandgap of the material (Figure 4-8b). The AMC substitution has a little effect on bandgap energy, for example, the bandgap estimated from EQE data remains the same energy (2.72 eV) upon 7% Mg^{2+} substitution. Although 7% Sr^{2+}

substituted LFO thin film with a bandgap energy of 2.74 eV displays an increase in bandgap, such a slight change is also within the fitting error. This observation is in contrast with the Wheeler et al., study, which concluded that photocurrent enhancement upon K^+ substitution is linked to a decrease in the bandgap.[9]

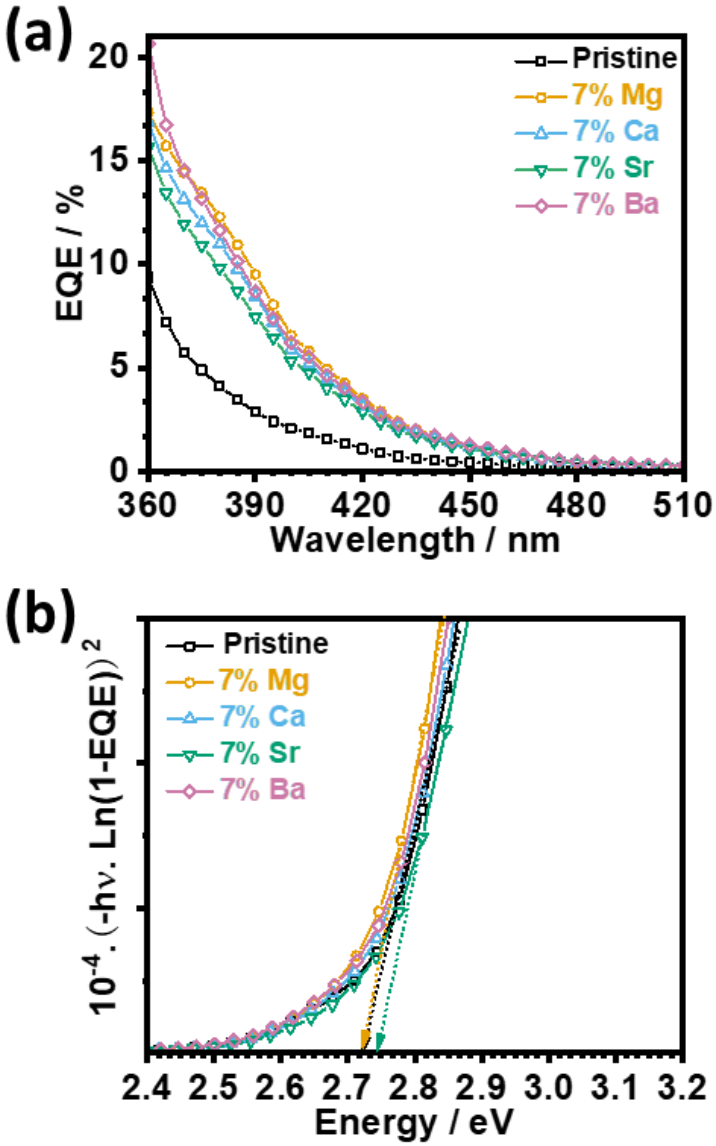

Figure 4-13 External quantum efficiency spectra for the pristine and 7% AMC substituted thin films (a); and Tauc plot representation of the EQE (b). Dashed arrows show the linear fit of pristine (black), Mg^{2+} substituted (yellow) and Sr^{2+} substituted (green) LFO, demonstrating that charge carriers are generated only above the 2.72 (±0.02) eV edge.

To rationalise the photocurrent enhancement mechanism, we explore the behaviour in Ar-saturated solution as displayed in Figure 4-14. LSV curves for pristine

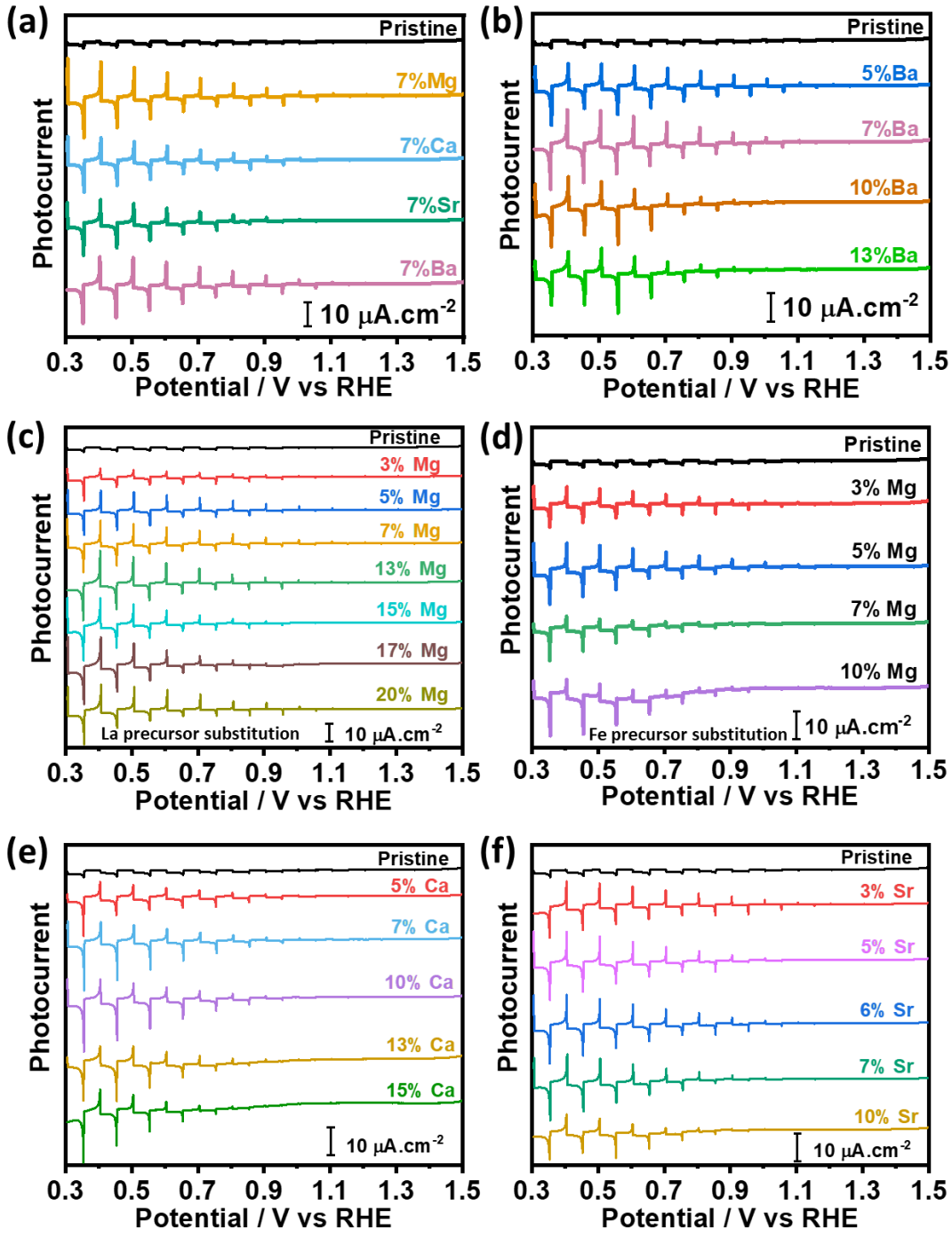

Figure 4-14 Linear sweep voltammetry (LSV) of pristine and AMC substituted LFO thin films in Ar-saturated 0.1M Na_2SO_4 aqueous solution pH 12: (a) 7% AMC substitution; and (b-f) different extents of AMC substitution. LSV were recorded at 5 mV s^{-1} and under square wave light perturbation (405 nm and 3.25×10^{15} cm^{-2} s^{-1} photon flux).

and all AMC substituted LFO thin films in Figure 4-14 were recorded under the same conditions as in Figure 4-12 after purging the solution with Ar for over 30 min. In all cases, a significant improvement in the magnitude of the photoresponses is observed, although there is clear evidence of fast surface recombination. Indeed, there is a sharp increase in the initial photocurrent (displacement current) followed by a substantial relaxation to a low quasi-stationary photocurrent. The off-transient is a positive photocurrent overshot and a relaxation with a similar time constant. (The transient photocurrent responses as a function of time will be discussed in detail later.) This behaviour is somewhat different from those observed in pristine highly crystalline LFO nanoparticle thin films, which are characterised by a highly asymmetric photocurrent transient responses associated with hindered majority carrier transfer rather than surface recombination, as demonstrated in the Chapter 3 and by Celorrio et al.[5] Consequently, AMC substitution has a strong effect on carrier mobility leading to high displacement current, but also promotes surface carrier recombination in Ar-saturated solution.

4.4.8 The role of sub-bandgap states in photoelectrochemical responses

In order to schematically illustrate the effect of AMC substitution in electronic states near the valence band (VB), the visualization of A- and B-states for pristine and AMC substituted LFO thin films is shown in Figure 4-15. The band diagram was constructed using flat band potential estimated from Mott-Schottky plots (Figure 4-10) and bandgap energy calculated from Tauc plots (Figure 4-8). To be specific, as illustrated by Cardon and Gomes,[31] the energy difference between flat band potential estimated from Mott-Schottky plot and valence band edge of p-type semiconductor (conduction band edge of n-type semiconductor) is within 0.1 eV; therefore, the flat band is used to indicate the position of valence band edges in Figure 4-15. Under the premise that the position of the valence band edges is known,

the position of the conduction band edges can be determined by the bandgap. Since the density of states is directly proportional to capacitance, the relative density of A- and B-states shown in Figure 4-15 is obtained from the EIS data (Figure 4-9c). It should be pointed out that the band diagram can also be created based on the VB XPS spectrum, bandgap energy and work function, which is a more reliable method. Specifically, the position of valence band edges with reference to Fermi level can be directly estimated from VB XPS spectrum, as shown in Figure 4-11. If the work function of a semiconductor can be obtained, its Fermi level is thereby determined with respect to the vacuum level. In this case, the band alignment of the semiconductor can be constructed once the bandgap is known. However, it is difficult to obtain the work function of LFO-based thin films, as their conductivity is not good.

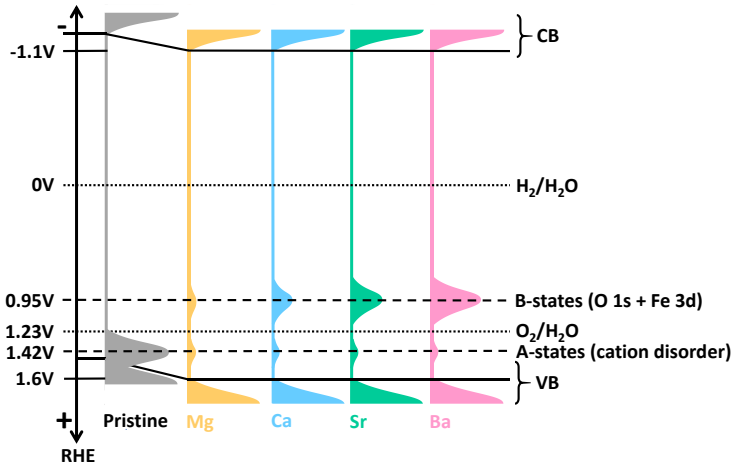

Figure 4-15 Schematic representation of the position of valence band edge as well as of the hydrated A- and B-states for pristine and AMC substituted LFO thin films. A-states are linked to intrinsic defects linked to cation disorder, while B-states are a combination of O 1s and Fe 3d states associated with high Fe-oxidation states.

As elaborated above, A-states are intrinsic defects that are from cation disorder, and the orbital hybridization between O 1s and Fe 3d leads to the formation of B-states. The dampening of intrinsic A-states and the emergence of B-states upon the introduction of AMC is one of the most significant reasons for the improvement of photoelectrochemical behaviour in LFO thin films. With regards to A-states, these

are located close to the valence band, remaining fully populated across most of the potential range investigated. These states behave as hole-traps, slowing down the transport of the majority carriers. This can be observed in the dynamic photocurrent transient responses of pristine and 7% Ba^{2+} substituted LFO thin films (Figure 4-16), recorded under the same conditions as in Figure 4-12 after saturating the solution with Ar (a and b) and O_2 (c and d). The photocurrent rise time in the on-transient and decay time in the off-transient are slower in pristine LFO than AMC substituted LFO

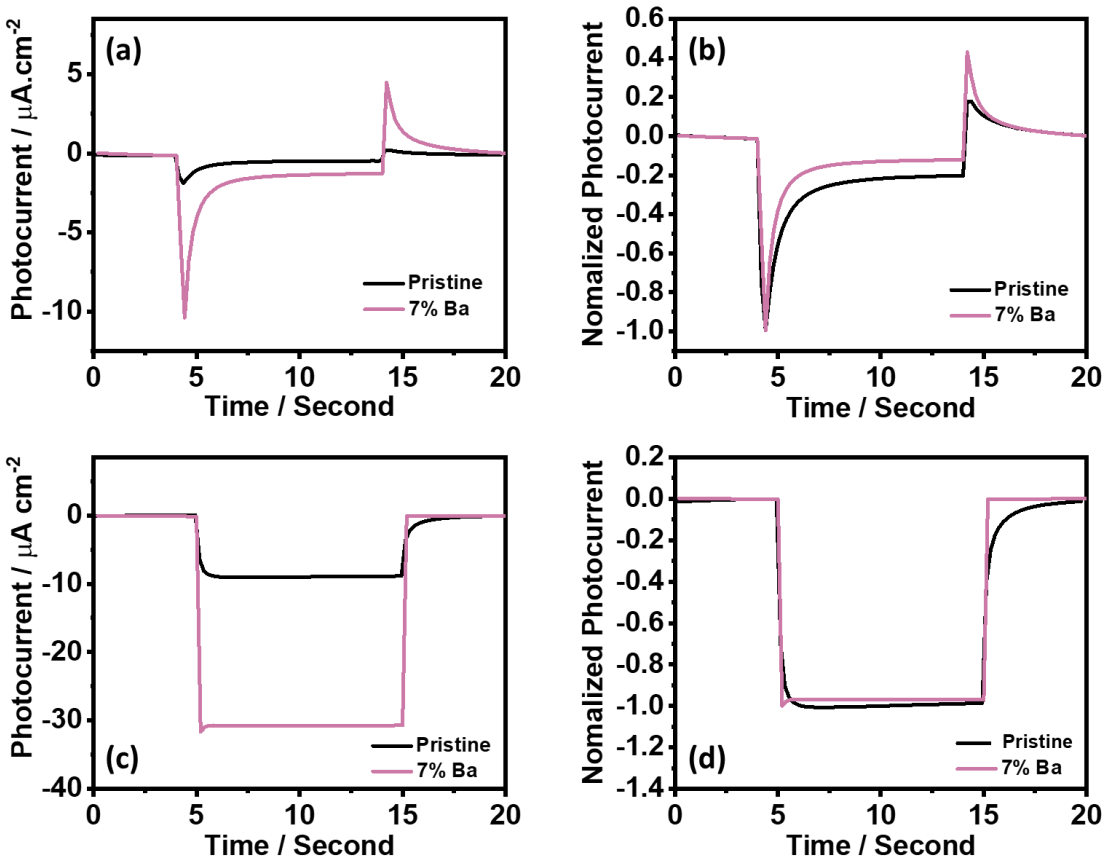

Figure 4-16 Dynamic photocurrent transient responses of pristine and 7% Ba^{2+} substituted LFO thin films at +0.45 V vs RHE in a 0.1M Na_2SO_4 aqueous solution (pH 12): under Ar-saturated solutions (a) and O_2-saturated solutions (c); Photocurrent transients normalised by the maximum photocurrent: Ar-saturated solutions (b) and O_2-saturated solutions (d). The thin films are illuminated with a 405 nm LED (3.25×10^{15} cm^{-2} s^{-1} photon flux).

films, which is clearly shown in the photocurrent transients normalised by the maximum photocurrent (Figure 4-16d). As demonstrated by Zhang et al., surface

states probed electrochemically act as majority carriers trap states in the presence of minority carrier scavengers, leading to transient photocurrent responses significantly slower than the RC time constant.[32] Consequently, the dampening of A-states upon AMC substitution is responsible for the sharpening of instantaneous (displacement) photocurrent shown in Figure 4-16a and c.

The enhancement of the photocurrent responses towards oxygen reduction is not only associated with an improvement in majority carrier transport (dampening of A-states) but crucially with increasing kinetics of electron transfer assisted via B-states. The Gerischer formalism for electron transfer is based on the isoelectronic nature of the interfacial process, i.e. heterogeneous electron transfer involves density of states in the solid and the redox species located at the same energy.[33–35] As shown in Figure 4-15, B-states are located close to the standard oxygen redox energy; therefore, these states can mediate electron transfer from LFO. This is supported by the electrochemical responses in Figure 4-17. The LSVs of pristine and Ba^{2+} substituted LFO thin films were performed in a O_2-saturated Na_2SO_4 aqueous solution at pH 12 in the dark with a scan rate of 5 mV s^{-1}, showing a substantial increase in dark current from 3.74 μA cm^{-2} to 20.61 μA cm^{-2} at +0.4 V vs RHE upon AMC (Ba^{2+}) substitution in Figure 4-17. Indeed, previous works have shown that O_2

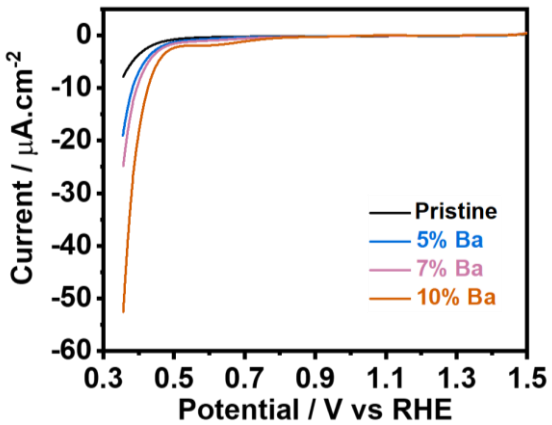

Figure 4-17 Electrochemical responses of pristine and Ba^{2+} substituted LFO thin films recorded at 5 mV s^{-1} in O_2-saturated Na_2SO_4 aqueous solutions (pH 12) in the dark.

reduction kinetics at perovskite oxides are strongly linked to the density of states in the potential range between +0.5 and +1.2 V vs RHE.[16,36] The data in Figure 4-17 show a systematic increase in the dark current at potentials lower than +0.8 V vs RHE, that is, once the density of B-states is fully populated. Under illumination, B-states are populated at all potentials accelerating the oxygen reduction kinetics (photocurrent).

The role of the sub-bandgap states in the photoelectrochemical hydrogen evolution reaction is somewhat less clear. We could postulate that in the absence of O_2, B-states can act as recombination centres as the charge transfer kinetics will be nominally zero. This is likely to be one reason for the comparatively smaller photostationary current at 7% Ba^{2+} substituted LFO thin films than pristine LFO photocathode under Ar-saturated solutions in Figure 4-16b. However, surface recombination can also occur in sub-band-gaps states (e.g., hole states) closed to the conduction band (CB) edge. This is inaccessible to be probed by electrochemical experiments, because various electrochemical reactions such as oxygen reduction are likely to cover the performance of sub-band-gaps states when relatively low potentials are applied to fill in those states. For example, the transient photocurrent of 7% Ba^{2+} substituted LFO photocathode in the presence of O_2 still displays a small spike in the on-transient in Figure 4-16c. This tends to be linked to hole states that are created by Fe^{4+} near the CB, leading to the charge carrier recombination. In this respect, it is important to raise a note of caution on rationalising experimental trends employing DFT based electronic structure calculations. Most studies reporting changes in electronic structures as a result of cation substitution correlate their findings with optimised stoichiometric structures, disregarding the variety of intrinsic defects present in these complex materials (particularly those synthesised under O_2-rich environment).[9,25] Consequently, our understanding of electronic states associated with extrinsic and intrinsic defect structures remain rather shallow. This

study only provides a partial picture into these complex issues which are crucial to our understanding of this class of high-correlated electron systems in electrocatalysis, photocatalysis and artificial photosynthesis.

4.4.9 The stability test of AMC substituted LFO photocathodes

The stability test of various LFO-based thin films (Figure 4-18) were performed under the same experimental conditions as in Figure 4-12. It is well-known that pristine LFO photocathode shows an attractive PEC stability.[5,9,10,37] But the LSV plots of AMC substituted thin films after 1 hour of continuous irradiation (Figure 4-18b)

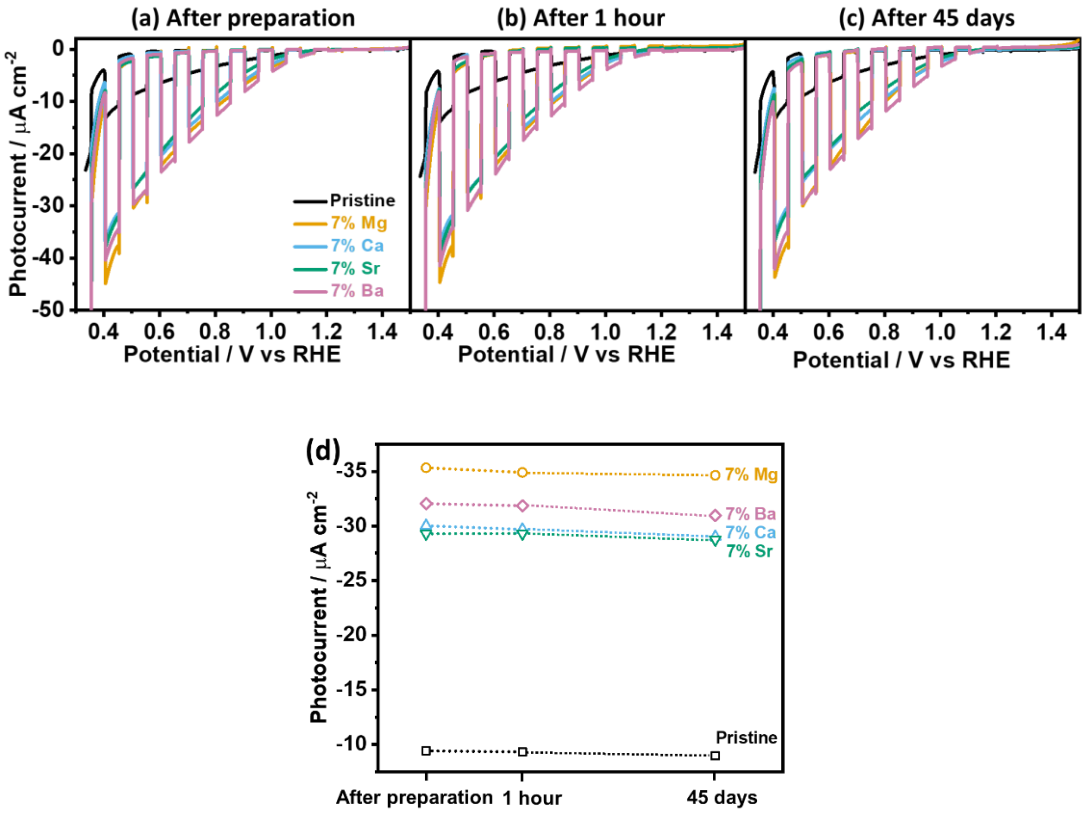

Figure 4-18 Stability test of 7% AMC substituted LFO thin films in O_2-saturated Na_2SO_4 aqueous solutions (pH 12) under illumination of a 405 nm LED (3.25×10^{15} cm^{-2} s^{-1} photon flux): LSV plots after preparation (a), after 1 hour of continuous illumination (b), after 45 days exposed to air (c) and photocurrent density extracted from Figure a, b and c vs. time plots at +0.4 V vs RHE (d).

and after 45 days exposed to air (Figure 4-18c) show identical photocurrent vs. potential trends in comparison with that for the first-time characterisation (Figure 4-18a), which indicates a strong PEC stability of AMC substituted LFO photoelectrodes. On the other hand, the photocurrents of various LFO-based thin films at +0.4 V vs RHE were selected from Figure 4-18a-c and plotted into Figure 4-18d as a function of time, displaying a constant photocurrent density. It should be noted that the photocurrent magnitude also remains almost the same during continuous irradiation for 1 hour (data of this process is not shown in Figure 4-18d). Therefore, it can be concluded that the stability of B-sites has the ability to remain active for long term applications.

4.5 Summary

Divalent alkaline-earth metal cations (AMC) Mg^{2+}, Ca^{2+}, Sr^{2+} and Ba^{2+} substitution into $LaFeO_3$ thin films prepared by sol-gel methods leads to changes in the electronic structure close to the valence band edge with a strong impact in photoelectrochemical performance. XRD and XPS analysis reveal a complex picture where parameters such as lattice constant and covalency are affected by the type and extent of AMC substitution. At very low substitution levels (below 5%), sites featuring higher Fe oxidation states promote the contraction of the lattice constant, which is partially compensated at higher substitution levels by strain effects arising from the larger AMC. XPS analysis reveals a linear correlation between the BE of Fe $2p_{3/2}$ and O 1s associated with the perovskite lattice, suggesting that the Fe oxidation state and covalency of the Fe-O bond are strongly correlated regardless of the AMC nature. The structural and electronic effects of AMC substitution also confirm that substitution takes place at the A-site, except for Mg^{2+}, which can also occupy B-sites.

The structural and electronic changes promoted by AMC substitution are probed by current-voltage curves and electrochemical impedance spectroscopy in alkaline solutions. Pristine LFO films exhibit states located around 100 to 200 meV above the valence band edge (A-states), which are linked to intrinsic defects such as cation vacancies. AMC substitution attenuates these states (while substantially increasing the density of majority carriers), as well as promoting deeper states centred at 600 meV above the valence band edge (B-states). Dynamic photoelectrochemical studies show that A-states acts as hole-traps, decreasing the mobility of charge carriers. On the other hand, B-states promotes the photoelectrochemical reduction of oxygen. In the absence of oxygen, AMC substitution increases in the displacement (transient) photocurrent but the photostationary values are strongly affected by surface recombination. Currently, it remains to be fully elucidated whether surface recombination occurs at B-states or higher sub-bandgap states under oxygen-free solutions. These observations strongly point forwards to a significant improvement of LFO as photocatalysts for water remediation upon AMC substitution below 10%. With regards to photoelectrochemical hydrogen generation, new approaches are required in order to minimise intrinsic hole-trap states while promoting density of states near the conduction band, which can facilitate interfacial electron transfer.

4.6 References

(1) Wang, P.; He, Y.; Mi, Y.; Zhu, J.; Zhang, F.; Liu, Y.; Yang, Y.; Chen, M.; Cao, D. Enhanced Photoelectrochemical Performance of $LaFeO_3$ Photocathode with Au Buffer Layer. *RSC Adv.* **2019**, *9*, 26780–26786.

(2) Guigoz, V.; Balan, L.; Aboulaich, A.; Schneider, R.; Gries, T. Heterostructured Thin $LaFeO_3$/g-C_3N_4 Films for Efficient Photoelectrochemical Hydrogen Evolution. *Int. J. Hydrogen Energy* **2020**.

(3) Freeman, E.; Kumar, S.; Celorrio, V.; Park, M. S.; Kim, J. H.; Fermin, D. J.; Eslava, S. Strategies for the Deposition of $LaFeO_3$ Photocathodes: Improving the Photocurrent with a Polymer Template. *Sustain. Energy Fuels* **2020**, *4*, 884–894.

(4) Son, M. K.; Seo, H.; Watanabe, M.; Shiratani, M.; Ishihara, T. Characteristics of Crystalline Sputtered $LaFeO_3$ Thin Films as Photoelectrochemical Water Splitting Photocathodes. *Nanoscale* **2020**, *12*, 9653–9660.

(5) Celorrio, V.; Bradley, K.; Weber, O. J.; Hall, S. R.; Fermín, D. J. Photoelectrochemical Properties of $LaFeO_3$ Nanoparticles. *ChemElectroChem* **2014**, *1*, 1667–1671.

(6) Wang, L.; Lee, C. Y.; Schmuki, P. Influence of Annealing Temperature on Photoelectrochemical Water Splitting of α-Fe_2O_3 Films Prepared by Anodic Deposition. *Electrochim. Acta* **2013**, *91*, 307–313.

(7) Kim, J. H.; Kim, J. H.; Jang, J. W.; Kim, J. Y.; Choi, S. H.; Magesh, G.; Lee, J.; Lee, J. S. Awakening Solar Water-Splitting Activity of $ZnFe_2O_4$ Nanorods by Hybrid Microwave Annealing. *Adv. Energy Mater.* **2015**, *5*, 1–9.

(8) Warren, S. C.; Voïtchovsky, K.; Dotan, H.; Leroy, C. M.; Cornuz, M.; Stellacci, F.; Hébert, C.; Rothschild, A.; Grätzel, M. Identifying Champion Nanostructures for Solar Water-Splitting. *Nat. Mater.* **2013**, *12*, 842–849.

(9) Wheeler, G. P.; Baltazar, V. U.; Smart, T. J.; Radmilovic, A.; Ping, Y.; Choi, K. S. Combined Theoretical and Experimental Investigations of Atomic Doping to Enhance Photon Absorption and Carrier Transport of $LaFeO_3$ Photocathodes. *Chem. Mater.* **2019**, *31*, 5890–5899.

(10) Wheeler, G. P.; Choi, K. S. Photoelectrochemical Properties and Stability of Nanoporous P-Type $LaFeO_3$ Photoelectrodes Prepared by Electrodeposition. *ACS Energy Lett.* **2017**, *2*, 2378–2382.

(11) Díez-García, M. I.; Gómez, R. Metal Doping to Enhance the Photoelectrochemical Behavior of $LaFeO_3$ Photocathodes. *ChemSusChem* **2017**, *10*, 2457–2463.

(12) Prévot, M. S.; Guijarro, N.; Sivula, K. Enhancing the Performance of a Robust Sol-Gel-Processed p-Type Delafossite $CuFeO_2$ Photocathode for Solar Water Reduction. *ChemSusChem* **2015**, *8*, 1359–1367.

(13) Hayashi, N.; Yamamoto, T.; Kageyama, H.; Nishi, M.; Watanabe, Y.; Kawakami, T.; Matsushita, Y.; Fujimori, A.; Takano, M. $BaFeO_3$: A Ferromagnetic Iron Oxide. *Angew. Chemie - Int. Ed.* **2011**, *50*, 12547–12550.

(14) Celorrio, V.; Calvillo, L.; Granozzi, G.; Russell, A. E.; Fermin, D. J. $AMnO_3$ (A = Sr, La, Ca, Y) Perovskite Oxides as Oxygen Reduction Electrocatalysts. *Top. Catal.* **2018**, *61*, 154–161.

(15) Celorrio, V.; Calvillo, L.; van den Bosch, C. A. M.; Granozzi, G.; Aguadero, A.; Russell, A. E.; Fermín, D. J. Mean Intrinsic Activity of Single Mn Sites at $LaMnO_3$ Nanoparticles Towards the Oxygen Reduction Reaction. *ChemElectroChem* **2018**, *5*, 3044–3051.

(16) Celorrio, V.; Calvillo, L.; Dann, E.; Granozzi, G.; Aguadero, A.; Kramer, D.; Russell, A. E.;

Fermín, D. J. Oxygen Reduction Reaction at $La_xCa_{1-x}MnO_3$ Nanostructures: Interplay between A-Site Segregation and B-Site Valency. *Catal. Sci. Technol.* **2016**, *6*, 7231–7238.

(17) Wang, L.; Du, Y.; Sushko, P. V.; Bowden, M. E.; Stoerzinger, K. A.; Heald, S. M.; Scafetta, M. D.; Kaspar, T. C.; Chambers, S. A. Hole-Induced Electronic and Optical Transitions in $La_{1-x}Sr_xFeO_3$ Epitaxial Thin Films. *Phys. Rev. Mater.* **2019**, *3*, 1–8.

(18) Grosvenor, A. P.; Kobe, B. A.; Biesinger, M. C.; McIntyre, N. S. Investigation of Multiplet Splitting of Fe 2p XPS Spectra and Bonding in Iron Compounds. *Surf. Interface Anal.* **2004**, *36*, 1564–1574.

(19) Brundle, C. R.; Chuang, T. J.; Wandelt, K. Core and Valence Level Photoemission Studies of Iron Oxide Surfaces and the Oxidation of Iron. *Surf. Sci.* **1977**, *68*, 459–468.

(20) She, S.; Yu, J.; Tang, W.; Zhu, Y.; Chen, Y.; Sunarso, J.; Zhou, W.; Shao, Z. Systematic Study of Oxygen Evolution Activity and Stability on $La_{1-x}Sr_xFeO_{3-\delta}$ Perovskite Electrocatalysts in Alkaline Media. *ACS Appl. Mater. Interfaces* **2018**, *10*, 11715–11721.

(21) Zhu, Y.; Zhou, W.; Yu, J.; Chen, Y.; Liu, M.; Shao, Z. Enhancing Electrocatalytic Activity of Perovskite Oxides by Tuning Cation Deficiency for Oxygen Reduction and Evolution Reactions. *Chem. Mater.* **2016**, *28*, 1691–1697.

(22) Shi, C.; Qin, H.; Zhao, M.; Wang, X.; Li, L.; Hu, J. Investigation on Electrical Transport, CO Sensing Characteristics and Mechanism for Nanocrystalline $La_{1-x}Ca_xFeO_3$ Sensors. *Sensors Actuators, B Chem.* **2014**, *190*, 25–31.

(23) Hu, S.; Zhang, L.; Liu, H.; Cao, Z.; Yu, W.; Zhu, X.; Yang, W. Alkaline-Earth Elements (Ca, Sr and Ba) Doped $LaFeO_{3-\delta}$ Cathodes for CO_2 Electroreduction. *J. Power Sources* **2019**, *443*, 1–10.

(24) Bocquet, A. E.; Fujimori, A.; Mizokawa, T.; Saitoh, T.; Namatame, H.; Suga, S.; Kimizuka, N.; Takeda, Y.; Takano, M. Electronic Structure of $SrFe^{4+}O_3$ and Related Fe Perovskite Oxides. *Phys. Rev. B* **1992**, *45*, 1561–1570.

(25) Shen, Z.; Zhuang, Y.; Li, W.; Huang, X.; Oropeza, F. E.; Hensen, E. J. M.; Hofmann, J. P.; Cui, M.; Tadich, A.; Qi, D.; Cheng, J.; Li, J.; Zhang, K. H. L. Increased Activity in the Oxygen Evolution Reaction by Fe^{4+}-Induced Hole States in Perovskite $La_{1-x}Sr_xFeO_3$. *J. Mater. Chem. A* **2020**, *8*, 4407–4415.

(26) Ritzmann, A. M.; Muñoz-García, A. B.; Pavone, M.; Keith, J. A.; Carter, E. A. Ab Initio DFT+U Analysis of Oxygen Vacancy Formation and Migration in $La_{1-x}Sr_xFeO_{3-\delta}$ (x = 0, 0.25, 0.50). *Chem. Mater.* **2013**, *25*, 3011–3019.

(27) Taylor, F. H.; Buckeridge, J.; Catlow, C. R. A. Defects and Oxide Ion Migration in the Solid Oxide Fuel Cell Cathode Material $LaFeO_3$. *Chem. Mater.* **2016**, *28*, 8210–8220.

(28) Stoerzinger, K. A.; Wang, L.; Ye, Y.; Bowden, M.; Crumlin, E. J.; Du, Y.; Chambers, S. A. Linking Surface Chemistry to Photovoltage in Sr-Substituted $LaFeO_3$ for Water Oxidation. *J. Mater. Chem. A* **2018**, *6*, 22170–22178.

(29) Acharya, S.; Mondal, J.; Ghosh, S.; Roy, S. K.; Chakrabarti, P. K. Multiferroic Behavior of Lanthanum Orthoferrite ($LaFeO_3$). *Mater. Lett.* **2010**, *64*, 415–418.

(30) Taylor, F. H.; Buckeridge, J.; Catlow, C. R. A. Screening Divalent Metals for A- and B-Site Dopants in $LaFeO_3$. *Chem. Mater.* **2017**, *29*, 8147–8157.

(31) Cardon, F.; Gomes, W. P.; On The Determination of The Flat-band Potential of A Semiconductor in Contact with A Metal or An Electrolyte from The Mott-Schottky Plot. *J. Phys. D: Appl. Phys.* **1978**, *11*, L63-L67.

(32) Zhang, Q.; Celorrio, V.; Bradley, K.; Eisner, F.; Cherns, D.; Yan, W.; Fermín, D. J. Density of Deep Trap States in Oriented TiO_2 Nanotube Arrays. *J. Phys. Chem. C* **2014**, *118*, 18207–18213.

(33) Gerischer, H. Über Den Ablauf von Redoxreaktionen an Metallen Und an Halbleitern: I. Allgemeines Zum Elektronenübergang Zwischen Einem Festkörper Und Einem Redoxelektrolyten. *Zeitschrift fur Phys. Chemie* **1960**, *26*, 223–247.

(34) Gerischer, H. Über Den Ablauf Von Redoxreaktionen an Metallen Und an Halbleitern Iii. Halbleiterelektroden. *Zeitschrift fur Phys. Chemie* **1961**, *27*, 48–79.

(35) Kissling, G. P.; Bünzli, C.; Fermín, D. J. Tuning Electrochemical Rectification via Quantum Dot Assemblies. *J. Am. Chem. Soc.* **2010**, *132*, 16855–16861.

(36) Celorrio, V.; Dann, E.; Calvillo, L.; Morgan, D. J.; Hall, S. R.; Fermin, D. J. Oxygen Reduction at Carbon-Supported Lanthanides: The Role of the B-Site. *ChemElectroChem* **2016**, *3*, 283–291.

(37) Pawar, G. S.; Tahir, A. A. Unbiased Spontaneous Solar Fuel Production Using Stable $LaFeO_3$ Photoelectrode. *Sci. Rep.* **2018**, *8*, 1-9.

CHAPTER 5.

High interfacial hole-transfer efficiency at $GaFeO_3$ thin film photoanodes

Portions of this chapter have been prepared for publication.

Sun, X.; Tiwari, D.; Fermin, D. J. High Interfacial Hole-transfer Efficiency at $GaFeO_3$ Thin Film Photoanodes. *Adv. Energy Mater.* **2020**, 10, 2002784.

X.S. prepared all samples and conducted all characterisations reported in this thesis. The SEM and EIS characterisations were performed in collaboration with D.T. The computational section was contributed by D.T.

5.1 Abstract

The photoelectrochemical properties of polycrystalline $GaFeO_3$ (GFO) thin films are investigated for the first time. Thin films prepared by sol-gel methods exhibit phase-pure orthorhombic GFO with the Pc21n space group, as confirmed by quantitative XRD analysis and Raman spectroscopy. Optical responses are characterised by an interband transition at 2.72 eV and sub-bandgap d-d transitions associated with octahedral and tetrahedral coordination of Fe^{3+} sites. DFT-HSE06 electronic structure calculations show GFO is highly ionic with very low dispersion in the valence band maximum (VBM) and conduction band minima (CBM). Electrochemical impedance spectroscopy reveals n-type conductivity with a flat band potential (U_{fb}) of +0.52 V vs RHE, indicating that GFO has the deepest CBM reported of any ferrite. Photoelectrochemical responses in the presence of SO_3^{2-} acting as hole-scavenger shows an ideal semiconductor-electrolyte interfacial behavior with no evidence of surface recombination down to the U_{fb}. Remarkably, the onset potential for the oxygen evolution reaction also coincides with the U_{fb}, showing interfacial hole-transfer efficiency above 50%. The photoelectrochemical properties are limited by bulk recombination due to the short-diffusion length of minority carriers as well as slow transport of majority carriers. Strategies towards developing high-efficiency GFO photoanodes are briefly discussed.

5.2 Introduction

5.2.1 Overview of current photoanodes

Chapter 3 and 4 have briefly introduced the progress of photocathodes, which offers a comparable picture into LFO thin film studies. As for photoanode, most of them have been widely studied are metal oxide-based materials owing to the

requirement of stability under oxidizing conditions.[1] Indeed, the current research related to oxide-based photoanodes is mainly concentrated on a small group of materials, especially for so-called dimensionally stable binary oxides such as TiO_2 and Fe_2O_3, in the field of PEC water splitting.[2,3] In addition, a large percentage of instable binary oxides-based photoanodes (e.g., ZnO and WO_3) have also attracted widespread attention, due to their relatively high PEC activity.[4,5] These absorbers have been investigated for nearly half a century; however, there is still a long research road to explore to achieve their viable and scalable PEC water splitting devices. It is undeniable that PEC water splitting is an emerging technology in comparison with PV devices, and the long research cycle is worth waiting for. The past few decades witness the rise of ternary oxide-based photoanodes. $BiVO_4$ remains the benchmark, showing excellent energy conversion efficacy and photochemical stability.[6] But it is limited by surface recombination, leading to the onset potential of around +0.8 V vs RHE for water oxidation.[7] The PEC performances of the rest typical complex n-type metal oxides can be seen in Table 1-1. It is worth mentioning ferrite-based photoanodes since they tend to remain those advantages from hematite in the process of PEC water splitting. For example, $ZnFe_2O_4$ photoanode shows a band gap of approximately 2.0 eV and good PEC stability and inertness.[8] After more than 30 years of research, it has achieved EQE above 10% at a wavelength around 350 nm and onset potential approximately +0.62 V vs RHE for OER through the optimization of annealing process and surface catalytic activity.[8,9] Recently, Zhang et al. reported that a $InFeO_3$ photoanode shows a higher EQE (6.5% at 400 nm) and better onset potential (+0.65 V vs RHE) than a α-Fe_2O_3 film for the water oxidation reaction,[10] though indium as a non-Earth-abundant element will increase the production cost of $InFeO_3$ and against the sustainable development for our planet. Other ferrite photoanodes such as $MgFe_2O_4$ and $CuFe_2O_4$ show the EQE value are between 3.5% - 4% at a wavelength of 400 nm and the onset potentials are around +0.64 V vs RHE and +0.8 V vs RHE, respectively, upon the loading of NiFeOx

as cocatalysts.[11] It should be noted that both surface and bulk charge transfer efficiency remain very low values in these intrinsic ferrite-based photoanodes, though various innovation methods (e.g., surface cocatalyst loading) can dramatically promote their PEC performance.

5.2.2 The selection of absorber ($GaFeO_3$)

Ferroelectric materials such as $BiFeO_3$ and Bi_2FeCrO_6 show promising PEC properties in the family of oxide-based photoelectrodes due to their unique spontaneous polarization and efficient charge separation.[12,13] For example, a reversed polarization induced by external electric field leads to a switchable photoelectrode (interchange between photocathode and photoanode) in the same ferroelectric.[12] Meanwhile, there is an enhancement in photocurrent responses, as the process of polarization makes the built-in electric field strong, promoting charge separation.[12] Gallium ferrite is a noted ferroelectricity with spontaneous polarization properties, indicating that GFO tends to possess those unconventional PEC performance mentioned above in the process of water splitting. Furthermore, the composition of GFO suggests that it can be an attractive candidate in the field of PEC water splitting, since ternary metal oxides presents a series of benefits to PEC performance as mentioned in Chapter 3. Interestingly, the similar Ga^{3+} and Fe^{3+} ionic radius enables GFO to show high cation disorder behaviour, which is distinct from other ternary metal oxides. This property may enable GFO to show unique PEC performance linked to the flexible electronic structure. Therefore, based on those advantages mentioned above, GFO is likely to be a fascinating material that can be employed in PEC water splitting device. Up to now, however, the investigations of GFO are mainly focused on magnetic properties;[14–16] by contrast, there is no report related to GFO performance in the process of PEC water splitting. Only Dhanasekaran and co-worker demonstrated that GFO has the photocatalytic activities for water splitting under visible light illumination.[17]

This chapter describes, for the first time, the unique photoelectrochemical properties of GFO photoanode. Polycrystalline GFO thin films are prepared by sol-gel methods exhibiting a high degree of phase purity (orthorhombic with the Pc21n space group) featuring over 150 XRD peaks, as well as 25 different Raman modes which are assigned to Ga and Fe sites in octahedral and tetrahedral coordination. Indeed, a variety of sub-bandgap optical transitions observed in as grown films are also consistent with both coordination geometries of Fe sites, suggesting a degree of elemental disorder. On the other hand, EDX and XPS analysis show identical Ga:Fe bulk and surface ratio, which is rather unusual in multicomponent transition metal oxides with the general formula ABO_3. The valence band spectrum is dominated by O 2p orbitals with a small degree of hybridization, as confirmed by DFT band composition calculations, demonstrating the strong ionic character of this ferrite. Differential capacitance data extracted from electrochemical impedance spectroscopy reveals a n-type conductivity with a flat band potential (U_{fb}) of +0.52 V vs RHE, which corresponds to the deepest conduction band reported for any ferrite. In the presence of SO_3^{2-}, GFO exhibits ideal semiconductor/electrolyte behavior, with no surface recombination, but limited by minority and majority carrier transport. Remarkably, the photocurrent onset potential for the oxygen evolution reaction coincides with U_{fb}, showing the highest interfacial charge transfer efficiency for polycrystalline thin films without the need for any co-catalysts. We also demonstrate that charge transport properties are highly sensitive to the Ga:Fe ratio, which opens new avenues for developing high-performance photoanodes.

5.3 Experimental Section

5.3.1 Materials

$Ga(NO_3)_3 \cdot xH_2O$ (99.999%) and $Fe(NO_3)_3 \cdot 9H_2O$ (99.999%), were purchased from Sigma-Aldrich company. Citric acid was purchased from Fisher Scientific company. Solvents: ethanol (99.8%), iso-propanol (99.8%), acetone (99.5%) and ethylene glycol (99.5%) were purchased from Sigma-Aldrich company. FTO-coated glass substrates (surface resistivity ~ 7 Ω sq^{-1}) were purchased from Sigma-Aldrich company. Distilled water was produced by Milli-Q systems (18.4 MΩ cm). All materials were used directly without further purification. The amount of crystal water in gallium nitrate were determined employing thermogravimetric analysis (TGA). The repeatable TGA results show there is six crystal water combined with each $Ga(NO_3)_3$ unit.

5.3.2 The preparation of $GaFeO_3$ thin film

The synthesis of GFO thin films was modified the sol-gel method shown in Chapter 4. Firstly, 1mL of an aqueous solution of 0.5 M $Ga(NO_3)_3 \cdot 6H_2O$ and 1 mL of an aqueous solution of 0.5 M $Fe(NO_3)_3 \cdot 9H_2O$ were mixed and stirring at 60 ^oC for 1 hour. To this, 1 mL ethanolic solution of 1 M citric acid and 62.5 mL ethylene glycol were added, and the solution was further stirred overnight in a capped glass vial. The obtained precursor solution was spin-coated onto clean $F:SnO_2$ (FTO) conductive glass at 3000 rpm for 30 seconds, followed by drying at 100 ^oC for 10 minutes and thermolysing the metal-complex at 400 ^oC for 1 hour, to deposit 1 layer of GFO. Thicker films are obtained by repeating the same procedure and building the thickness layer-by-layer. The final films were annealed at 600 ^oC for 8 hours (ramp rate: 5 ^oC min^{-1}) to obtain crystalline GFO thin films. The Ga^{3+} and Fe^{3+} precursors were stoichiometrically changed following $Ga_{2-x}Fe_xO_3$ (x from 0.8 to 1.3) compositions to prepare the thin films with different Ga:Fe ratio.

5.3.3 Computational methods

GFO electronic structure calculations were carried out by D.T. using the CASTEP18,19 and HSE06 functional-based hybrid-DFT methodology. Norm-conserving pseudopotentials with an energy cut-off of 1100 eV and Monkhorst-Pack k-point grid spaced < 0.02 $Å^{-1}$ were employed throughout the calculations. For structure optimization, strict convergence criteria were implemented, including energy and force tolerances of 1 neV and 1 meV $Å^{-1}$, respectively. The optimized $GaFeO_3$ unit-cell has orthorhombic symmetry (Pc21n) and dimensions within 1% of experimental results. The band structure and density of states (DOS) calculations were also performed with the same energy convergence and parameters.

5.4 Results and Discussion

5.4.1 The complexity of $GaFeO_3$ structure

The complex structural properties of GFO prepared by thermolysis of a sol-gel precursor containing nitrate salts of both cations, citric acid, and ethylene glycol at 400 ^oC, followed by annealing at 600 ^oC in the air for 8 h (see Experimental Section), are shown in Figure 5-1. The powder XRD pattern (Figure 5-1a) features over 150 Bragg reflections which closely match the standard pattern of orthorhombic GFO. The figure also shows the large number of reflections associated with the binary phases ε-Ga_2O_3 and ε-Fe_2O_3 over the range of 2θ values investigated. These results emphasize the need for high-quality XRD diffractograms and quantitative refinement to unambiguously demonstrate phase purity in this complex material. Figure 5-1a illustrates the full-profile Rietveld refinement of the experimental diffractogram to the orthorhombic GFO structure (Pc21n space group), with correlation parameter Rp= 5.11 and Rwp = 3.06 and a rather flat difference curve.

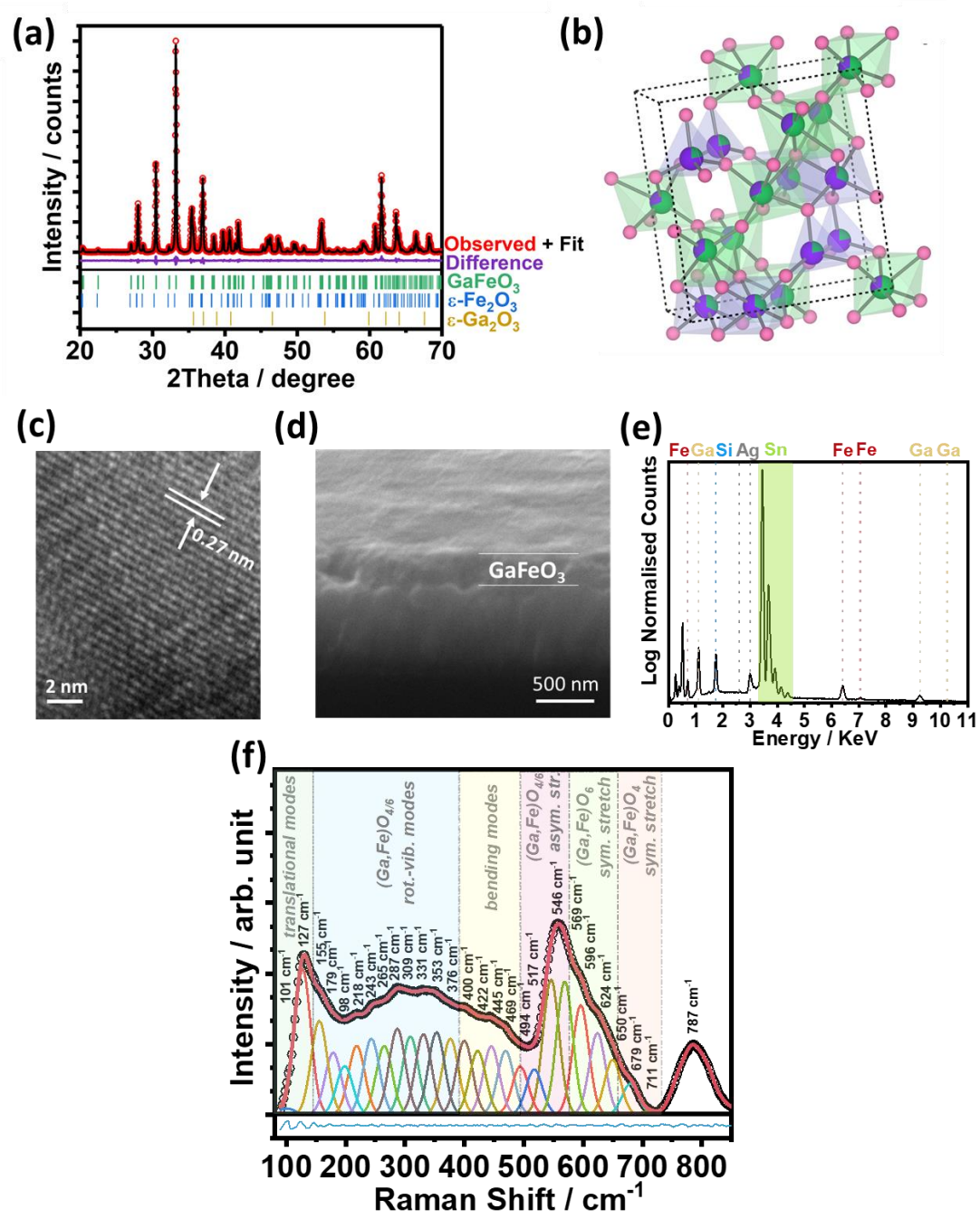

Figure 5-1 $GaFeO_3$ (GFO) structural complexity: (a) powder XRD with quantitative Rietveld analysis; (b) schematic of the GFO unit cell, featuring Ga (purple) and Fe (green) sites with tetrahedral and octahedral coordination geometries; (c) HR-TEM of GFO powder with lattice fringes associated with {221} planes; (d) cross-sectional SEM image of a GFO film obtained after 10 coating steps onto FTO glass; (e) EDX spectrum recorded at the top of the film after dc-sputter coating a 20 nm Ag layer; and (f) Raman spectrum of GFO films under 514 nm excitation, featuring 27 modes deconvoluted using Voigt functions.

The estimated orthorhombic unit cell parameters are a = 8.73589(72) Å, b = 9.38098(74) Å and c = 5.07718(42) Å, with the unit cell consisting of 40 atoms equivalent to 8 GFO formula units. The unit cell in Figure 1b exhibits 4 different crystallographic sites for metals atoms, including two with tetrahedral coordination and two with octahedral coordination. The octahedra form a network in the structure through shared terminals. The structural parameters obtained from the refinement are summarized in the crystallographic information file (CIF), which can be accessed from the crystallographic database through the CSD repository number: 2025904. The analysis is consistent with previous neutron diffraction studies reported by Mishra et al.[18] One notable feature which is commonly observed in the GFO crystal structure is the mixed occupancy at the metal sites, which varies significantly with synthesis methods and condition. This arises because of the similar ionic radius of Ga^{3+} and Fe^{3+}. This feature is a defining aspect of the photoelectrochemistry responses, as discussed further below. The crystalline nature of the GFO powders can be observed by the lattice fringes in the high-resolution transmission electron micrograph (HR-TEM) image in Figure 5-1c, featuring a d-spacing of 0.27 nm, which is linked to {221} planes.

Figure 5-1d shows the cross-sectional scanning electron microscope (SEM) image of GFO thin film after 10 coating steps on FTO substrate, indicating a thickness of 350 nm. The thin films were obtained by consecutive spin-coating, drying, and thermolysis steps, followed by annealing at the 600 ^{o}C in the air for 8 hours (see Experimental Section). Energy-dispersive X-rays (EDX) analysis shows the Ga:Fe ratio of 1.19 (±0.1) in GFO thin film. In order to prevent charging of the GFO thin film, dc-sputter coating was employed before the acquirement of EDX spectrum, so that the silver peaks in Figure 5-1e is from dc-sputter coating a thin Ag layer (20 nm).

The Raman signature arising from the C2v(9) point group symmetry of orthorhombic GFO thin films are shown in Figure 5-1f. The spectrum is deconvoluted

with approximately 27 modes in the range of 100 to 800 cm^{-1}, matching modes reported in single crystals,[19] assigned to Ga^{3+} polyhedral as well as Fe^{3+} in tetrahedral and octahedral coordination.[20–23] Stretching modes are observed between 500 - 750 cm^{-1} with tetrahedral and symmetric stretches appearing at higher frequencies, while modes above 760 cm^{-1} are likely due to Ga^{3+}.[24] The spectrum only shows a fraction of the 117 Raman active normal modes expected for a 40 atom unit-cell, including 29 A1, 30 A2, 29 B1, and 29 B2.[19] However, this pattern is highly consistent with phase pure materials previously reported.[25,26]

5.4.2 XPS characterisation of $GaFeO_3$ thin films

The X-ray photoelectron spectroscopy (XPS) survey spectrum in Figure 5-2a shows a variety of features, including prominent Ga (Ga $2p_{1/2}$, Ga $2p_{3/2}$, Ga 3s, Ga 3p, and Ga 3d), Fe (Fe $2p_{1/2}$, Fe $2p_{3/2}$, and Fe 3p) and oxygen (O 1s) photoemission lines, as well as the corresponding Auger lines. Ga 2p (Figure 5-2b) shows the spin-orbit components of Ga $2p_{3/2}$ and $2p_{1/2}$ with a splitting of 26.9 eV, along with loss feature at around 1136 eV. Furthermore, the Ga $2p_{3/2}$ peak position at 1118 eV is characteristic of native gallium oxide, confirming that Ga is in a +3 oxidation state.[27,28] The main feature of the O 1s spectrum (Figure 5-2c) is centered at 530 eV, which is assigned to lattice bound oxygen,[29] while the other contributions are linked to surface hydroxyl and carbonylated groups.[30] Fe 2p core-level (Figure 5-2d) is significantly more complex to rationalize due to contribution from various phenomena such as multiple-splitting, multiple oxidation states, and charge transfer effects. As a first approximation, the most intense component in Fe $2p_{3/2}$ is at 710.8 eV, with a 13.5 eV splitting from the Fe $2p_{1/2}$ component, which is consistent with a Fe +3 oxidation state.[29,31] Evidence of higher oxidation states can be linked to the higher binding energy components; however, this would require further analysis of other Fe core levels.[32] Interestingly, the observed surface Ga:Fe of 1.17 is very close to the bulk values obtained by EDX (1.19, Figure 5-1e) and XRD refined site

occupancy (1.15, Figure 5-1a). This behavior is rather unusual for transition metal oxides with the general ABO_3 formula (such as perovskites), which often exhibit different A:B ratio in the bulk and at the surface.[30,33]

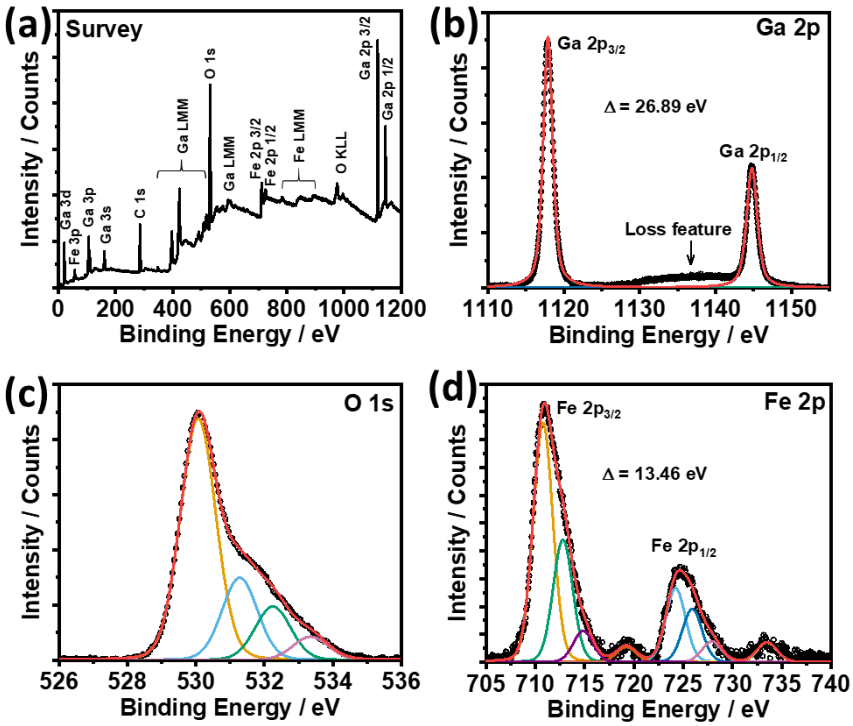

Figure 5-2 Surface composition analysis of GFO thin films using XPS: (a) survey spectrum showing the different photoemissions features; (b) Ga 2p core-level; (c) O 1s core-level; and (d) Fe 2p core-level. Spectral deconvolution is performed using Gaussian-Lorentzian mix functions.

5.4.3 Optical analysis of $GaFeO_3$ thin films

The optical properties of GFO thin films in the visible range are summarized in Figure 5-3. The absorption coefficient (α), extracted from transmittance and reflectance spectra of 350 nm films (Figure 5-3a), are displayed as a function of the photon energy, revealing several optical transitions between 1 and 3 eV (Figure 5-3b). The large $1/\alpha$ values indicate strong light capture cross section with energies larger than the optical band gap, which is characterized by a direct transition at 2.72 eV as estimated from the Tauc plot in Figure 5-3c. The energy differential plot of the absorption constant in Figure 5-3d reveals the various sub-bandgap features in the

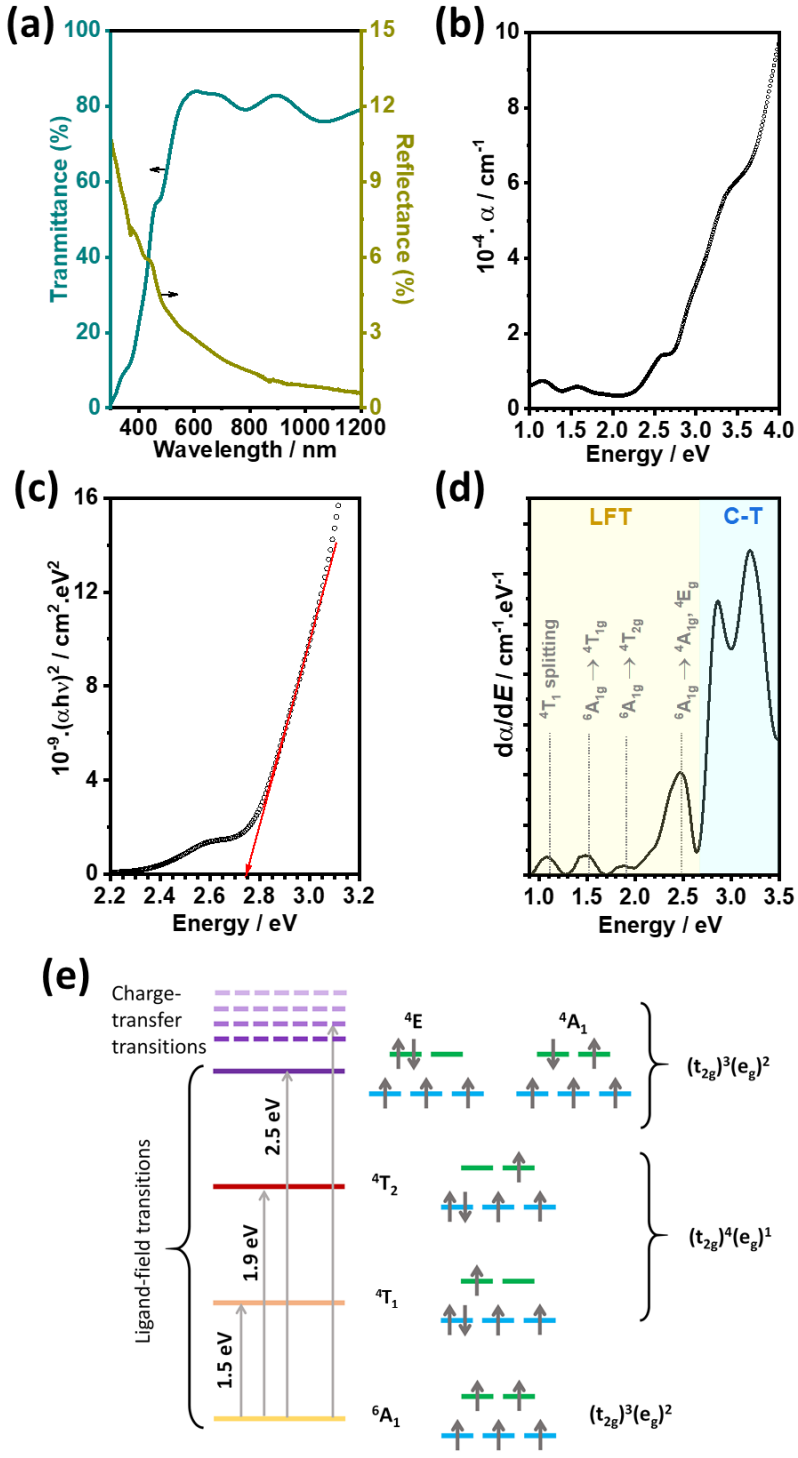

Figure 5-3 Optical properties of GFO thin films: (a) transmittance and reflectance spectra for a 350 nm GFO film; (b) absorption spectrum constructed from (a); (c) Tauc plot for bandgap determination assuming direct band-band transitions; (d) energy-differential absorption spectrum along with symmetry assignment for ligand-field (LFT) and charge-transfer transitions (C-T); and (e) modified TS diagram for Fe^{3+} in tetrahedral and octahedral field depicting the electronic configuration of states associated with the optical transitions.

visible range, which correspond to ligand-field or charge-transfer transitions.[14] As described below, the valence band maximum (VBM) and conduction band minimum (CBM) of GFO are primarily made up of transition metal Fe-3d and O-2p states, where Fe coordinates in both tetrahedral and octahedral geometry; thus the optical transitions can be described by merging Tanabe-Sugano (TS) diagrams of Fe^{3+} in both coordination geometries (Figure 5-3e).[34] The prominent d-d forbidden transitions can be related to the presence of distortions in the lattice, which is a further manifestation in the cation disorder in the material.

5.4.4 Band composition and energy of $GaFeO_3$ thin films

The valence band spectrum of GFO recorded using Al Kα X-rays source as excitation is illustrated in Figure 5-4a. To rationalise these features, electronic structure calculations using DFT with HSE06 functional (Figure 5-4b) were performed as described in the Experimental Section. The band diagram is characterized by rather flat conduction band minimum (CBM) and valence band maximum (VBM) in Figure 5-4c, indicating high effective masses of charge carriers and, thus, low mobilities. However, Figure 5-4c shows an indirect bandgap transition of GFO, which is contrary to the experimental results (direct band gap transition) estimated from Tauc plots (Figure 5-3c). This can also be rationalized by the feature of band edges. The rather flat band edges enable the phonon transition energy to be less than 35 meV at zero Kelvin. Upon illumination, such small energy plays a little effect on the optical transition of GFO at room temperature. In this case, the Tauc plot analysis fails to distinguish the type of bandgap. Figure 5-4b shows that the calculated DOS and valence bandwidth reproduce the spectral response accurately, although the finer orbital features are not experimentally resolved due to the small cross-section of the valence band states under X-ray excitation. The DFT calculations reflect the ionic nature of the oxide with the O 2p and Fe 3d states dominating the VBM and

CBM, respectively. Only a small degree of hybridization is calculated in the valence (O 2p, Fe 3d, and Ga 4p orbitals) and conduction bands (Fe 3d and O 2p orbitals).

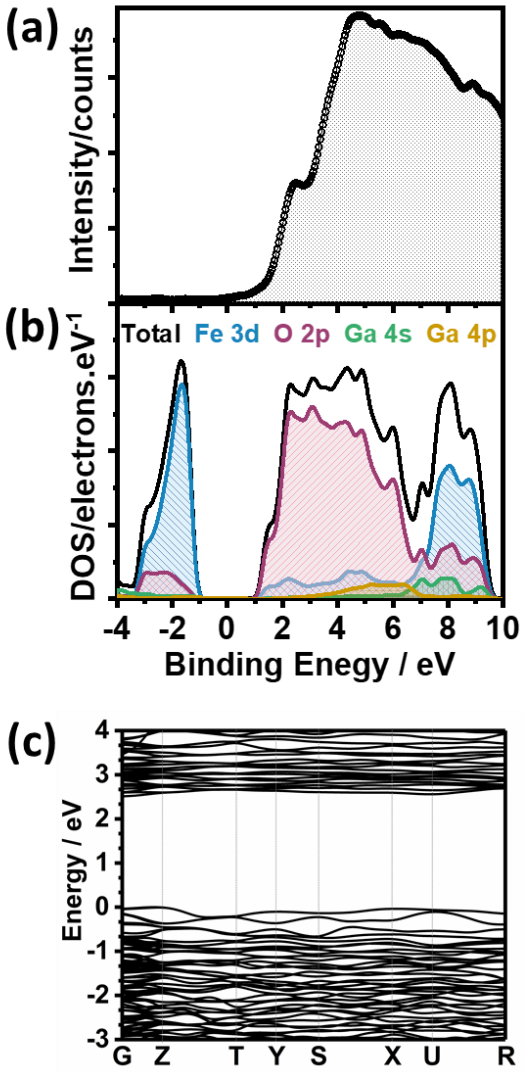

Figure 5-4 Bands composition and structure: (a) valence-band spectrum of a GFO thin film measured under Al-Kα X-ray excitation; (b) density of states (DOS) and (c) band structure of GFO calculated employing hybrid density functional theory (DFT) with HSE06 functional.

Figure 5-5a shows differential capacitance-potential curves obtained by electrochemical impedance spectroscopy of 350 nm GFO film in Ar-saturated 0.1M Na_2SO_4 aqueous solutions at pH 12. The sharp increase in capacitance at a potential

below +0.7 V vs RHE results from the thinning of the space charge layer as the n-type semiconductor approaches the flat band potential. A Mott-Schottky plot, constructed from Figure 5-5a, is displayed in Figure 5-5b. The positive slope reveals n-type semiconducting properties of as-grown GFO thin films. Based on Mott-Schottky equation (see previous chapters), the density of donor states (N_D) is around 1.9 × 10^{18} cm^{-3} in GFO thin films. The remarkable linearity of the Mott-Schottky plot over a range of 1V and right down to the flat band potential strongly suggest a low density of sub-band gap states near the CBM. The absence of Fermi level pinning is rather unusual in multicomponent semiconductor oxides,[35] in which cation and oxygen vacancies can generate a wide range of deep trap states.[36]

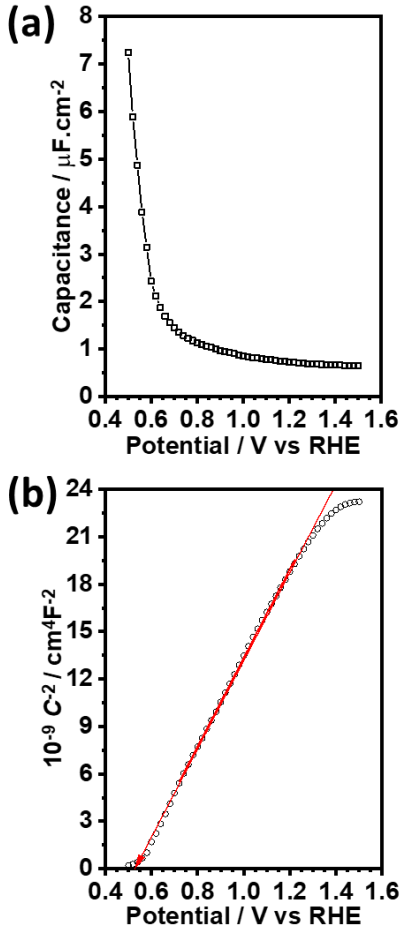

Figure 5-5 Flat band energy: (a) capacitance voltage curves extracted from electrochemical impedance spectroscopy of 350 nm GFO film in Ar-saturated 0.1M Na_2SO_4 aqueous solutions (pH 12) and (b) Mott-Schottky plot.

A flat-band potential (U_{fb}) of +0.52 V vs RHE can be estimated from the Mott-Schottky plot, which, as illustrated in Figure 5-6, corresponds to a very deep VBM value located at +3.22 V vs RHE. This is not only the deepest VBM reported for ferrite absorbers but also even deeper than wide-bandgap oxides such as ZnO and TiO_2. This unusual band energetic can be rationalised in terms of the effect of the FeO_6 octahedral tilting on the energy of the O 2p orbitals.[44] The ionic radius of gallium (0.62 Å) is significantly smaller than other A-site elements, such as La (1.36 Å), Y (0.9 Å) and Bi (1.03 Å); thus the Fe-O-Fe angle is less than 180° leading to the decrease of VBM. Furthermore, based on the model proposed by Meng et al.,[45] rather electronegative A-site cations (such as Ga^{3+}) tend to lower the CBM in FeO_6 coordinated structures with a low degree of hybridization. Figure 5-6 also shows the band alignment of GFO with common electron-transporting (ETL) and hole-transporting layers (HTL), indicating that establishing semiconductor junctions with appropriate band alignment will require unconventional materials.

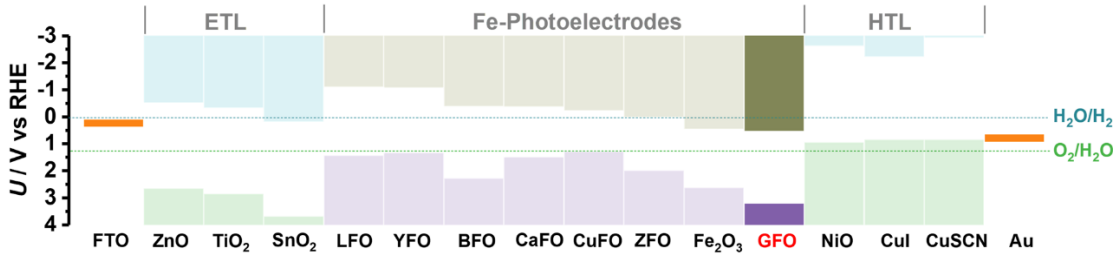

Figure 5-6 Band-alignment of GFO band-edges with respect to common electron-transport (ETL)[37] and hole-transport layers (HTL).[37] Band offset with other Fe based photoelectrodes including $LaFeO_3$ (LFO),[38] $YFeO_3$ (YFO),[31] $BiFeO_3$ (BFO),[39] $CaFe_2O_4$ (CaFO),[40] $CuFeO_2$ (CuFO),[41] $ZnFe_2O_4$ (ZFO),[42] and Fe_2O_3,[43] illustrates how deep is the VBM in GFO. The construction of the GFO band diagram is identical to Figure 4-15, as shown in section 4.4.8.

5.5 PEC characterisation of $GaFeO_3$ thin films

The unique structrual, optical and electronic properties of GFO thin films bring about a very unusual photoelectrochemical behavior as described in Figure 5-7. Figure 5-7a contrasts the current-voltage characteristics of a 350 nm GFO thin film under chopped illumination (405 nm) in Ar-purged 0.1 M Na_2SO_3 and 0.1 M Na_2SO_4 solutions (pH 12). The photocurrent onset-potential (photovoltage) is between +0.4

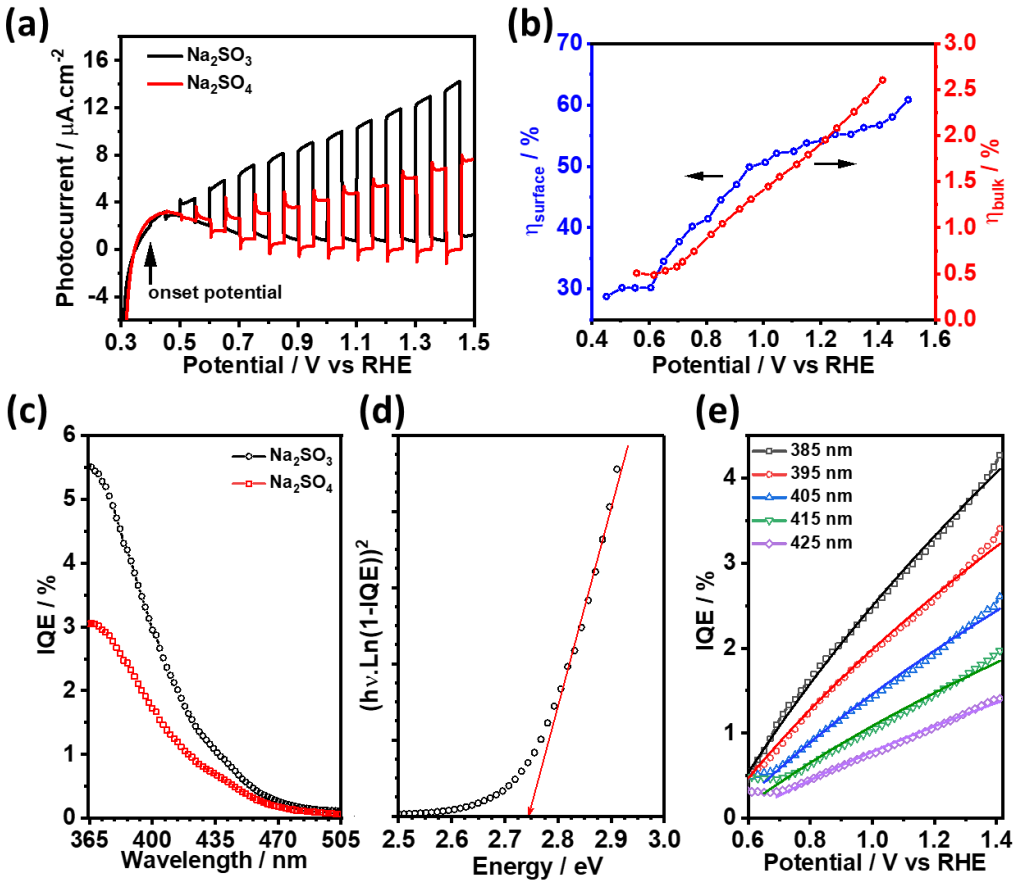

Figure 5-7 Photoelectrochemical responses of 350 nm GFO thin films: (a) linear sweep voltammetry (LSV) recorded at 5 mV s^{-1} under square wave 405 nm light perturbation and 4.25 × 10^{15} cm^{-2} s^{-1} photon flux in Ar-saturated 0.1M Na_2SO_3 and Na_2SO_4 electrolytes (pH 12); (b) the yield of surface and bulk charge transfer estimated from (a); (c) IQE at +1.4 V vs RHE as a function of wavelength; (d) Tauc plot analysis of IQE data; and (e) potential-dependence of IQE in Ar-saturated 0.1M Na_2SO_3 electrolytes (pH 12), along with fits to the Gärtner model (Eqn. 5-1).

and +0.5 V vs. RHE in both electrolytes, which is remarkably close to the U_{fb}. The magnitude of the photocurrent responses is larger in the presence of SO_3^{2-}, a strong hole scavenger that can effectively suppress surface recombination.[46] The photocurrent decay in the light on-transients and the negative overshoot in the off-transient in the SO_4^{2-} solution are also evidence of surface recombination competing with the oxygen evolution reaction.[46] Surface charge transfer efficiency ($\eta_{surface}$) is the photocurrent ratio between both electrolytes, measuring the interfacial hole-transfer efficiency towards OER, and bulk charge transfer efficiency (η_{bulk}) is the ratio between measured photocurrent and maximum photocurrent converted by absorbed photon in the presence of hole scavengers.[47] Figure 5-7b displays the yield of surface and bulk charge transfer, calculated from photocurrent density in Figure 5-7a, revealing that charge transfer in bulk is much poorer than that at surface. In the case of 350 nm GFO films, the $\eta_{surface}$ value is 55% at +1.23 V vs RHE, which is significantly larger than other ferrites photoanodes such as $CaFe_2O_4$ (5%) and $ZnFe_2O_4$ (10%-40%).[11] With regards to η_{bulk}, it highly depends on the illumination energy. As shown in Figure 5-7c, it can be dramatically enhanced at shorter wavelength, though less efficient bulk charge separation and transfer is a common phenomenon in metal oxides. The internal quantum efficiency spectra recorded at +1.4 V vs. RHE in Figure 5-7c, as well as the corresponding Tauc representation (Figure 5-7d), are strongly consistent with the estimation of the optical band gap (2.7 eV), further confirming that sub-bandgap transitions do not generate free charge carriers. In addition, the photocurrent density of a 350 nm thick GFO photoanode calculated from the external quantum efficiency spectrum is 0.035 mA cm^{-2} under AM 1.5 illumination at +1.4 V vs RHE for the water oxidation reaction.

The absence of surface recombination in the presence of SO_3^{2-} allows rationalizing the photocurrent-voltage characteristics in terms of the Gaertner expression:[46,48,49]

$$IQE = 1 - \frac{e^{(-\alpha W)}}{1+\alpha L_n} \qquad \text{Eqn. (5-1)}$$

where W is the width of the space charge region, and L_n is the holes diffusion length. The fit to the IQE-voltage curves at different wavelengths in Figure 5-7e was obtained using Eqn. (5-1), the α values displayed in Figure 5-3b, while W is calculated from the Schottky equation,[48,49]

$$W = \sqrt{\left[\frac{2\varepsilon\varepsilon_0}{qN_D}\left(U_{fb} - E\right)\right]} \qquad \text{Eqn. (5-2)}$$

employing the experimental values of U_{fb} and N_D. From this analysis, a L_n = 12.5 ± 0.3 nm can be estimated across the range of wavelengths. It is well-known that the mobility of holes is much lower than electrons, so that the minority carrier diffusion length is relatively short in photoanodes. Although the hole diffusion length of GFO is longer than that of some ferrite-based photoanodes, such as Fe_2O_3 (L_n = 2-4 nm) and Fe_2WO_6 (L_n = 10 nm),[50,51] it is not comparable to $BiVO_4$ photoanode that exhibits the diffusion length of up to 57 nm.[52] The fact that Eqn. (5-1) reproduces the experimental curves down to the U_{fb} confirms that surface recombination is negligible in the presence of SO_3^{2-}. On the other hand, the relatively short L_n further indicates that photoelectrode efficiency is primarily limited by bulk recombination, leading to low η_{bulk}. This conclusion is consistent with the very low band dispersion (Figure 5-4c), which induce heavy effective masses of electrons and holes.

Further evidence of the role of carrier transport in the photocurrent responses can be elucidated from the thickness dependence and illumination direction shown in Figure 5-8a to d. These LSV plots were conducted in Ar-saturated 0.1M Na_2SO_3 aqueous solutions at pH 12 and illuminated by a LED with a narrow emission centered at 405 nm and photon flux of 4.25 × 10^{15} cm^{-2} s^{-1}. The photocurrent magnitude increases with an increasing thickness (Figure 5-8a), which is determined by the number of coating steps. The photocurrent magnitude increases by a factor of three upon increasing the film thickness from 110 to 350 nm. Based on the optical

constant (Figure 5-3b), the penetration depth of light at a wavelength of 405 nm ($1/\alpha$) is approximately 500 nm. Thus, increasing film thickness in this range effectively increases the flux of carrier generation. Figure 5-8b shows that 350 nm

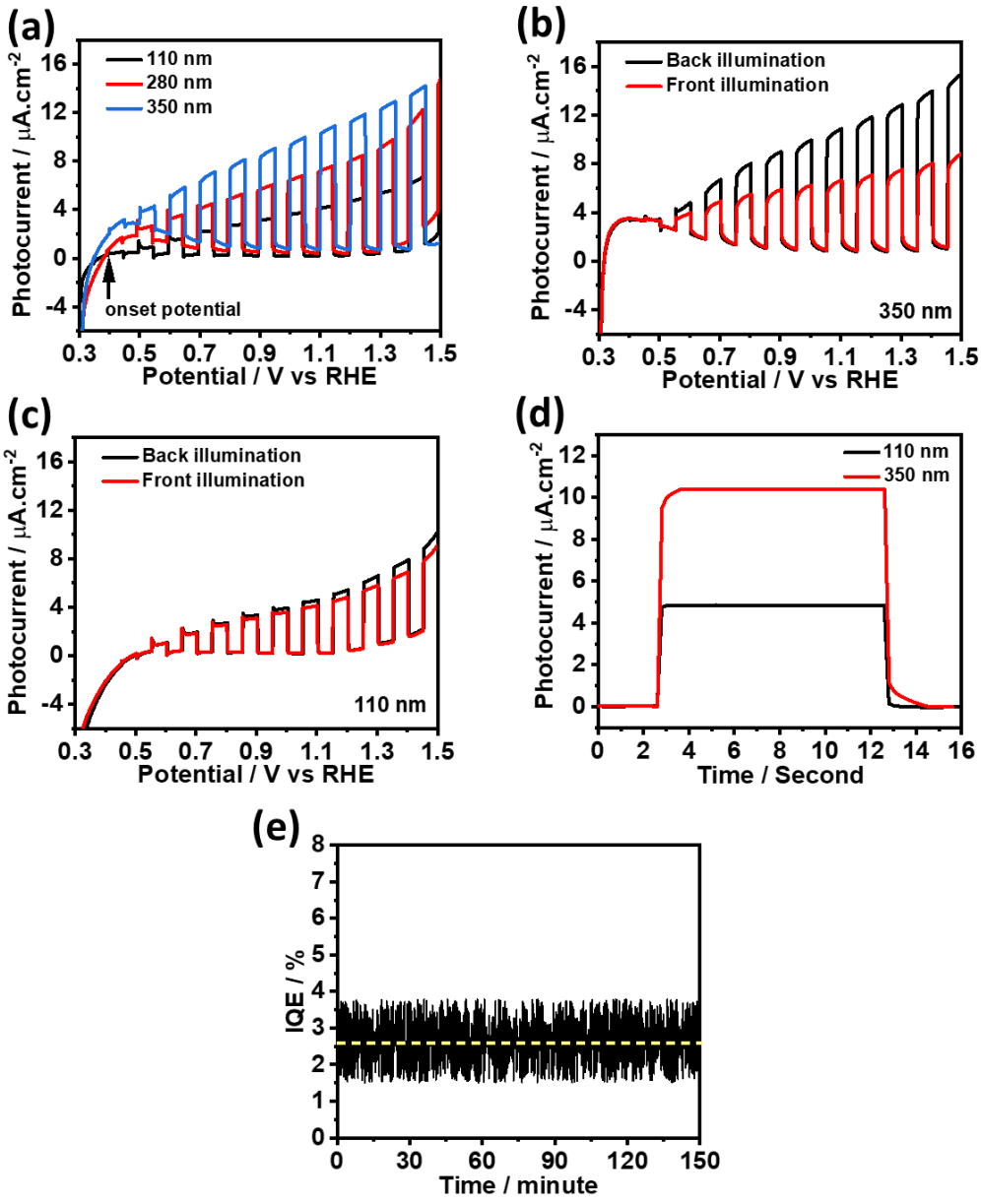

Figure 5-8 Thickness dependence of photocurrent responses and PEC stability test: (a) LSV responses of films with a thickness between 110 and 350 nm in Ar-saturated 0.1M Na_2SO_3 aqueous solutions at pH 12; photocurrent responses under the back and front illumination at 350 nm (b) and 110 nm (c) films; (d) photocurrent transient responses at 350 and 110 nm GFO films at +1.2 V vs. RHE; and (e) stability test of 350 nm film under a 405 nm continuous irradiation.

films exhibit twice larger photocurrents under *back illumination* (through the FTO-coated glass) than under *front illumination* (through GFO/electrolyte junction). On the other hand, the difference between front and back illumination is very small in 110 nm films (Figure 5-8c). Photocurrent transients in Figure 5-8d also show a slower rise time and decay in the 350 nm films, while the 110 nm film displays a sharper response. These results clearly indicate that electron transport in these films is also a key limiting factor in the performance of these materials, which may arise not only from intrinsically low mobility but also the presence of deep trap states.[53] In addition, Figure 5-8e shows the PEC stability of 350 nm GFO film in Ar-saturated Na_2SO_3 aqueous solutions (pH 12) under a 405 nm continuous irradiation for 150 minutes, indicating that GFO photoanode can remain active for long-term applications.

As mentioned above, the similar ionic radius between Ga^{3+} and Fe^{3+} leads to unique composition, structure, and photoelectrochemical properties in GFO thin films. Figure 5-9a illustrates the strong effect of the Ga:Fe ratio on the photoelectrochemical responses under the identical experimental conditions as Figure 5-8a. Decreasing the Ga:Fe ratio from x=1.2 to x=0.7 leads to a 10-fold increase in photocurrent, which may be attributed to the increase of trap states connected to Ga sites. The Ga:Fe ratios (x values) reported in Figure 5-9 correspond to the composition of the sol-gel precursor. Analysis of the film composition reveals small variations of approximately 10% with respect to the Ga:Fe ratio in the sol-gel precursor. The XRD patterns of various $Ga_xFe_{2-x}O_3$ compositions investigated in (photo)electrochemical characterization (Figure 5-9a and c) illustrate almost identical results. Representative XRD patterns (Figure 5-9b) show no clear evidence of the binary oxide phase in this range of composition, although the Ga-Fe-O phase diagram is very rich as a result of the similar ionic radii of both cations.[54,55] However,

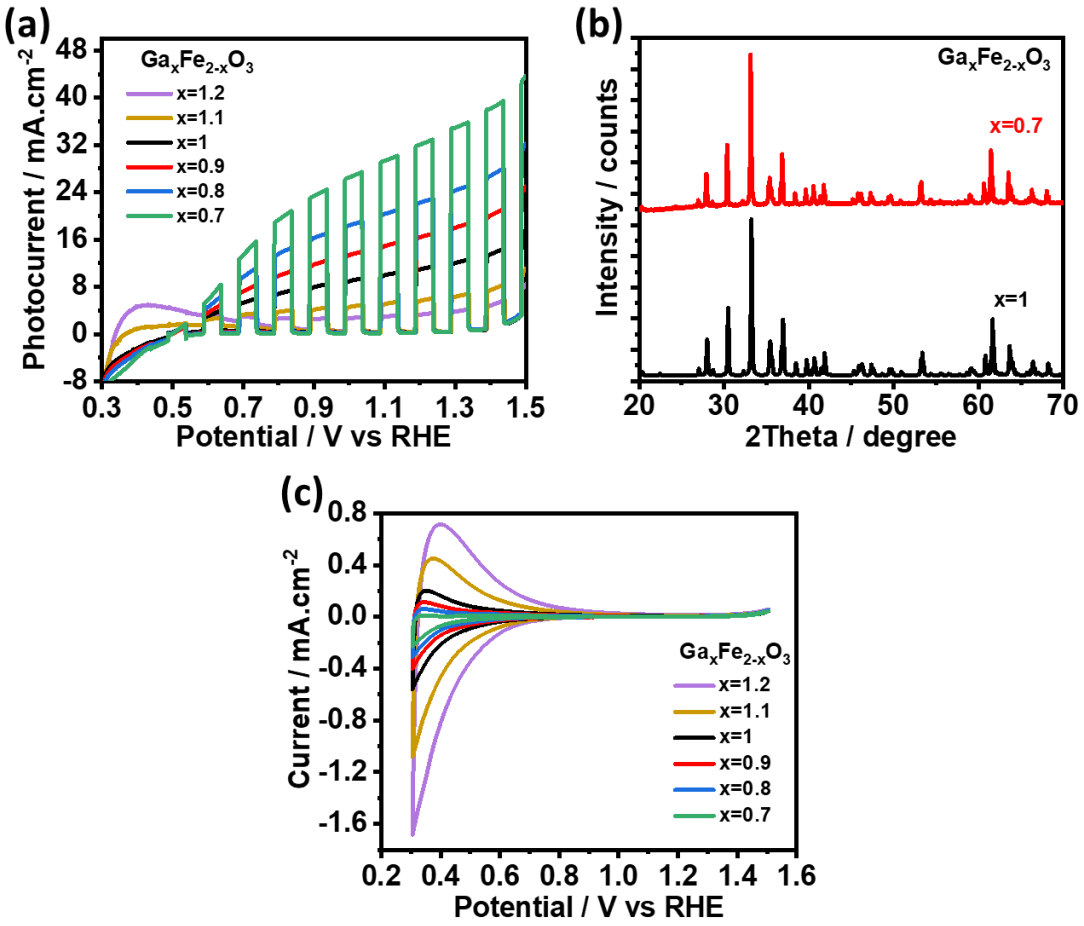

Figure 5-9 The effect of Ga:Fe ratio: (a) $Ga_xFe_{2-x}O_3$ photocurrent responses as a function of Ga:Fe ratio (x values) in the sol-gel precursor; Scan rate, wavelength, and photon flux values are as indicated in Figure 5-8a; (b) representative XRD patterns of $Ga_xFe_{2-x}O_3$ (x=1 and 0.7); and (c) cyclic voltammograms of $Ga_xFe_{2-x}O_3$ thin films, recorded at 100 mV s^{-1} in the dark in Ar-saturated 0.1M Na_2SO_3 aqueous solutions (pH 12).

the hematite phase can be clearly seen in XRD patterns when x decreases below 0.7 (such as 0.6, data is not shown). Cyclic voltammograms recorded as a function of the $Ga_xFe_{2-x}O_3$ compositions (Figure 5-9c) show that the onset potential of electron accumulation systematically shifts towards more negative potentials as the Ga content decreases in the film. This is a clear indication of a shift in the flat-band potential towards more negative potentials, i.e., upward energy shift of the band edges, which is also consistent with the model proposed by Meng et al.[45] These unique properties of GFO have important implications towards designing highly

active photoanodes, including: (1) carrier collection and light capture cross-section can be improved by depositing ultra-thin GFO layers onto highly textured electron transporting layers, and (2) band alignment and carrier transport can be finely tuned by adjusting Ga:Fe ratio.

5.6 Summary

Solution-processed GFO thin films exhibit remarkable photoelectrochemical properties, including high surface charge transfer ratio towards the OER, which manifests itself by a photocurrent onset potential close to the flat band potential (between +0.4 and +0.5 V vs. RHE). We are not aware of any other semiconductor material capable of evolving oxygen at the flat-band potential in the absence of protecting layers and co-catalysts. In the presence of SO_3^{2-} ions acting as hole scavengers, no evidence of surface recombination is observed. In addition, the high PEC stability of GFO photoanode is another significant property for viable and scalable PEC water splitting. Based on the Gaertner model, a hole diffusion length of 12.5 ± 0.3 nm can be estimated under a range of wavelengths close to the bandgap. The ideal behavior of the GFO/electrolyte junction is also observed in capacitance-potential curves, which follows the Mott-Schottky equation for more than 1 V down to the flat-band potential. The CBM is located +0.52 V vs. RHE, which is the deepest CBM reported for any ferrite. DFT-HSE06 calculations show that this material is highly ionic, and the relatively deep CBM can be rationalized in terms of Coulombic potential generated by the Ga^{3+} cation. Our study also shows that the similar ionic radii of Ga^{3+} and Fe^{3+} ion introduces significant complexity in the material structure, featuring tetrahedral and octahedral coordinations of the cations, which manifest themselves in multiple Raman modes and optical transitions. The GFO photoresponses are dominated by bulk recombination losses, linked to low

carrier mobility resulting from low band dispersion and deep trap states. Our results also show that bulk recombination is significantly decreased in Ga-poor films. These experimental and computational results demonstrate not only the potential of this material as photoanodes, but also the tunability of its electronic properties and the potential for integration into highly efficient photoelectrochemical devices.

5.7 References

(1) Walter, M. G.; Warren, E. L.; McKone, J. R.; Boettcher, S. W.; Mi, Q.; Santori, E. A.; Lewis, N. S. Solar Water Splitting Cells. *Chem. Rev.* **2010**, *110*, 6446–6473.

(2) Ochiai, T.; Fujishima, A. Photoelectrochemical Properties of TiO_2 Photocatalyst and Its Applications for Environmental Purification. *J. Photochem. Photobiol. C Photochem. Rev.* **2012**, *13*, 247–262.

(3) Sivula, K.; Le Formal, F.; Grätzel, M. Solar Water Splitting: Progress Using Hematite (α-Fe_2O_3) Photoelectrodes. *ChemSusChem* **2011**, *4*, 432–449.

(4) Liu, M.; Nam, C. Y.; Black, C. T.; Kamcev, J.; Zhang, L. Enhancing Water Splitting Activity and Chemical Stability of Zinc Oxide Nanowire Photoanodes with Ultrathin Titania Shells. *J. Phys. Chem. C* **2013**, *117*, 13396–13402.

(5) Knöppel, J.; Zhang, S.; Speck, F. D.; Mayrhofer, K. J. J.; Scheu, C.; Cherevko, S. Time-Resolved Analysis of Dissolution Phenomena in Photoelectrochemistry – A Case Study of WO_3 Photocorrosion. *Electrochem. commun.* **2018**, *96*, 53–56.

(6) Tae Woo Kim and Kyoung-Shin Choi. Nanoporous $BiVO_4$ Photoanodes with Dual-Layer Oxygen Evolution Catalysts for Solar Water Splitting. **2014**, *343*, 990–995.

(7) Zachäus, C.; Abdi, F. F.; Peter, L. M.; Van De Krol, R. Photocurrent of $BiVO_4$ Is Limited by Surface Recombination, Not Surface Catalysis. *Chem. Sci.* **2017**, *8*, 3712–3719.

(8) Kim, J. H.; Jang, Y. J.; Choi, S. H.; Lee, B. J.; Kim, J. H.; Park, Y. Bin; Nam, C. M.; Kim, H. G.; Lee, J. S. A Multitude of Modifications Strategy of $ZnFe_2O_4$ Nanorod Photoanodes for Enhanced Photoelectrochemical Water Splitting Activity. *J. Mater. Chem. A* **2018**, *6*, 12693–12700.

(9) Haart, L. D.; Blasse, G. Photoelectrochemical Properties of Ferrites with The Spinel Structure. *Solid State Ionics* **1985**, *16*, 137–140.

(10) Zhang, B.; Seki, M.; Zhou, H.; Chen, J.; Tabata, H. $InFeO_3$ Photoelectrode with Two-dimensional Superlattice for Visible- and Ultraviolet-light-driven Water Splitting.

APL Mater. **2020**, *8*, 051107.

(11) Guijarro, N.; Bornoz, P.; Prévot, M.; Yu, X.; Zhu, X.; Johnson, M.; Jeanbourquin, X.; Le Formal, F.; Sivula, K. Evaluating Spinel Ferrites MFe_2O_4 (M = Cu, Mg, Zn) as Photoanodes for Solar Water Oxidation: Prospects and Limitations. *Sustain. Energy Fuels* **2018**, *2*, 103–117.

(12) Shah, J. H.; Ye, H.; Liu, Y.; Idris, A. M.; Malik, A. S.; Zhang, Y.; Han, H.; Li, C. Exploration of the Intrinsic Factors Limiting the Photocurrent Density in Ferroelectric $BiFeO_3$ Thin Film. *J. Mater. Chem. A* **2020**, *8*, 6863–6873.

(13) Huang, W.; Harnagea, C.; Tong, X.; Benetti, D.; Sun, S.; Chaker, M.; Rosei, F.; Nechache, R. Epitaxial Bi_2FeCrO_6 Multiferroic Thin-Film Photoanodes with Ultrathin p-Type NiO Layers for Improved Solar Water Oxidation. *ACS Appl. Mater. Interfaces* **2019**, *11*, 13185–13193.

(14) Ogawa, Y.; Kaneko, Y.; He, J. P.; Yu, X. Z.; Arima, T.; Tokura, Y. Magnetization-Induced Second Harmonic Generation in a Polar Ferromagnet. *Phys. Rev. Lett.* **2004**, *92*, 047401.

(15) Katayama, T.; Yasui, S.; Osakabe, T.; Hamasaki, Y.; Itoh, M. Ferrimagnetism and Ferroelectricity in Cr-Substituted $GaFeO_3$ Epitaxial Films. *Chem. Mater.* **2018**, *30*, 1436–1441.

(16) Kim, J. Y.; Koo, T. Y.; Park, J. H. Orbital and Bonding Anisotropy in a Half-Filled $GaFeO_3$ Magnetoelectric Ferrimagnet. *Phys. Rev. Lett.* **2006**, *96*, 047205.

(17) Dhanasekaran, P.; Gupta, N. M. Factors Affecting the Production of H_2 by Water Splitting over a Novel Visible-Light-Driven Photocatalyst $GaFeO_3$. *Int. J. Hydrogen Energy* **2012**, *37*, 4897–4907.

(18) Mishra, S. K.; Mittal, R.; Singh, R.; Zbiri, M.; Hansen, T.; Schober, H. Phase Stability of Multiferroic $GaFeO_3$ up to 1368 K from in Situ Neutron Diffraction. *J. Appl. Phys.* **2013**, *113*, 174102.

(19) Mukherjee, S.; Garg, A.; Gupta, R. Probing Magnetoelastic Coupling and Structural Changes in Magnetoelectric Gallium Ferrite. *J. Phys. Condens. Matter* **2011**, *23*, 445403.

(20) Gupta, H. C.; Singh, M. K.; Tiwari, L. M. Lattice Dynamic Investigation of Raman and Infrared Wavenumbers at the Zone Center of Orthorhombic $RFeO_3$ (R = Tb, Dy, Ho, Er, Tm) Perovskites. *J. Raman Spectrosc.* **2002**, *33*, 67–70.

(21) Shim, S. H.; Duffy, T. S. Raman Spectroscopy of Fe_2O_3 to 62 GPa. *Am. Mineral.* **2002**, *87*, 318–326.

(22) Shebanova, O. N.; Lazor, P. Raman Spectroscopic Study of Magnetite ($FeFe_2O_4$): A New Assignment for the Vibrational Spectrum. *J. Solid State Chem.* **2003**, *174*,

424–430.

(23) Ghosh, S.; Kamaraju, N.; Seto, M.; Fujimori, A.; Takeda, Y.; Ishiwata, S.; Kawasaki, S.; Azuma, M.; Takano, M.; Sood, A. K. Raman Scattering in $CaFeO_3$ and $La_{0.33}Sr_{0.67}FeO_3$ across the Charge-Disproportionation Phase Transition. *Phys. Rev. B - Condens. Matter Mater. Phys.* **2005**, *71*, 245110.

(24) Onuma, T.; Fujioka, S.; Yamaguchi, T.; Itoh, Y.; Higashiwaki, M.; Sasaki, K.; Masui, T.; Honda, T. Polarized Raman Spectra in β-Ga_2O_3 Single Crystals. *J. Cryst. Growth* **2014**, *401*, 330–333.

(25) Thomasson, A.; Kreisel, J.; Lefèvre, C.; Roulland, F.; Versini, G.; Barre, S.; Viart, N. Raman Scattering of Magnetoelectric Gallium Ferrite Thin Films. *J. Phys. Condens. Matter* **2013**, *25*, 045401.

(26) Golosova, N. O.; Kozlenko, D. P.; Kichanov, S. E.; Lukin, E. V.; Dubrovinsky, L. S.; Mammadov, A. I.; Mehdiyeva, R. Z.; Jabarov, S. H.; Liermann, H. P.; Glazyrin, K. V.; Dang, T. N.; Smotrakov, V. G.; Eremkin, V. V.; Savenko, B. N. Structural, Magnetic and Vibrational Properties of Multiferroic $GaFeO_3$ at High Pressure. *J. Alloys Compd.* **2016**, *684*, 352–358.

(27) Yan, H.; Huang, Y.; Cui, W.; Zhi, Y.; Guo, D.; Wu, Z.; Chen, Z.; Tang, W. Magnetic Properties and Crystal Structure of $Ga_{2-x}Fe_xO_3$. *Powder Diffr.* **2018**, *33*, 195–201.

(28) Ramachandran, R. K.; Dendooven, J.; Botterman, J.; Pulinthanathu Sree, S.; Poelman, D.; Martens, J. A.; Poelman, H.; Detavernier, C. Plasma Enhanced Atomic Layer Deposition of Ga_2O_3 Thin Films. *J. Mater. Chem. A* **2014**, *2*, 19232–19238.

(29) Sun, X.; Tiwari, D.; Fermin, D. J. Promoting Active Electronic States in $LaFeO_3$ Thin-Films Photocathodes via Alkaline-Earth Metal Substitution. *ACS Appl. Mater. Interfaces* **2020**, *12*, 31486–31495.

(30) Celorrio, V.; Calvillo, L.; van den Bosch, C. A. M.; Granozzi, G.; Aguadero, A.; Russell, A. E.; Fermín, D. J. Mean Intrinsic Activity of Single Mn Sites at $LaMnO_3$ Nanoparticles Towards the Oxygen Reduction Reaction. *ChemElectroChem* **2018**, *5*, 3044–3051.

(31) Díez-García, M. I.; Celorrio, V.; Calvillo, L.; Tiwari, D.; Gómez, R.; Fermín, D. J. $YFeO_3$ Photocathodes for Hydrogen Evolution. *Electrochim. Acta* **2017**, *246*, 365.

(32) Stoerzinger, K. A.; Wang, L.; Ye, Y.; Bowden, M.; Crumlin, E. J.; Du, Y.; Chambers, S. A. Linking Surface Chemistry to Photovoltage in Sr-Substituted $LaFeO_3$ for Water Oxidation. *J. Mater. Chem. A* **2018**, *6*, 22170–22178.

(33) Celorrio, V.; Calvillo, L.; Dann, E.; Granozzi, G.; Aguadero, A.; Kramer, D.; Russell, A. E.; Fermín, D. J. Oxygen Reduction Reaction at $La_xCa_{1-x}MnO_3$ Nanostructures: Interplay between A-Site Segregation and B-Site Valency. *Catal. Sci. Technol.* **2016**, *6*, 7231–7238.

(34) Sherman, D. M. The Electronic Structures of Fe^{3+} Coordination Sites in Iron Oxides: Applications to Spectra, Bonding, and Magnetism. *Phys. Chem. Miner.* **1985**, *12*, 161–175.

(35) Hankin, A.; Bedoya-Lora, F. E.; Alexander, J. C.; Regoutz, A.; Kelsall, G. H. Flat Band Potential Determination: Avoiding the Pitfalls. *J. Mater. Chem. A* **2019**, *7*, 26162–26176.

(36) Taylor, F. H.; Buckeridge, J.; Catlow, C. R. A. Defects and Oxide Ion Migration in the Solid Oxide Fuel Cell Cathode Material $LaFeO_3$. *Chem. Mater.* **2016**, *28*, 8210–8220.

(37) Chueh, C. C.; Li, C. Z.; Jen, A. K. Y. Recent Progress and Perspective in Solution-Processed Interfacial Materials for Efficient and Stable Polymer and Organometal Perovskite Solar Cells. *Energy Environ. Sci.* **2015**, *8*, 1160–1189.

(38) Sun, X.; Tiwari, D.; Fermin, D. J. Nanostructured $LaFeO_3$ Photocathodes with Onset Potentials for the Hydrogen Evolution Reaction Over 1.4 V vs. RHE. *J. Electrochem. Soc.* **2019**, *166*, H764–H768.

(39) Chakrabartty, J.; Nechache, R.; Harnagea, C.; Li, S.; Rosei, F. Enhanced Photovoltaic Properties in Bilayer $BiFeO_3$/Bi-Mn-O Thin Films. *Nanotechnology* **2016**, *27*, 215402.

(40) Díez-García, M. I.; Gómez, R. Investigating Water Splitting with $CaFe_2O_4$ Photocathodes by Electrochemical Impedance Spectroscopy. *ACS Appl. Mater. Interfaces* **2016**, *8*, 21387–21397.

(41) Read, C. G.; Park, Y.; Choi, K. S. Electrochemical Synthesis of P-Type $CuFeO_2$ Electrodes for Use in a Photoelectrochemical Cell. *J. Phys. Chem. Lett.* **2012**, *3*, 1872–1876.

(42) Kim, J. H.; Kim, J. H.; Jang, J. W.; Kim, J. Y.; Choi, S. H.; Magesh, G.; Lee, J.; Lee, J. S. Awakening Solar Water-Splitting Activity of $ZnFe_2O_4$ Nanorods by Hybrid Microwave Annealing. *Adv. Energy Mater.* **2015**, *5*, 1401933.

(43) Li, J.; Wu, N. Semiconductor-Based Photocatalysts and Photoelectrochemical Cells for Solar Fuel Generation: A Review. *Catal. Sci. Technol.* **2015**, *5*, 1360–1384.

(44) Li, H.; Chen, Y.; Xi, S.; Wang, J.; Sun, S.; Sun, Y.; Du, Y.; Xu, Z. J. Degree of Geometric Tilting Determines the Activity of FeO_6 Octahedra for Water Oxidation. *Chem. Mater.* **2018**, *30*, 4313–4320.

(45) Meng, X. Y.; Liu, D. Y.; Qin, G. W. Band Engineering of Multicomponent Semiconductors: A General Theoretical Model on the Anion Group. *Energy Environ. Sci.* **2018**, *11*, 692–701.

(46) Fermín, D. J.; Ponomarev, E. A.; Peter, L. M. Kinetic Study of CdS Photocorrosion by Intensity Modulated Photocurrent and Photoelectrochemical Impedance Spectroscopy. *J. Electroanal. Chem.* **1999**, *473*, 192–203.

(47) Lee, D. K.; Lee, D.; Lumley, M. A.; Choi, K. S. Progress on Ternary Oxide-Based Photoanodes for Use in Photoelectrochemical Cells for Solar Water Splitting. *Chem. Soc. Rev.* **2019**, *48*, 2126–2157.

(48) Gärtner, W. W. Depletion-Layer Photoeffects in Semiconductors. *Phys. Rev.* **1959**, *116*, 84–87.

(49) Li, J.; Peter, L. M. Surface Recombination at Semiconductor Electrodes. Part III. Steady-State and Intensity Modulated Photocurrent Response. *J. Electroanal. Chem.* **1985**, *193*, 27–47.

(50) Kennedy, J. H.; Frese, K. W. J. Photooxidation of Water at α-Fe_2O_3 Electrodes. *J. Electrochem. Soc.* **1978**, *125*, 709-714.

(51) Abdi, F. F.; Chemseddine, A.; Berglund, S. P.; Van De Krol, R. Assessing the Suitability of Iron Tungstate (Fe_2WO_6) as a Photoelectrode Material for Water Oxidation. *J. Phys. Chem. C*, **2017**, *121*, 153–160.

(52) Jang, J.-W.; Friedrich, D.; Muller, S.; Lamers, M.; Hempel, H.; Lardhi, S.; Cao, Z.; Harb, M.; Cavallo, L.; Heller, R.; Eichberger, R.; van de Krol, R.; Abdi, F. F. Enhancing Charge Carrier Lifetime in Metal Oxide Photoelectrodes Through Mild Hydrogen Treatment. *Adv. Energy Mater.* **2017**, *7*, 1701536.

(53) Zhang, Q.; Celorrio, V.; Bradley, K.; Eisner, F.; Cherns, D.; Yan, W.; Fermín, D. J. Density of Deep Trap States in Oriented TiO_2 Nanotube Arrays. *J. Phys. Chem. C* **2014**, *118*, 18207.

(54) Trassin, M.; Viart, N.; Versini, G.; Barre, S.; Pourroy, G.; Lee, J.; Jo, W.; Dumesnil, K.; Dufour, C.; Robert, S. Room Temperature Ferrimagnetic Thin Films of the Magnetoelectric $Ga_{2-x}Fe_xO_3$. *J. Mater. Chem.* **2009**, *19*, 8876–8880.

(55) Mukherjee, S.; Ranjan, V.; Gupta, R.; Garg, A. Compositional Dependence of Structural Parameters, Polyhedral Distortion and Magnetic Properties of Gallium Ferrite. *Solid State Commun.* **2012**, *152*, 1181–1185.

CHAPTER 6.

Conclusion and future outlook

6.1 Conclusion

The initial research aim of this work was to investigate ferrite-based metal oxides to achieve viable and scalable PEC water splitting technology. Lanthanum iron oxide ($LaFeO_3$) shows attractive PEC properties, such as positive onset potential, long-term durability, and favorable band alignment, for HER in the vast family of ferrite-based metal oxides; however, the low EQE of LFO photocathode hinders its practical applications. In this thesis, LFO photocathode was innovated from surface modification (Chapter 3) and bulk structure tuning (Chapter 4). As introduced in Chapter 1, heterostructure and cocatalyst loading are two promising surface modification strategies for improving the performance of photoelectrodes in the process of water splitting, whereas atom doping (substitution) can effectively tune electronic structure in bulk.

TiO_2 thin films and Pt nanoparticles were sequentially deposited onto the surface of nanostructured LFO photocathodes in Chapter 3, leading to a 10-fold increase in the photocurrent responses in the absence of oxygen. The Mott-Schottky plots reveals the flat band potential of LFO thin film is around +1.44 V vs RHE. The most striking observation is the onset potential of LFO (+1.47 V vs RHE) for HER can shift to flat band potential upon the deposition of TiO_2 layer, which is the most positive value reported for a single absorber photoelectrode to the best of my knowledge. These enhancements in PEC behaviour are attributed to the TiO_2 layer not only forms a heterostructure with LFO, but also acts as a surface blocking layer for hole transfer to the electrolyte, and Pt nanoparticles increase the surface charge-transfer kinetics at LFO photocathode.

With regards to lattice substitution, Chapter 4 demonstrates that the substitution of divalent alkaline-earth metal cations Mg^{2+}, Ca^{2+}, Sr^{2+}, and Ba^{2+} into LFO thin films synthesized by sol–gel method enables its EQE to change from below 10% to

15%~20% at a wavelength close to 360 nm and potential bias of +0.45 V vs RHE in the presence of oxygen. More importantly, this work reveals the relationship between PEC performances and structural and electronic properties in LFO-based thin films. The structural variation of various thin films was elucidated by XRD and XPS analysis, for instance, AMC substitution leads to the increase of relatively high iron oxidation states (e.g., Fe^{4+}), which promotes the contraction of the lattice constant at low substitution levels in LFO thin films. In addition, the correlation between Fe oxidation state and Fe−O covalency is the increase of Fe^{4+} species makes Fe-O covalency strong. EIS characterisations probe the change of electronic properties linked to structural variations. There are hole-trap states (intrinsic defects) located around 100 to 200 meV above the valence band edge in pristine LFO, while those intrinsic defects can be weakened upon the substitution of AMC, enhancing majority carrier mobility. At the same time, AMC substituted thin films show fresh states centered at 600 meV above the valence band edge, which promotes the PEC oxygen reduction due to the increase of electron transfer kinetics, based on dynamic PEC analysis.

It is obvious to see that both surface and bulk modification enable LFO thin films to achieve the improvement of PEC performance. Apart from the different innovation sites, the method for LFO thin film preparations is another difference between Chapter 3 and 4. Briefly, the LFO nanoparticles prepared by thermolysis of an ionic-liquid precursor at 900 ^{o}C were sonicated in ethanol and terpineol mixed with ethyl cellulose, followed by spin-coating onto FTO substrate to acquire LFO photocathodes in Chapter 3. The LFO thin films employed in Chapter 4 were synthesized by directly spin-coating precursor solutions onto FTO substrates, subsequently, those thin films were calcined at 600 ^{o}C. The process of photoelectrode synthesis plays a significant role in PEC behaviours, which can be seen in Chapter 1. On the one hand, the powder based LFO photoelectrode

preparation (Chapter 3) can generate a highly crystalline thin film, avoiding the formation of surface states, such as hole-trap states, and increasing surface charge carrier transfer efficiency. To be specific, the presence of surface states in pristine LFO photocathode prepared by direct thin film synthesis in Chapter 4 enables the flat band potential to be 0.12 V more negative than that of nanostructured LFO thin film, which limits the possibility of achieving high photovoltage. Furthermore, the surface recombination that can be clearly seen in directly synthesized LFO thin films is restrained in nanostructured LFO thin films for HER. On the other hand, based on morphological characterisations, direct LFO photoelectrode preparation displays a highly compact, uniform, and reproducible thin film in comparison with powder based LFO photoelectrode synthesis. The high quality photoelectrode can promote bulk charge carrier transfer efficiency, leading to the EQE as high as 20% for PEC oxygen reduction in Chapter 4. In contrast, the dynamic photocurrent studies indicate there exist a number of majority carrier trap states in the powder based LFO photoelectrodes, increasing bulk charge carrier recombination. Grain boundaries in the nanostructured films may become a strong barrier to majority carrier transport, so that electron-hole recombination also tends to occur at the interface of grain boundaries. Moreover, LFO nanoparticles with relatively large crystallite domains in the range of 60 nm fails to close contact with FTO substrate, further blocking the transfer of photogenerated holes at film/substrate interface. It should be noted that although the crystallization and quality of thin films play grand influences on the different PEC behaviours, the effects of different solvents employed in such two type LFO thin film preparation methods are also worth considering.

In addition to innovating existing attractive materials, this thesis also focuses on the discovery of novel metal oxides can be employed in PEC water splitting technology. A new photoanode, gallium iron oxide ($GaFeO_3$), was presented in Chapter 5. The structural, optical and PEC properties of GFO are systematically

reported under the combination of theoretical and experimental investigations for the first time. GFO thin film shows high interfacial hole-transfer efficiency due to slow surface recombination rates, which also enables the onset potential of GFO for OER to coincides with its flat-band potential. The material is highly ionic with the deepest band edge energies reported for any ferrite, providing sufficient driving force for OER. In addition, the results demonstrate GFO photoanode is limited by bulk recombination owing to the short-diffusion length of minority carriers and low mobility of majority carriers. The relatively low bulk charge transfer efficiency can be enhanced by increasing iron ration in GFO thin films. The feasibility of Ga:Fe ratio variation in a large range (from 1.5 to 0.5) is attributed to the similar ironic radii between Ga^{3+} and Fe^{3+}, which cannot be seen in other ternary metal oxides. It should be noted that although GFO has the same general formula of LFO (ABO_3), this is a different class of materials as both metal cations exhibit octahedral and tetrahedral coordination.

6.2 Future outlook

Currently, metal oxides sustain poor charge carrier separation and transfer in PEC water splitting process, leading to relatively low solar energy conversion efficiency, which is one of the grandest reasons impeding the viable application of metal oxides in the field of PEC water splitting. Although numbers of strategies have focused on the enhancement of charge carrier density and mobility in metal oxides, the results remain significantly below the target required for commercial PEC water splitting devices. In the future, there is a vast research space for those who are committed to the investigation of oxide-based photoelectrodes since our existing knowledge related to PEC properties of metal oxides is very limited.

As discussed in Chapter 1, the tandem PEC water splitting devices can show higher STH conversion efficiency than single absorber PEC water splitting cells; more

importantly, tandem cells make it easy to achieve unassisted solar water splitting. Both ferrite photoelectrodes ($LaFeO_3$ and $GaFeO_3$) studied in this thesis are promising materials for the design of PEC water splitting configurations, especially for tandem devices. Currently, boosting photovoltage is one of the most formidable challenges in tandem cell design. The onset potential of LFO and GFO for water reduction and oxidation reaction, respectively, is outstanding in oxide-based PEC water splitting, which enables them to be attractive candidates in the design of tandem configurations. However, the low quantum efficiency of both materials significantly hinders their development. Effective innovation strategies on the improvement of energy conversion efficiency should be found in the future.

Based on the discussion above, it is clear to see that the performances of LFO photocathodes employing two different synthesis methods respectively show unique advantages in the process of PEC water splitting for hydrogen generation in Chapter 3 and 4. Integrating their merits on the same LFO thin film is one of the feasible strategies to enhance its PEC behaviours, though it can be foreseen that there is a trade-off between them. In addition, the EQE of LFO thin film is still extremely low for HER, according to all published studies so far. The current explanations for this challenge are surrounded by the poor water reduction kinetics at LFO surface and the competition of photogenerated holes at film/water interface. In this thesis, we originally elaborated the intrinsic defect in LFO thin film also plays an important role in the performance of PEC hydrogen generation; however, our understandings of electronic states associated with intrinsic (extrinsic) defect structures remain rather shallow. Thus, it is critical to further explore the whole picture into those complex factors that impede the energy conversion efficiency at LFO photocathode for HER in the future.

With regards to GFO photoanode, it can be predicted that the research spaces are wide, since it is the first time to be reported for PEC water splitting. The innovation

of GFO thin film can be started with increasing bulk charge carrier transfer. For example, as mentioned in Chapter 5, there are two suggestions: (i) the deposition of ultra-thin GFO layers onto highly textured electron transporting layers can enhance the charge carrier collection and light capture cross-section, and (ii) band alignment and carrier transport can be finely tuned employing the feasible ration variation between Ga^{3+} and Fe^{3+}. Then, it is worth mentioning that GFO is a typical ferroelectric material; therefore, the study of PEC performance assisted by polarization tends to be an interesting project. On the other hand, the ferroelectric properties of GFO is likely to generate widespread attention in other solar energy conversion fields, such as photovoltaics design.

The ultimate aim of investigating PEC water splitting is to produce hydrogen. Those PEC experimental work for hydrogen or oxygen generation in this thesis was carried out in a stable electrolyte (Ar-saturated Na_2SO_4 aqueous solutions), which in principle means that the only solar energy conversion reaction that can occur at photoelectrode surface should be a water reduction or oxidation reaction. However, there are no gas (hydrogen or oxygen) measurements in this thesis. Therefore, employing appropriate gas characterization technologies in the future can not only experimentally validate the occurrence of water reduction and oxidation reactions, but also provide more guidance on the topics such as gas collection methods for the practical application of PEC water splitting devices.